PION ELECTROPRODUCTION FROM HELIUM3, DEUTERIUM, AND HYDROGEN

A Dissertation

By

Stephen Milton Avery

Submitted to the Graduate College of
Hampton University
in partial fulfillment of the requirements
for the degree of

DOCTOR OF PHILOSOPHY

May 2002

This dissertation submitted by Stephen Milton Avery in partial fulfillment of the requirements for the degree of Doctor of Philosophy at Hampton University, Hampton, Virginia, is hereby approved by the committee under whom the work has been completed.

Cynthia Keppel, Ph. D.
Chair

Oliver K. Baker, Ph. D.

Rolf Ent, Ph. D.

Harold E. Jackson, Ph. D.

Khin Maung Maung, Ph. D.

Donald A. Whitney, Ph. D.
Dean of the Graduate College

Date

ABSTRACT

PION ELECTROPRODUCTION FROM HELIUM3, DEUTERIUM, AND HYDROGEN. (May 2002)

Stephen Milton Avery, B.S., Millersville University;
M.S., Hampton University; Ph.D., Hampton University
Chair of Advisory Committee: Dr. Cynthia Keppel

A series of measurements for pion electroproduction from helium-3, deuterium, and hydrogen were completed at the Thomas Jefferson National Accelerator Facility by the NucPi Collaboration. **E91003** began taking data in February 1998 and was completed in April 1998. The longitudinal and transverse parts of the differential cross section were extracted, by means of a Rosenbluth type separation, in the direction parallel to the virtual photon, at $Q^2 = 0.4$ GeV^2, for W = 1.15 and W = 1.6 GeV. The mass dependence of the longitudinal cross section should provide insight into the surprising apparent absence of any significant cross section enhancement due to excess pions in the nuclear medium.

DEDICATION

To my wife and best friend, LaShon.

God has the glory in what he conceals, kings have glory in what they fathom.

Proverbs 25:2

Um Credo Intelligum

ACKNOWLEDGMENTS

All glory and thanks to God and His Son, Jesus Christ. First, I would like to thank my parents, Curtis and Lorraine Avery, for sacrificing much in their lives to give me a quality education and sound religious foundation. I would like to thank my big brother, David, for being an excellent role model. To my Aunt Emma and my cousins Changa Bilaal and Rosetta. To the entire Taylor family for their blessings and encouragement. Thanks to my parents–in–law, Vincent and Pam Coles, the entire Coles clan and my extended family for their love and support. I would like to thank my advisor, Dr. Cynthia Keppel, for supporting me in my career choices and agreeing to accept the duties of being my advisor. To Dr. Harold Jackson for proposing this experiment, and to Dr. Rolf Ent for always finding time to talk and being straight–forward in our discussions. I want to thank Dr. Khin Maung for being an excellent teacher. I've had four great teachers in my lifetime, and you are one of them. To Dr. Keith Baker who has been a mentor since day one. Thanks for always saying the right words to make me believe that I am good enough and encouraging me to continue on. I would like thank Dr. Warren Buck, Carlane Pittman, and Vevelyn Nazario for their commitment. To

Dr. Donald Lyons for “keeping it real”. Also, thanks to Dr. Jose Goity and Dr. Donald Whitney. I want to acknowledge the hard work and dedication of Dr. Paul Gueye. His commitment to the students has contributed tremendously to our success. To Dr. M. Eric Christy for helping me, even though, he was extremely busy with other projects. A special thank you to my fellow graduate students and colleagues: Dr. Mark Harvey, Dr. Wendy Hinton, Alicia Uzzle, Dr. Jinseok Cha, Dr. Peter Agbakpe, Lulin Yuan, Anthony Cochran, Leon Cole, Leon Reynolds, Ceasar Jackson, and all the HU graduate students. In the words of Booker T. Washington, ”The world cares very little about what a man or woman knows; it is what a man or woman is able to do that counts”. Let’s keep this thing going. Thank you Leophus King at MU for believing in me. I wish to thank my Argonne/NucPi team: John Arrington and Dave Gaskell, for there help on the Monte Carlo simulation and for helping me get through the analysis. Thanks to Brian Mueller, Jörg Reinhold, Dipangkar Dutta, Gabriel and Ioana Niculescu. To Hall C staff: Dave Mack, Bill Vulcan, Joe Mitchell, Hamlet Mkrtchyan, Steve Wood, Joe Beaufait, Joe Mitchell, and Jim Dunne. To my wife LaShon and my daughter Taylor, thank you for your patience and understanding during this busy time, and for always letting me know that you support me. Asante.

TABLE OF CONTENTS

Page

LIST OF TABLES

LIST OF FIGURES

Figure Page

Figure Page

CHAPTER 1

Introduction and Motivation

Nuclear physics deals with the study of the components of matter and how they interact with each other. The framework of matter has many distinct levels. The atom was once considered to be the basic building block of matter, but experiment has shown that atoms are composed of nuclei and electrons. The nucleus, which is made of protons and neutrons, has sub-structure made up of quarks and gluons. Trying to understand the structure of matter and how the fundamental constituents interact is not an easy task, primarily because the size of the constituents is so small. The atom is about 10^{-8} cm; the diameter of a nucleus is about 10^{-12} cm; protons and neutrons have a radius of about 10^{-13} cm; and quarks and electrons are smaller than 10^{-16} cm. Today, we believe that quarks and electrons are point particles (structureless).

Although proton and other particle accelerators have been around since the 1930s, one of the most successful tools for studying nuclear structure has been the electron linear accelerator. Experiments at SLAC (*S*tanford *L*inear *A*ccelerator *C*enter), which was constructed in the 1960s, gave the first evidence that protons and neutrons had substructure [1] [2]. This substructure was later called “quarks”. When the electron scatters from a target it transfers momentum to the target by emitting a virtual photon. We use virtual photons as a probe in the nucleus for extracting information. From the de Broglie wavelength relation $\lambda = \mathrm{h/p}$ we see that increasing the momentum (and energy) decreases the wavelength of the photon. If the wavelength is large it will not be able to penetrate the nucleon and scatters from it intact. This is known as elastic scattering. As the wavelength decreases, the photon is able to penetrate the nucleon exciting it or breaking it up to create new particles, this is known as inelastic scattering. The case where the photon wavelength is so small that it probes the quarks directly is known as deep inelastic scattering.

As stated earlier, experimentally it is difficult to study matter in its most fundamental form. It is just as difficult to do it theoretically. The theory that we use to understand the quark building blocks of matter is called $Quantum$ $Chromodynamics(QCD)$. QCD is the theory of the strong interactions that make quarks and gluons come together to form hadrons (3-quark baryons and 2-quark mesons). The quarks are the pieces and the gluons are the "glue" that holds them together. The gluon is the carrier of the strong interaction between the quarks. Basically, QCD is the theory of the fundamental structure of matter. Using experimental data and comparing it with theoretical predictions, we are able to develop a deeper understanding of fundamental building blocks of nature.

1.1 What is a pion?

Quarks have been observed to form particles in groups of 2 (mesons) or 3 (baryons) only. The lightest quarks are the up and down, and the pion is composed of one each. Pions are, then, the lightest known bound quark objects. Therefore, the pion mass is small, $m_\pi \approx 139$ MeV, smaller then the masses of other hadronic particles (particles made of quarks) by a significant amount (see table 1.1). This suggests that the pion may be of a special character as compared to the other hadrons. QCD suggests a low energy scenario which corresponds to a familiar principle of superconductivity [3]. The ground state of a superconductor is a condensate of copper pairs, while the QCD ground state has a quark pair condensate. The two quark pion is the lowest energy excitation of this ground state.

Hadron	Charge State	J^π	Mass (MeV)	Width (MeV)
Nucleon	proton	$\frac{1}{2}^+$	m_p=938.3	stable
	neutron	$\frac{1}{2}^+$	m_n=939.6	stable
Δ-isobar	Δ^{++}	$\frac{3}{2}^+$	m_Δ=1232	115
	Δ^+	$\frac{3}{2}^+$	“	“
	Δ^0	$\frac{3}{2}^+$	“	“
	Δ^-	$\frac{3}{2}^+$	“	“
Pion	π^+	0^-	m_{π^+}=139.6	$2.52x10^{-14}$
	π^-	0^-	m_{π^-}=139.6	“
	π^0	0^-	m_{π^0}=135.0	$8x10^{-6}$
$\rho - meson$	ρ^+	1^-	m_ρ=769	154
	ρ^-	1^-	“	“
	ρ^0	1^-	“	“
ω-meson	ω^0	1^-	m_ω=783	10

Table 1.1: Properties of low mass hadrons

1.1.1 Why is the pion special: The Yukawa Picture

The long range interaction between two or more nucleons is based on the exchange of virtual field quanta between the nucleons. The lightest of these quanta is the pion, and it is the dominant component of the long range nuclear force, the force that bonds the nucleons together to form a nucleus.

Yukawa proposed that nucleons emit particles that stay near the nucleons and then are reabsorbed. These particles are now called *pions*, and they are the facilitators of the nuclear force. It is well known that the outer part of the nucleon cloud is dominated by virtual pions. During the time the pion is being emitted and reabsorbed, the nucleon maintains its rest mass. This is a temporary violation of the mass-energy conservation law because the normal rest mass increases before the pion is emitted and after it is absorbed. The pion cannot escape from the nucleon because that would be a permanent violation of the mass-energy conservation law. Based on the uncertainty principle, temporary violations of the mass-energy conservation law are possible as long as they last for a very short time. These pion are considered to be *virtual* because they are short lived and their existence is dependent on temporarily violating the mass-energy conservation law.

If two nucleons are close together, the pion clouds can overlap and these *virtual pions* can transfer from one cloud to the other. In this process the momentum of the pion is also transfered from one nucleon to the other. When momentum is transferred it has the same effect as applying a force. According to Yukawa, the exchange of *virtual pion* between nucleons leads to the nuclear force acting between them, binding the nucleus together. The more nucleons that are binded together, the stronger the binding energy.

The theory that describes the interactions of electrons and photons is called *Quantum Electrodynamics*(QED). Yukawa adapted the theory of (QED), using two nucleons interacting with a short range strong force instead of two electrons with a long range Coulomb force. He assumed the particle exchanged had a non-zero rest mass instead of a zero rest mass as in QED. He first considered the classical electrostatic potential $\phi(r)$:

$$\phi(r) = \frac{e_1}{4\pi r}. \tag{1.1}$$

The potential energy for two point charges(e_1,e_2) separated by a distance r is:

$$V(r) = \frac{e_1 e_2}{4\pi}\frac{1}{r}. \tag{1.2}$$

If we consider the same case for two nucleons, the field outside one nucleon with a coupling constant g_1 has a potential of:

$$\Phi(r) = -\frac{g_1}{4\pi}\frac{e^{-mr}}{r}. \tag{1.3}$$

The potential energy for two nucleons with coupling constants (g_1,g_2) separated by a distance r is:

$$V(r) = -\frac{g_1 g_2}{4\pi}\frac{e^{-mr}}{r}. \tag{1.4}$$

The only differences between the Coulomb potential and the meson potential are the sign change and the exponential form of the meson potential. When Yukawa made this prediction, the pion wasn't discovered yet. It would take more then ten years before his prediction could be confirmed.

If a nucleon is surrounded by a cloud with N number of pions, you can make a logical assumption that two nucleons could have $2N$ number of pions, and so on. Therefore, it would be fair to say that the more nucleons there are, the more virtual pions you expect. In fig. 1.1, the binding energy per nucleon initially increases rapidly as a function of mass number. From Yukawa's point of view, the pion is the dominant component of the long range nuclear force and the pion exchange currents provide the bulk of the nuclear binding. Where there are more nucleons (higher mass number), there are more pions, and hence a larger binding force. Given this argument, we would expect more (*excess*) pions in lithium than deuterium, for example. In heavier nuclei, the nucleus becomes more dense and the repulsive Coulomb interactions between protons become more dominant. One of the most fundamental challenges in nuclear physics today is to find an unambiguous signature of nuclear pions.

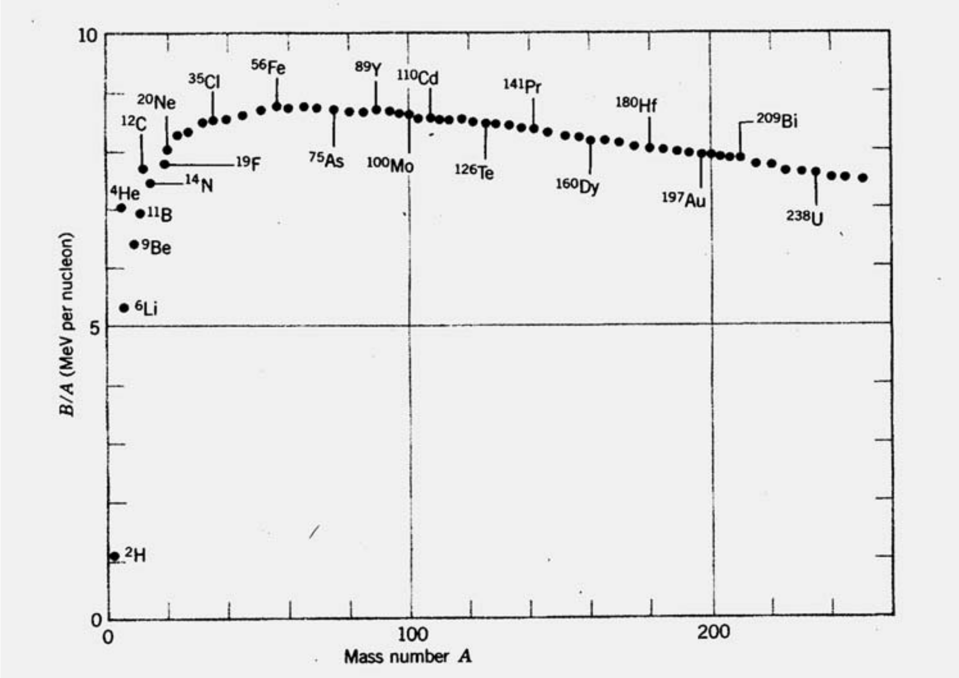

Figure 1.1: Behavior of observed binding energy per nucleon B/A as a function of mass number A.

1.2 Nuclear Pions - Fact or Fiction?

In February of 1983, Bertsch *et al.* [4] wrote an article in *Science* magazine discussing three experiments which looked for pionic effects in nuclei. The first was a deep inelastic muon scattering experiment, the second is a quasi-elastic polarization transfer experiment, and the third a Drell-Yan experiment. All of these experiments will be discussed in detail in the following section. All sought to answer the question “Where are the Nuclear Pions?”

1.2.1 European Muon Collaboration(EMC)

The *European Muon Collaboration* (EMC) were the first to state that the nucleon structure functions describing the nucleon's quark composition are modified inside the nucleus [6]. A simple picture of the nucleus would be a bunch of free, non-interacting nucleons, where the the structure function measured from deep inelastic scattering (scattering from the quarks) would just be the neutron structure function times N plus the proton structure function times Z. That is, the scattering from quarks inside the nucleon would not be changed by that nucleon being in a nuclear environment.

Deep inelastic scattering is the region where the four-momentum transfer Q^2 and the energy transfer ν are both large. Scattering experiments in this region are important because here is where the internal structure of the nucleon is exposed, probing the nucleon's point-like partons. The cross section for inelastic scattering can be written as

$$\frac{d^2\sigma}{d\,\Omega d\,E'} = \frac{4\alpha^2 E^{\prime 2}}{Q^4}\Big[W_2(\nu, Q^2)\cos^2(\frac{\theta}{2}) + 2\,W_1(\nu, Q^2)\sin^2(\frac{\theta}{2})\Big] \quad . \tag{1.5}$$

In inelastic scattering the functions $W_1(\nu, Q^2)$ and $W_2(\nu, Q^2)$ are analogous to the form factors $G_E(q^2)$(electric form factor) and $G_M(q^2)$(magnetic form factor) which yield the nucleon charge and current structure in elastic scattering. $W_1(\nu, Q^2)$ and $W_2(\nu, Q^2)$ are functions of two independent variables Q^2 and ν. As $Q^2 \to \infty$ and

$\nu \to \infty$ the structure functions scale as

$$MW_1(\nu, Q^2) \to F_1(x) \tag{1.6}$$

$$\nu W_2(\nu, Q^2) \to F_2(x) \tag{1.7}$$

In this limit, the electron is seen as scattering from the nucleon's point-like constituents (quarks). The structure functions are no longer functions of Q^2 and ν separately, but are expressed as a dimensionless scaling variable defined by

$$x = \frac{Q^2}{2M\nu} \tag{1.8}$$

x is defined as *Bjorken* x. The structure functions exhibit their point-like substructure through *Bjorken* scaling.

The *European Muon Collaboration* is known for the so-called *EMC* effect [6]. In 1983, they found that the ratio of nuclear structure function W_2 per nucleon in iron differed from that in deuterium. They scattered high energy muons off the quarks in nuclear targets, and found comparably more quarks than in deuterium. The conclusion was that these extra quarks had come from the pion field. A calculation by Ericson and Thomas supported these findings [7], concentrated in an area of $x < 0.3$. Later experiments done at *SLAC* found smaller enhancements in the same x range [8] [9]. A second *EMC* collaboration confirmed these results [10] [11]. Figure 1.2 shows the data from these experiments.

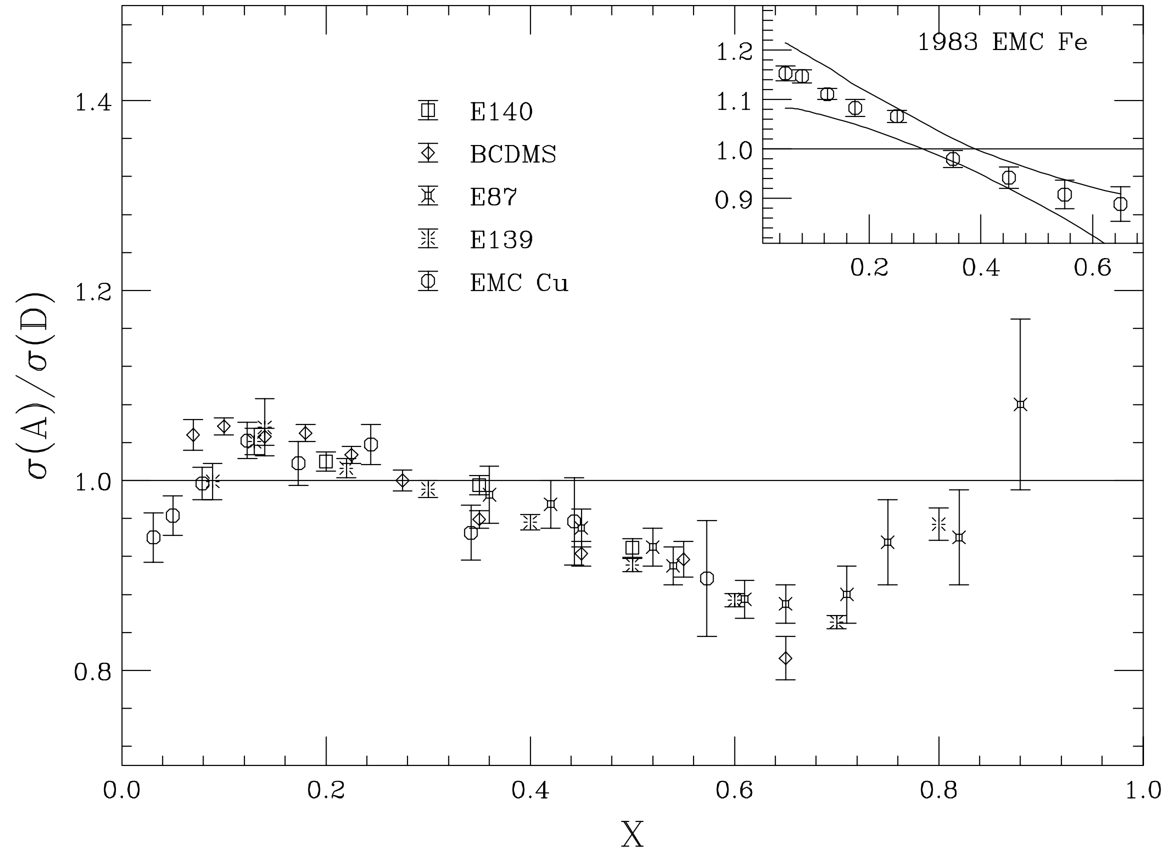

Figure 1.2: The embedded plot shows the first surprising EMC collaboration results. The plot in the forefront shows data from the SLAC experiments as well as from the second EMC collaboration. Both show cross section ratios, heavy targets to deuterium, plotted as a function of Bjorken x = $\frac{Q^2}{2M\nu}$.

1.2.2 Polarization Transfer

A direct method for measuring nuclear pions is to use polarized proton beams incident on a nuclear target, and measure the polarization transfer. By performing ($\vec{p}$,$\vec{p}'$) and ($\vec{p}$,$\vec{n}$) experiments one can isolate the spin-isospin longitudinal response function R_L.

The first of these experiments was carried out at the *Los Alamos Meson Physics Facility*(*LAMPF*). For the ($\vec{p}$,$\vec{p}'$) reaction [12] [13], they scattered polarized protons from *Pb* (lead) and *Ca* (calcium) and isolated the axial-longitudinal coupling of the proton to the pion field from all other couplings to get a complete set of polarization transfer observables [16] [17] [18]. From these observables, the longitudinal spin-flip probability (S_L) is determined for nuclear targets and compared to that from deuterium to extract the response functions.

Fig. 1.3 shows the ratio of response functions for the reaction. The transverse response function has no bearing on the enhancement; which is only sensitive to the longitudinal piece. The data was taken at $q \approx 350$ MeV/c which is where you pion enhancement is predicted to be observable, but there was no evidence found for pion enhancement.

The ($\vec{p}$,$\vec{n}$) reaction was taken as well on C(carbon) and Ca(calcium) at q = 340 MeV/c [15] [14]. In order to extract R_L, a probe is needed which is able to couple longitudinally to the spin of a nucleon as in the reactions ($\vec{p}$,$\vec{p}'$), ($\vec{p}$,$\vec{n}$), ($\vec{d}$,2$\vec{p}$), ($\vec{n}$,$\vec{p}$), (^3He,t), or the semihadronic processes such as $(e, e'\pi)$. ($\vec{p}$,$\vec{n}$) is purely

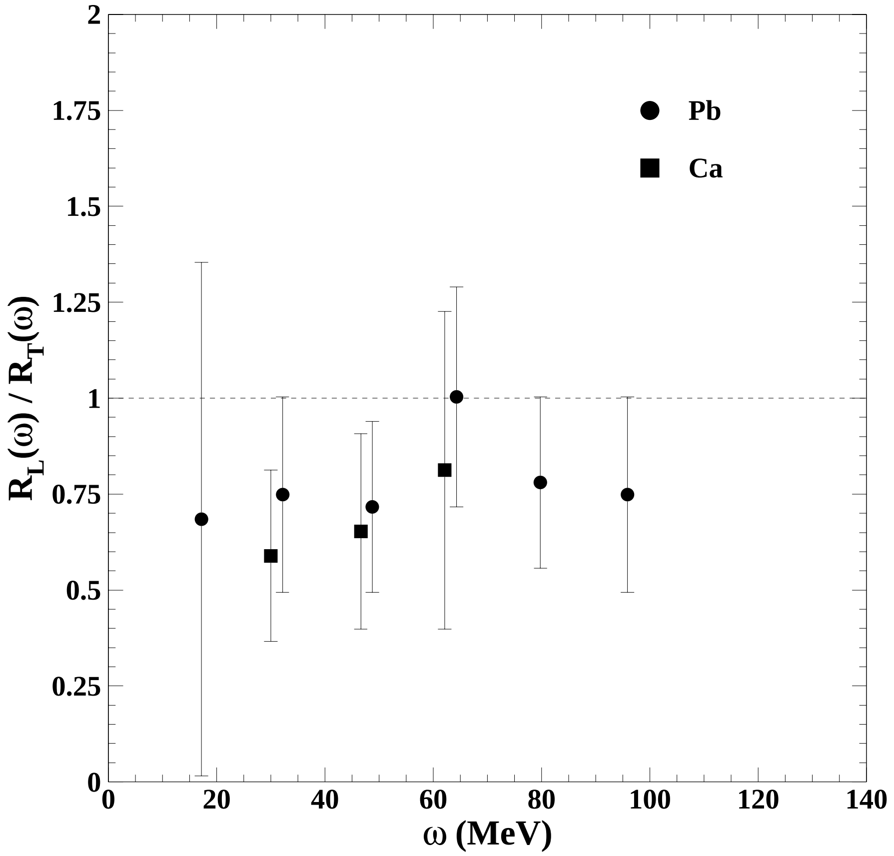

Figure 1.3: Ratio of longitudinal and transverse response functions for *Pb* and *Ca* from $(\vec{p},\vec{p}')$ reaction.

isovector and any pion enhancement due to pion exchange should be in a purely isovector channel. This should make the $(\vec{p},\vec{n})$ reaction an excellent choice for seeing pion enhancement, but fig. 1.4 shows no evidence for enhancement.

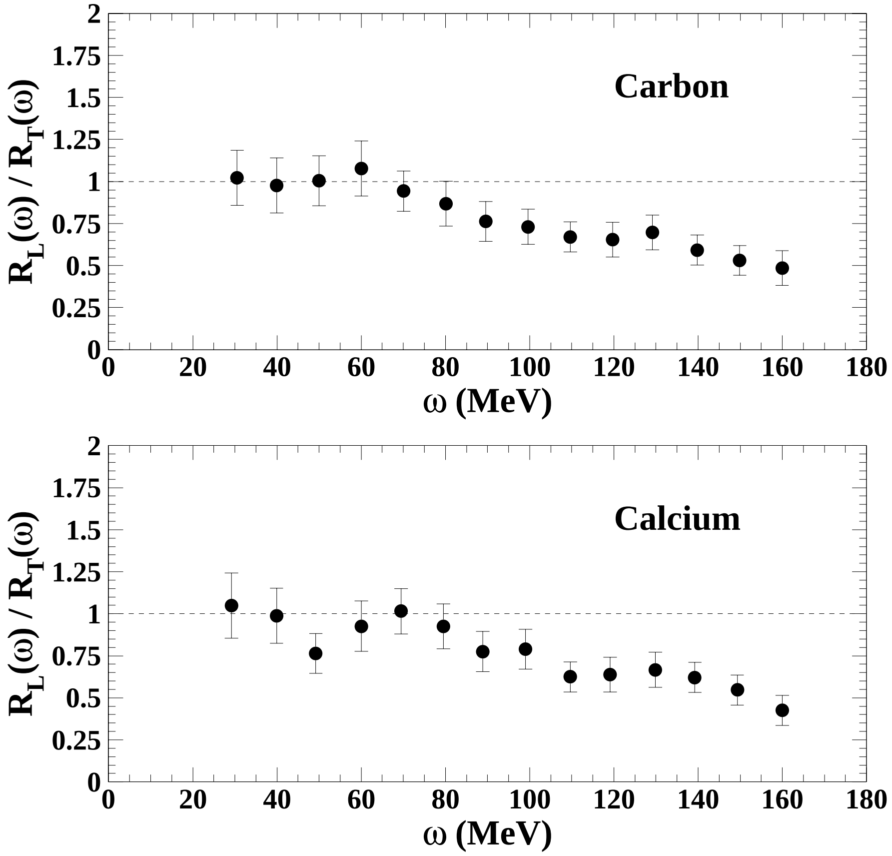

Figure 1.4: Ratio of longitudinal and transverse response functions for C and Ca from ($\vec{p}$,$\vec{n}$) reaction.

1.2.3 Drell-Yan Process

The $Drell-Yan$ process is the name associated with inclusive production of lepton pairs from hadron-hadron collisions, $q\bar{q} \rightarrow \gamma^* \rightarrow l^+l^-$. Fig. 1.5 illustrates the process; a quark and an anti-quark of the same flavor merge to form a virtual photon which produces a lepton pair. The pion consists of an equal amount of quarks and anti-quarks. Therefore an enhancement in the $Drell-Yan$ process

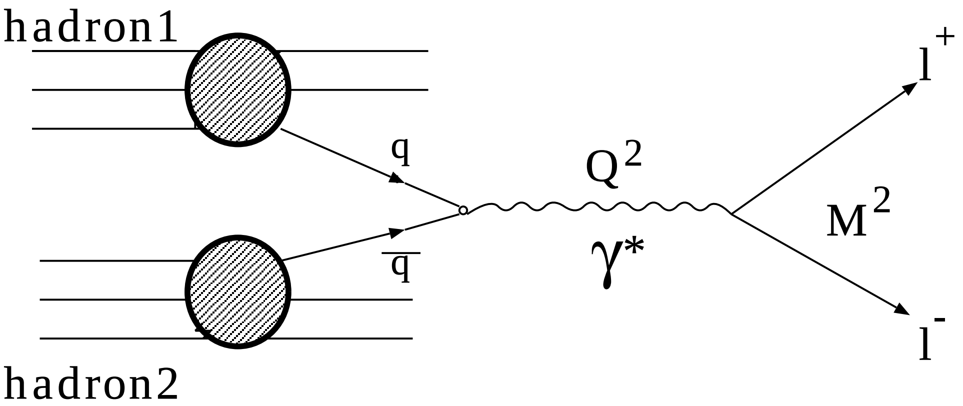

Figure 1.5: The Drell-Yan process.

from the pion field in proton-nucleus scattering would show up as an increase in the production of lepton pairs as compared to proton-deuterium scattering.

The experiment(E772) conducted at Fermi National Accelerator Laboratory collided protons with deuterium, carbon, calcium, iron, and tungsten [19], and measured muon pairs. They plotted the ratio of the yield from the heavy targets to deuterium versus $Bjorken\ x$ to find evidence of nuclear dependence. Fig. 1.6 shows the results from the experiment and indicates no evidence for pion enhancement at small x_t, $Bjorken\ x$ at the target.

1.2.4 Comments

The previous experiments could not conclusively give any evidence to support the idea of pion excess. On the other hand, we can not totally rule out the fundamental idea of the pion as the mediator of the nuclear force based on the previous results. Other effects such as shadowing, re-scattering, or final state in-

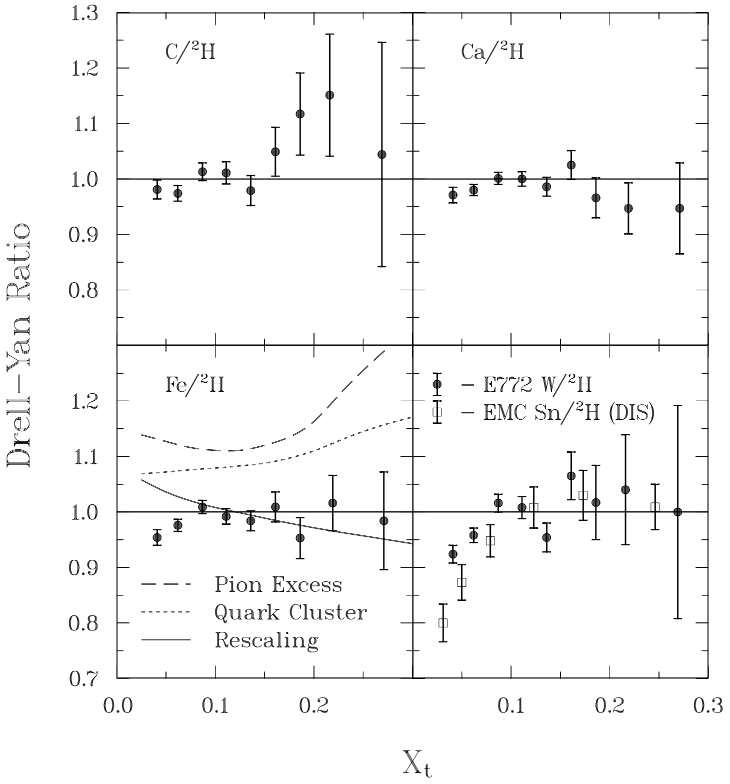

Figure 1.6: Ratio of μ pair production per nucleon as a function of x. The lines represent different models from EMC effect calculations.

teractions may be coming into play which may not have been fully understood in the analysis. Clearly, we can say that other methods are warranted in the search for nuclear pions. The goal of experiment **E91003** at Jlab was to look for mass-dependent effects by virtual pion knockout from nuclei.

Friman, Pandharipande, and Wiringa [5] performed a calculation to find the number of excess pions in nuclei. They started with the Lagrangrian:

$$\mathcal{L} = \mathcal{L}_{\mathcal{O}} + \mathcal{L}_{\mathcal{I}}. \tag{1.9}$$

L_O are for free particles and L_I are for the bound particles. For L_I we have

$$L_I = g\bar{\Psi}\Phi\Psi, \tag{1.10}$$

where

- g is the coupling constant;
- $\bar{\Psi}$ and Ψ are fermions; and
- Φ are scalars.

The scalar field describes the pions and it consists of both creation and annihilation operators

$$\Phi = \phi^{+}(x) + \phi^{-}(x), \tag{1.11}$$

where

- $\phi^{+}(\mathrm{x}) = \sum_k c_k \; a_k \; e^{-ikx}$; and
- $\phi^{-}(\mathrm{x}) = \sum_k c_k \; a_k^{+} \; e^{ikx}$.

To find the operator which tells the number of pions with momentum $\vec{k}_\pi$, our creation and annihilation operators are multiplied and integrate over all space, giving:

$$n_\pi(k) = \int \frac{d^3k}{(2\pi)^3} a_k^{+} a_k. \tag{1.12}$$

This number operator is used to get the expectation value with a system of A nucleons in the ground state $|A>$ to get an estimate of the pion excess. Table 1.2 lists the number of excess pions per nucleon predicted for nuclear matter and different nuclei.

Nucleus	$\langle \delta n_\pi \rangle$/A
Nuclear Matter, k_F=0.93	0.08
Nuclear Matter, k_F=1.13	0.12
Nuclear Matter, k_F=1.33	0.18
^2H	0.024
^3He	0.05
^4He	0.09
^{27}Al	0.11
^{56}Fe	0.12
^{208}Pb	0.14

Table 1.2: Pion excess (per nucleon) in nuclear matter and nuclei from Friman *et al* calculation.

The defining factor for Jefferson Lab Experiment **E91003**, which sought to verify the afore-mentioned calculation, is where the excess pions can be observed. The pion excess distribution from the above calculation indicates there should be an enhancement around pion momentums of 400-600 MeV/c, and a suppression around 100-300 MeV/c. This corresponds to k_π of 2-3 fm^{-1} and 0.5-1.5 fm^{-1}, respectively. An example of this distribution is in fig. 1.7

Thomas Jefferson National Accelerator Facility (Jlab) offers the services of a high duty factor electron accelerator, capable of acting as a direct probe into the virtual pion field. The object of the experiment here reported was to sample the nuclear pion field and try to find the predicted target-mass dependent effects.

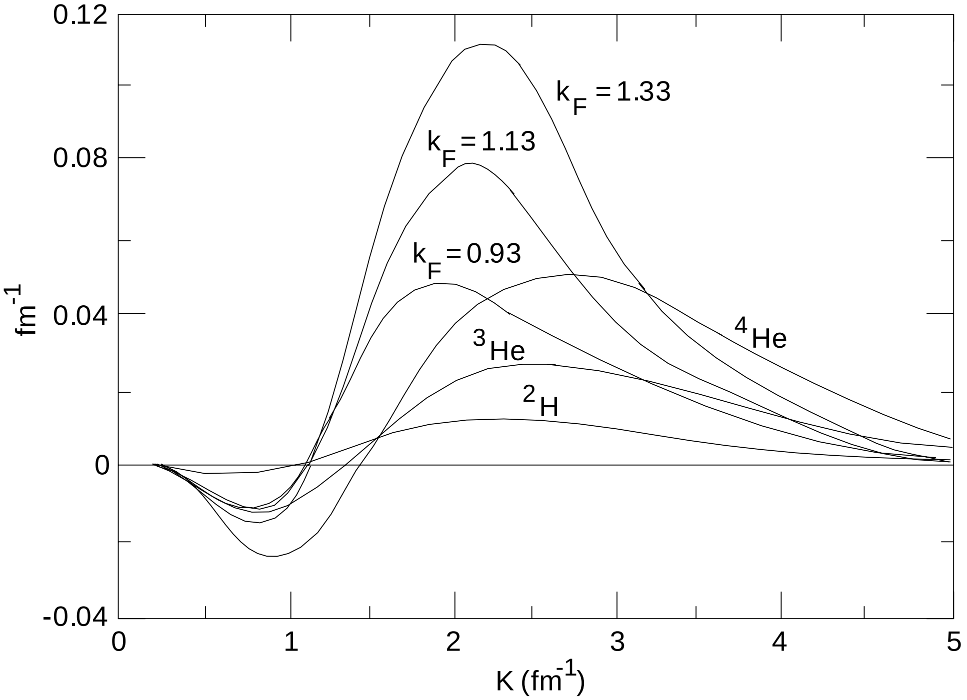

Figure 1.7: Pion excess vs. momentum distribution of excess pions.

sectionPion Electroproduction The process studied for **E91003** was A(e,e'x)B, where

- A represents the target which could have been ^1H, ^2H, or ^3He;
- x is the pion; and
- B is the final state, which could be a neutron, proton, triton, ^2H-n, or p-p-p, depending on the target and polarity.

1.2.5 Kinematics

The kinematic variables for $(e, e'\pi)$ are shown in fig. 1.8. An incident elec-

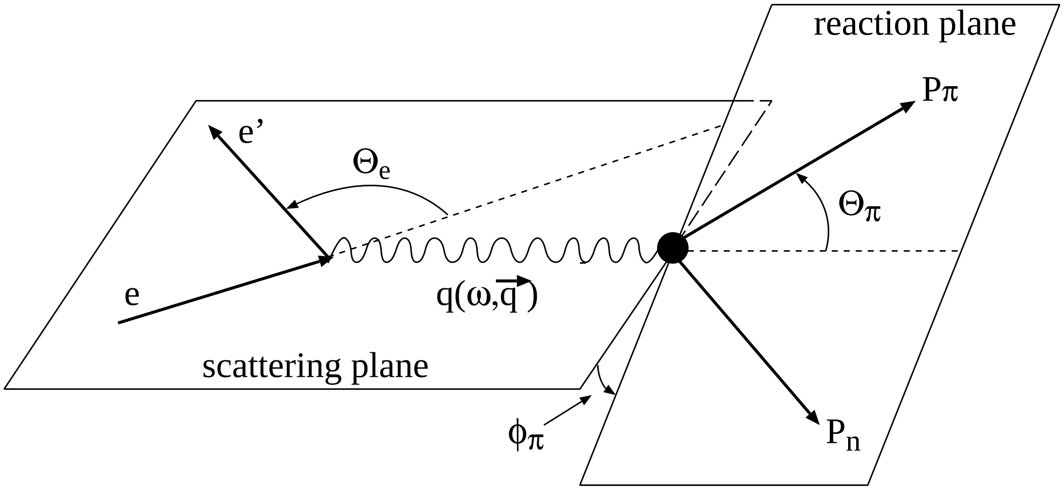

Figure 1.8: Schematic of (e,$e'\pi$) reaction for pion electroproduction.

tron scatters off a target by emitting a virtual photon γ^*. The electron scatters(e') at an angle Θ_e with respect to the direction of the incident beam. For this experiment, the electron was in the High Momentum Spectrometer (HMS) in Hall C. The pion travels at an angle Θ_π with respect to the virtual photon direction, and was detected in the Short Orbit Spectrometer (SOS). The *scattering plane* is defined by the incident and scattered electron. The *reaction plane* contains the pion and the residual nucleus. It is defined by the momentum transfer $\vec{q}$ of the virtual photon and the three momentum $\vec{p}$ of the pion. The angle ϕ_π represents the angle between the *scattering plane* and the *reaction plane*. The missing energy E_m and the missing momentum p_m are defined respectively as

$$E_m = E_e - E_{e'} - E_\pi, and \tag{1.13}$$

$$\vec{p}_m = \vec{q} - \vec{p}. \tag{1.14}$$

From these equations, one can construct the missing mass

$$M_m = \sqrt{E_m^2 - \vec{p}_m^{\,2}}. \tag{1.15}$$

The Lorentz invariant quantities used to describe the (e,$e'\pi$) reaction are defined as

$$\begin{aligned} -q^2 &= Q^2 = (e - e')^2; & (1.16)\\ s &= W^2 = (q + M_p)^2; and & (1.17)\\ t &= (q - P_\pi)^2. & (1.18) \end{aligned}$$

The four-momentum transfer q = (ω, $\vec{q}$) is defined by q = e - e'. The square of the four-momentum vector $q^2 = q_\mu q^\mu = \omega^2$ - $|\vec{q}^2|$ is defined by $q = (e - e')^2$. q^2 is always negative for electron scattering, but it is commonly written $Q^2 = -q^2$. s is the invariant mass of the virtual photon-target system. It is denoted as $W = \sqrt{s}$ and expressed as $W = \sqrt{M_p^2 + 2M_p^2\omega - Q^2}$. t is the square of the four-momentum transferred to the nucleon. It is written as

$$t = (E_\pi - \omega) - |\vec{p}_\pi|^2 - |\vec{q}|^2 + 2|\vec{p}_\pi||\vec{q}|cos\theta_\pi \tag{1.19}$$

t is always negative and is at a minimum when $\theta_\pi = 0$. The minimum value of -t increases for increasing Q^2 and decreasing W. s and t are called *Mandelstam* *varibles*. There are three total, with the third being

$$u = (q - P_n)^2. \tag{1.20}$$

These variables are used in nuclear physics to describe and study the structure of the scattering amplitude. Fig. 1.9 contains the kinematic diagrams for the *Mandelstam* variables. It should be noted that the diagrams represent specific reaction mechanisms, but the *Mandelstam* variables themselves are universal.

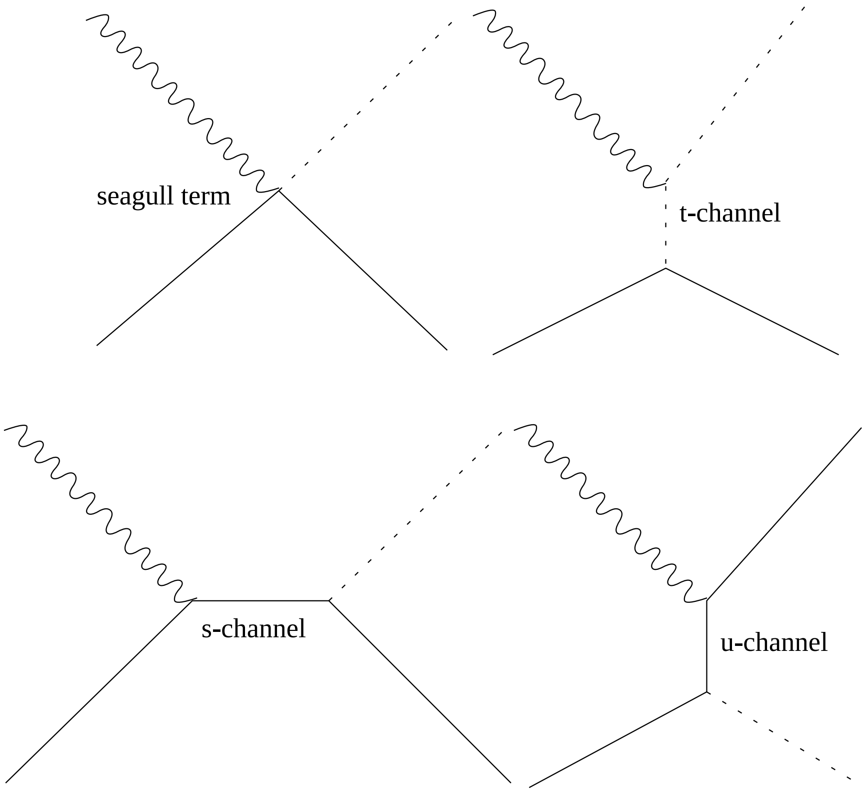

Figure 1.9: Pictorial representation of *Mandelstam* variables s, t, and u. For pion electroproduction these terms represent the contributing Born terms.

1.2.6 Born terms

The **O**ne **P**hoton **E**xchange **A**pproximation ($OPEA$) assumes a scattered electron emits a single virtual photon which couples to, in this case, a nucleonic system. The amplitude for this process is described as the sum of Feynman amplitudes for all reaction mechanisms that contribute to (e,$e'\pi$). In pion electroproduction, the Born (single photon exchange) terms are the first order processes that contribute to the amplitude. Referring back to fig. 1.9, the *seagull term* is needed to restore gauge invariance when using pseudovector coupling of the photon; the t-channel (or pole process) describes pion electroproduction as knocking out virtual pions via virtual photons. The s-channel process is known as the nucleon pole, and the u-channel process is called the crossed nucleon pole.

For our purposes, we are interested in the t-channel process because it is believed that, for small values of t, the longitudinal part of the cross section for pion electroproduction is dominated by the t-channel process (pole process). The direct interaction with virtual pions should be uniquely sensitive to nuclear pion excess. The t-channel process tell us the probability of a virtual photon interacting with a virtual pion of a certain momentum times the probability of finding the pion with that same momentum. Other t-channel processes contribute (see fig. 1.10), but are small compared to the top diagram.

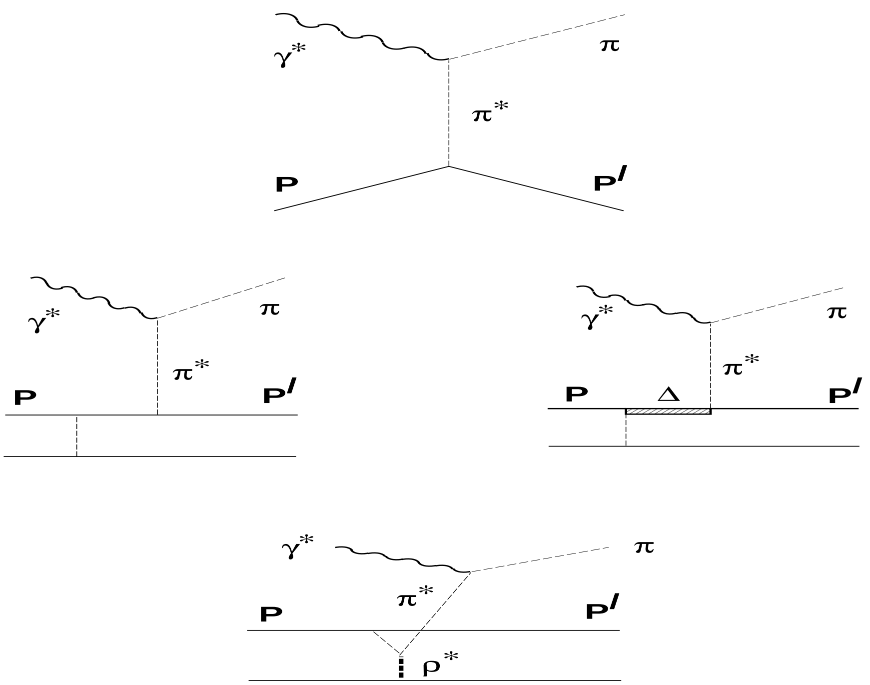

Figure 1.10: Pion electroproduction mechanisms in the t-channel. Charge scattering from a single nucleon is dominated by the pole term(top figure). Other reactions contribute, but are small compared to the pole term.

The longitudinal part of the cross section is given by

$$\sigma_L \approx \frac{-tQ^2}{(t-M_\pi^2)^2} g_{\pi NN}^2(t) F_\pi^2(Q^2,t), \tag{1.21}$$

where $g_{\pi NN}^2(t)$ describes the probability of finding a virtual pion with a given momentum, and $F_\pi^2(Q^2,t)$ describes the probability of having a virtual photon interact with a virtual pion. Finding enhancement of the pion field would be due to the modification of $g_{\pi NN}^2(t)$, which would consequently increase σ_L.

1.2.7 Pion Electroproduction Cross Sections

The pion electroproduction cross section can be written as a contraction between the leptonic and hadronic tensors:

$$\frac{d^6\sigma}{d\Omega_{e'}dE_{e'}d\Omega_\pi dE_\pi} = |\vec{p}_\pi|E_\pi\frac{\alpha^2}{Q^4}\frac{E_{e'}}{E_e}L_{\mu\nu}W^{\mu\nu}. \tag{1.22}$$

The leptonic tensor ($L_{\mu\nu}$) is calculated exactly using QED. The hadronic tensor ($W^{\mu\nu}$) contains all the information on the hadronic part of the scattering process. Another form of the cross section which has a direct relation with the cross section for real photons, and used for discrete final states, is

$$\frac{d^5\sigma}{d\Omega_{e'}dE_{e'}d\Omega_\pi} = \Gamma\frac{d^2\sigma}{d\Omega_\pi^*}, \tag{1.23}$$

where

$$\frac{d\sigma}{d\Omega_\pi^*} = \frac{d\sigma_T}{d\Omega^*} + \varepsilon_L\frac{d\sigma_L}{d\Omega^*} + \sqrt{2\varepsilon_L(\varepsilon+1)}\frac{d\sigma_{LT}}{d\Omega^*}\cos\phi + \varepsilon\frac{d\sigma_{TT}}{d\Omega^*}\cos 2\phi \tag{1.24}$$

is the center-of-mass cross section,

$$\Gamma = \frac{\alpha}{2\pi^2}\frac{E'K_{eq}}{EQ^2(1-\epsilon)} \tag{1.25}$$

is the flux of the transverse virtual photons, and

$$\varepsilon = \frac{1}{1 + 2\frac{|\vec{q}|^2}{Q^2} tan^2\frac{\theta_e}{2}}. \tag{1.26}$$

ε describes the relative longitudinal flux of polarized virtual photons. The factor K_{eq} is called the equivalent photon energy and is typically set equal to $(W^2 - M_p^2)/2M_p$. This is the energy a real photon needs to produce a system with invariant mass W. The cross section $\frac{d\sigma}{d\Omega^*}_\pi$ depends on three Lorentz invariant variables: Q^2, the four-momentum transferred to the target; W, the invariant mass of the recoiling hadronic system; and the Mandelstam variable t, the momentum transferred to the nucleon.

The contraction of the leptonic and hadronic tensors, discrete states, results in the formation of four structure functions (eqn. 1.24): σ_T-cross section of the unpolarized incident photon beam, σ_L-cross section from the longitudinal components of the virtual photon, σ_{LT}-cross section due to the interference effects between the longitudinal and transverse parts of the the cross section, and σ_{TT}-the asymmetry contribution of a transversely polarized beam. The longitudinal-transverse (LT) and the transverse-transverse (TT) cross sections have a dependence on the angle out of the scattering plane, and average to zero in parallel kinematics ($\theta_{pq} = 0$), leaving only σ_L and σ_T in the cross section. These terms can be decomposed via a Rosenbluth type separation. A Rosenbluth type separation is achieved by varying ε while keeping Q^2, t, and W constant. ε is varied by changing the electron beam energy and scattering angle. Plotting the reduced cross section as a function of ε, and doing a least square fit to the linear dependence there of gives the longitudinal component as the slope and the transverse component as the y-intercept.

For nuclear targets it is also necessary to account for the Fermi momentum distribution between nucleons in a nucleus. Introducing another degree of freedom changes the 5-fold cross section into a 6-fold cross section.

$$\frac{d^6\sigma}{d\Omega_{e'}\,dE_{e'}\,d\Omega_\pi\,dP_\pi} = \Gamma\frac{d^2\sigma}{d\Omega_\pi^* dP_\pi}. \tag{1.27}$$

The extra degree of freedom in this case is the final pion momentum. By integrating over P_π, the nuclear cross section can be expressed as 5-fold, making it possible to compare with hydrogen targets.

1.3 Experiment E91003 Kinematics and Goals

Experiment **E91003** ran in Hall C at Jefferson Lab from February to April 1998. The goal was to measure the longitudinal component of the pion electroproduction cross sections for ^2H and ^3He, and compare them to the longitudinal component of H to look for target-mass dependent effects (*ie* pion excess).

Electrons with energies between 0.85 and 3.25 GeV were scattered off cryogenic targets. The scattered electrons were detected in the **H**igh **M**omentum **S**pectrometer and the charged pions were detected in the **S**hort **O**rbit **S**pectrometer. Both the SOS and HMS had identical detector packages consisting of

- drift chambers for path trajectory,
- scintillator hodoscopes for triggering and time-of-flight particle identification,
- Čerenkov counter for particle identification, and
- shower counters for e/π particle identification.

Pions were identified in the *SOS* by using time-of-flight and *HMS-SOS* coincidence timing from information received by the scintillator hodoscopes.

E91003 measured the longitudinal component of the cross section at different values of the nucleon recoil momentum k_π, where pion enhancement (and suppression) were expected to be prominent. Data was taken at the same Q^2 in parallel kinematics (θ_{pq}=0). There were two W values of 1.15 and 1.6 GeV. The change in W was due to its high correlation with k_π. At each value of k_π, Q^2 and W were held constant while the virtual photon longitudinal polarization ε was varied. This allowed us to extract the longitudinal component of the cross section via a Rosenbluth type separation.

E_{Beam}(GeV)	ε_L	W(GeV)	$Q^2(GeV/c)^2$	k_π
0.845	0.437	1.15	0.4	0.47
1.645	0.861	1.15	0.4	0.47
1.645	0.490	1.60	0.4	0.20
3.245	0.894	1.60	0.4	0.20

Table 1.3: E91003 kinematics

CHAPTER 2

Experimental Apparatus

2.1 Overview

The Nuclear Pion Experiment (**E91003**), A Study of Longitudinal Charged Pion Electroproduction in ^1H, ^2H and ^3He, was performed at the Thomas Jefferson National Accelerator Facility (Jefferson Lab) utilizing its 100% duty factor electron beam. E91003 involved colliding high energy electrons onto hydrogen, deuterium, and helium targets, knocking out an electroproduced pion from the target nucleus. The electroproduced pion was detected in coincidence, before their in-flight decay, with the scattered electron, using the Hall C spectrometers. Empty target cells made of aluminum were used for background measurements. (**E91003**) was completed in the spring of 1998. The experimental equipment used in (**E91003**) was the standard equipment available in Hall C consisting of

- target assembly (this includes the targets themselves);
- a pair of focusing electromagnetic spectrometers, namely:
  - the High Momentum Spectrometer (**HMS**),
  - and the Short Orbit Spectrometer (**SOS**).

  Each one these spectrometers has its own set of detectors comprised of:

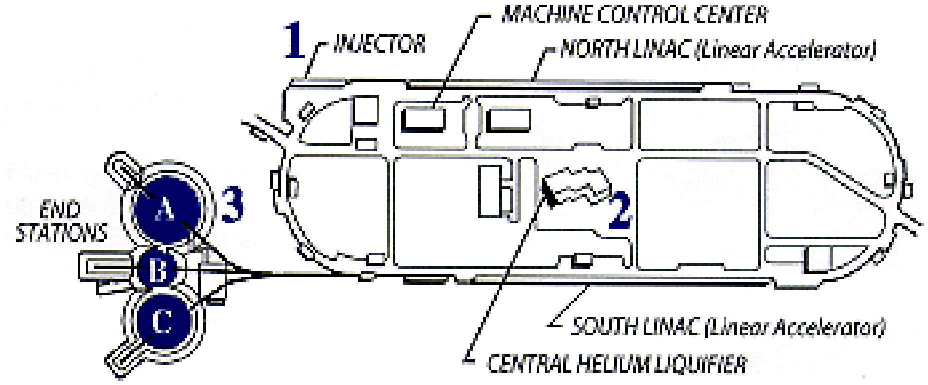

Figure 2.1: Jlab Accelerator

∗ Drift chambers,

∗ Scintillator hodoscopes,

∗ Gaseous Čerenkov counter,

∗ Shower counter.

All the systems above will be described in more detail in the rest of this chapter and they have been discussed in previous dissertations [32] [29] [31].

2.2 Accelerator

The Thomas Jefferson National Accelerator Facility (Jlab) accelerator, shown schematically in Fig. 2.1, produces an unpolarized, high-current, continuous wave beam of electrons. The accelerator has a ‘racetrack’ configuration consisting of a 45 MeV injector, a pair of linear accelerators, a switchyard, and three experimental halls. Electrons from the injector are sent into the north linac, these electrons are accelerated through superconducting niobium RF resonant cavities and gain 400 MeV in energy. The beam is then sent through the east arc and into the south linac where it gains another 400 MeV. At this point the beam can either be sent into the experimental halls via the beam switchyard, or it can be steered through the west arc and passed the linacs to gain another 800 MeV. This can be done up to five times yielding a beam energy in the range of 845 MeV to 4045 Mev. The same linacs are used for each cycle, but the east and west arcs use different magnets depending on how many passes the beam has taken. The accelerator is capable of beam currents up to 200μA to the three experimental halls simultaneously. The accelerator produces short beam bursts at a repetition rate of 1497 MHz, resulting in a 2 ns bunch structure in each hall. The beam current for each hall can be adjusted based on the experiment specifications. The beam is considered to be a continuous-wave (CW, 100% duty factor) because the time spread in the arrival of events in the detectors of the two spectrometers is larger than the time between pulses.

2.2.1 Hall C Beamline

The Hall C Beamline cares the beam from the beam switch yard to the target. The beamline is 41.6 m long and consists of 8 dipoles, 12 quadrupoles, 8 sextupoles, and 8 pairs of beam correctors. Several pieces of equipment are used along the Hall C beamline, they are

- Superharps
- Beam Position Monitors

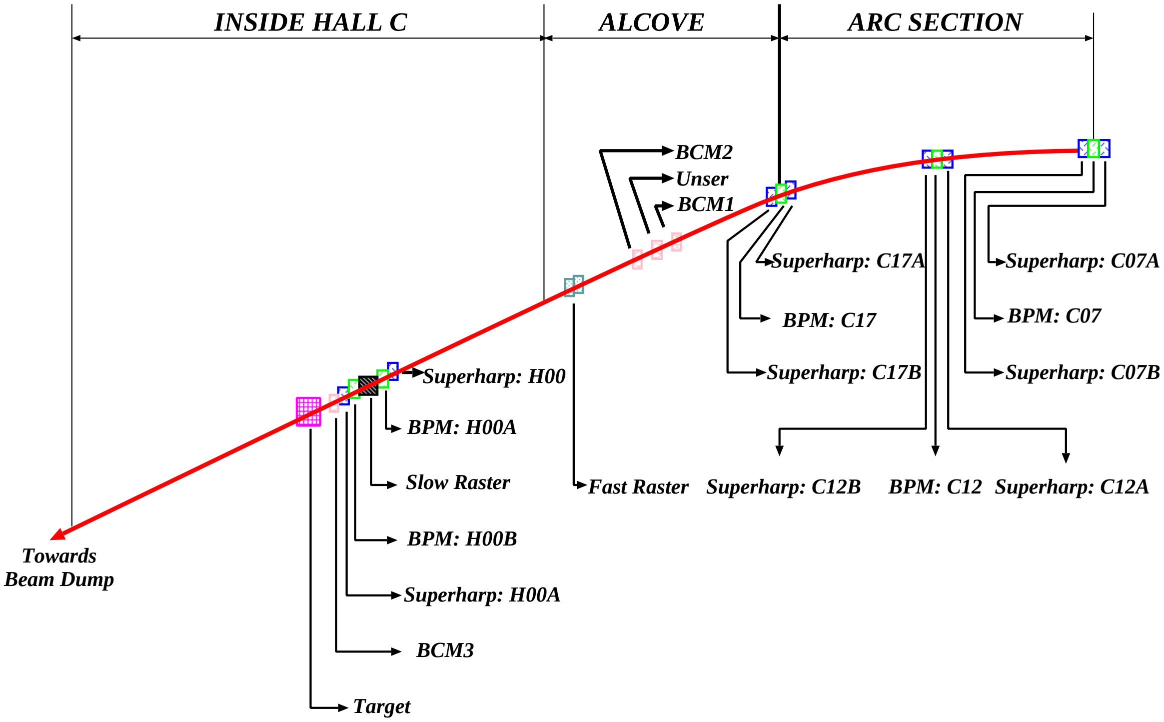

Figure 2.2: A schematic showing the components and layout of the Hall C arc beamline.

- Beam Energy Measurement
- Beam Current and Unser Monitors
- Target Raster

I will discuss each of these monitors in more detail.

2.2.1.1 Superharps

The superharp consisted of a frame with three tungsten wires. Two of the wires are vertical and the other one is horizontal. the frame is moves in and out of the path of the beam to determine the beam position. The vertical wires

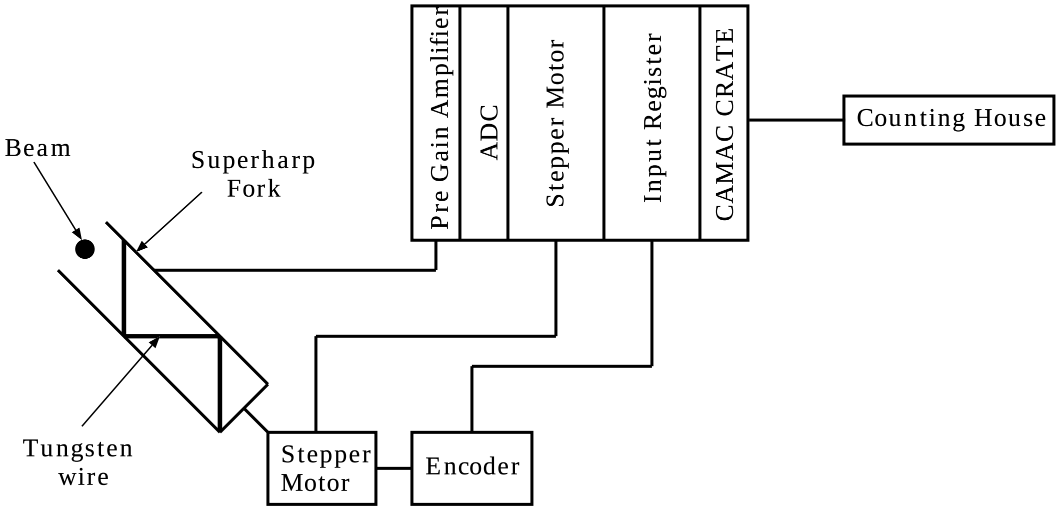

Figure 2.3: Hall C Superharp

measure the horizontal position of the beam, while the horizontal wires measure the vertical position on the beam. Wires are connected to an ADC (Analog–to–Digital Converter), while an encoder determines the position where the beam intercepts the wire. The superharp is accurate to $\approx 10\mu m$. This is satisfactory for reproducing the position and width of the beam, which is $\sim 100\mu m$. We could not make measurements with the superharps during data taking because such measurements are destructive.

2.2.1.2 Beam Position Monitors

In addition to the "Superharps", Beam Position Monitors (BPMs), are used to determine the position of the beam. As shown in Fig. 2.2, the beam position was monitored with several BPMs. Unlike the superharps, the BPMs are able to take measurements during data production. The BPM is basically a resonant cavity with four antenna that are rotated ±45° from the vertical and horizontal. The mechanical parameters of the cavity can be tuned to the accelerator operating frequency. This will ensure that the electron beam passing through the cavity will excite TEM modes. The sensitivity of the modes are proportional to the distance of the beam to the center of the cavity. The BPM is mounted in the beamline so its axis will coincide with the nominal axis of the beam. As stated earlier, the BPMs were used to read out the position continuously and the superharp was only performed every few hours as a check. The superharp had a smaller absolute error on the beam position, but using a combination of both monitors allowed for a ±1 mm absolute uncertainty of the beam position with a relative uncertainty of $\sim 0.1 - 0.2$ mm.

2.2.1.3 Beam Energy Measurement

Having a good understanding of the beam energy is vital when doing electron scattering experiments. Since we have acquired information about the position and direction of the beam from superharp and BPM measurements, we can use this information along with the knowledge of the field integral $\int B * dl$ to calculate the electron beam energy from the relationship:

$$P = \frac{e}{\Theta_{arc}} \int B \, dl \ \ , \tag{2.1}$$

where p is particle momentum, e is the electron charge and Θ_{arc} is the angle of the arc (34.4°). The accuracy of the Hall C beam energy measurements were on the order of 10^{-3}.

2.2.1.4 Beam Current and Unser Monitors

Three Beam Current Monitors (BCMs) were used during **E91003** - BCM1, BCM2 and BCM3. These BCMs measured the radio frequency of a resonant cavity in the beamline. All of the beam current monitors are geometrically the same. Basically they were stainless steel cylinders placed in the beamline. They were positioned so the beam could go through the center of one end of the cylinder and out the center of the other end. The characteristics of the beam in Hall C excited the 1497 MHz TM_{010} resonance mode. This mode was the most favorable because it doesn't disturb the beam position. Of the three beam current monitors only BCM1 and BCM2 had reasonable gain stability, and of these two BCM2 proved to be the more precise monitor. For that reason BCM2 was used to record the charge for the data analysis.

The BCMs had to be calibrated to ensure that the gain remained stable. These calibrations were done every couple of days using the unser monitor. The unser monitor is made up of two transformers. The first transformer measures the alternating current (AC) fluctuations while the other transformer measures the direct current (DC) fluctuations. A simple schematic of the unser is shown in

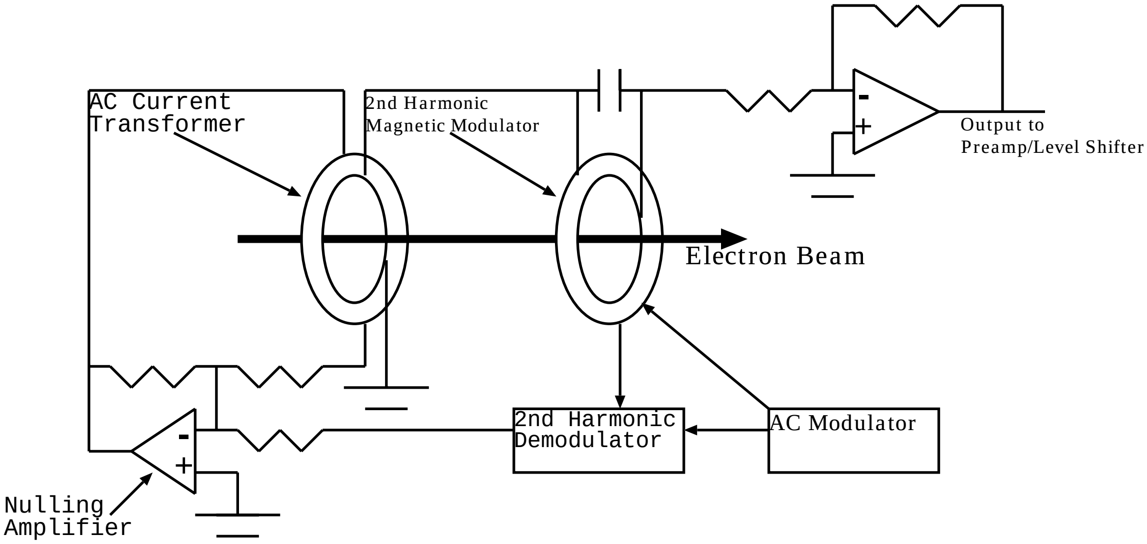

Figure 2.4: Simple schematic of Unser monitor and electronics.

Fig. 2.4. An AC modulator drives the transformers through its hysteresis curve. The hysteresis curve stays symmetric as longs as there are no DC fluctuations. Once a DC fluctuation is present, the hysteresis curve loses its symmetry and a small amount of current is forced through a feedback loop to restore the symmetry. The amount of current it takes to restore the symmetry of the hysteresis curve is the output of the unser monitor. This output is sent to Voltage–to–Frequency (V–F) converter and stored in the scaler files.

2.3 Target

E91003 used liquid hydrogen, deuterium, and helium-3 cryogenic targets for data taking. E91003 was the first to use helium-3 in Hall C. After the beam traveled through the Hall C beam arc and into the the experimental hall it encountered the

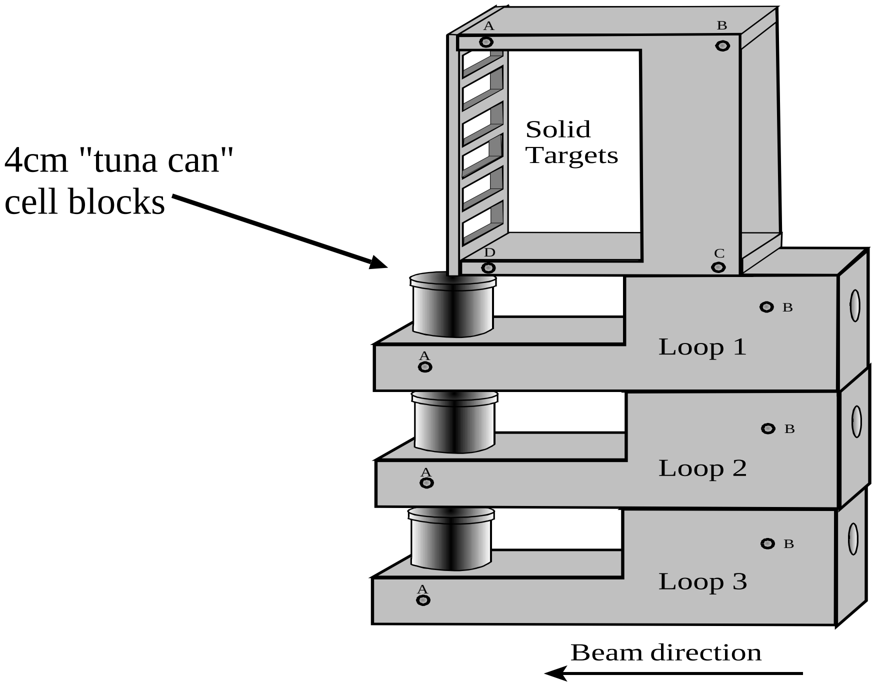

Figure 2.5: A schematic showing the layout of the Hall C cryotarget.

scattering chamber where the cryogenic targets are located. The cryogenic target is a set of loops through which the hydrogen, deuterium, or helium flow. The flow of the gases are regulated by using fans at various location throughout the loop. The targets are cooled through heat exchange with 15K liquid helium, and stabilized by using heaters. A high powered heater compensated for the heat output of the beam, while low powered heaters made fine adjustments to the variations in the cooling system. The nominal temperature and pressure for hydrogen is 19 K and 24 psi, for deuterium it was 22 K and 20 psi. Liquid helium had a nominal operating temperature and pressure of 5.5K and 130psi. Although helium-3 was not a true liquid, the temperature and pressure it operated at made it exhibit liquid-like

Target	Temperature (K)	Density (g/cm^3)	Purity (%)
Hydrogen	19.0 ± 0.05	0.07230 ± 0.0003	99.8 ± 0.10
Deuterium	22.0 ± 0.05	0.16708 ± 0.0007	99.2 ± 0.13
Helium-3	5.50 ± 0.05	0.07670 ± 0.0004	99.7 ± 0.13

Table 2.1: The target properties of hydrogen, deuterium, and helium-3 targets under normal running conditions.

properties. The target configuration is in the shape of a "tuna can" approximately 4 cm long. The fluctuations of the target density was minimized by rastering the electron beam. In order to estimate the contribution of the target walls in data, empty targets or "dummy targets", were included in the target stack. These "dummy targets" consisted of aluminum plates ten times thicker then the target cell walls. The temperature was kept constant to 0.1% throughout the experiment and the uncertainty in the target density was on the order of 1%.

2.4 HMS and SOS spectrometers

Two spectrometers were used for this experiment. Scattered electrons were detected in the High Momentum Spectrometer (HMS) and the scattered pions were detected in coincidence in the Short Orbit Spectrometer (SOS). This is the standard detection system in Hall C at Jefferson Lab.

All the data for E91003 was taken using an octagonal collimator, that was placed between the target and the spectrometer to better define the solid angle acceptances. The collimators was replaced with a set of sieve slits for optics studies.

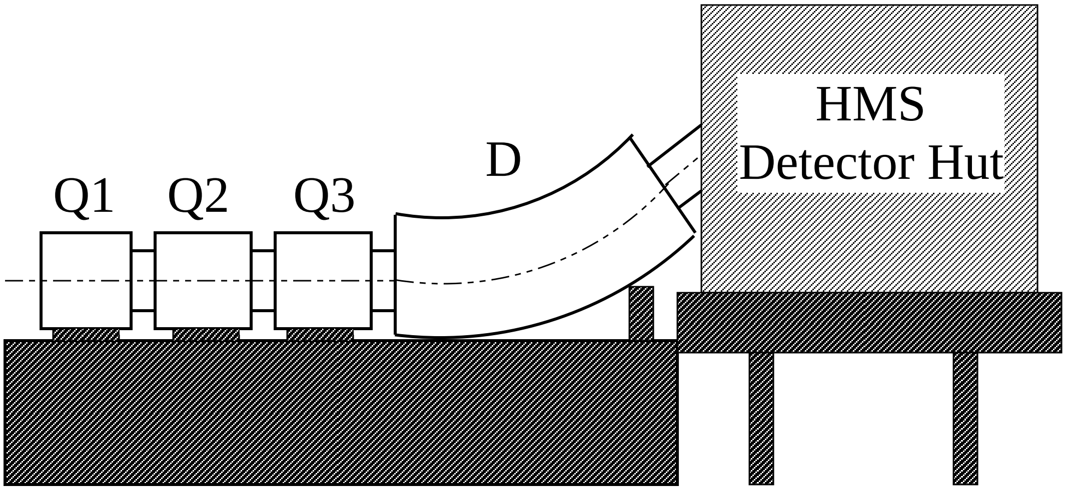

Figure 2.6: Side view of HMS Spectrometer.

Both the HMS and SOS were calibrated for point-to-point tuning, which means that an event from the target would be focused to a point on the focal plane of the spectrometer.

2.4.1 High Momentum Spectrometer (HMS)

The HMS spectrometer consist of three quadrupoles and one bending dipole magnet. These superconducting magnets are in a QQQD configuration. The quadrupoles are used for focusing the beam, while the dipole causes a vertical bend of 25° for the central ray. The quadrupoles are current regulated, and the dipole is regulated using a NMR probe. The current and magnetic field are controlled remotely.

The spectrometer and the detector hut are mounted on a carriage that rotates about the scattering chamber. The HMS was used to detect the scattered electrons for E91003.

Maximum central momentum	7.4 gev/c
Momentum bite$[(p_{max} - p_{min})/p_0]$	18 %
Momentum resolution $[\delta p/p]$	< 0.1 %
Solid angle (no collimator)	> 6 msr
Angular acceptance - scattering angle	±32 mr
Angular acceptance - out of plane	±85 mr
Min. central scattering angle	12.5°
Scattering angle reconstruction	0.4 mr
Out of plane angle reconstruction	0.9 mr
Useful extended target acceptance	10 cm

Table 2.2: Summary of the HMS characteristics.

2.4.2 Short Orbit Spectrometer (SOS)

The SOS spectrometer was used to detect pions in coincidence with the HMS. The short orbit spectrometer was designed with a short flight path to detect short lived particles such as pions and kaons.

In addition to having a short flight path the SOS has a large acceptance in both scattering angle and momentum. The SOS consist of a quadrupole (QS) and two dipoles (BM01 and BM02) creating a QDD configuration. The first dipole has an upward bend angle of 33° and the second dipole has a downward bend of 15° resulting in a slope of 18° through the detectors. The magnetic tune used was point-to-point in both the horizontal and dispersive directions.

The magnetic field in the magnets are regulated by using hall probes.

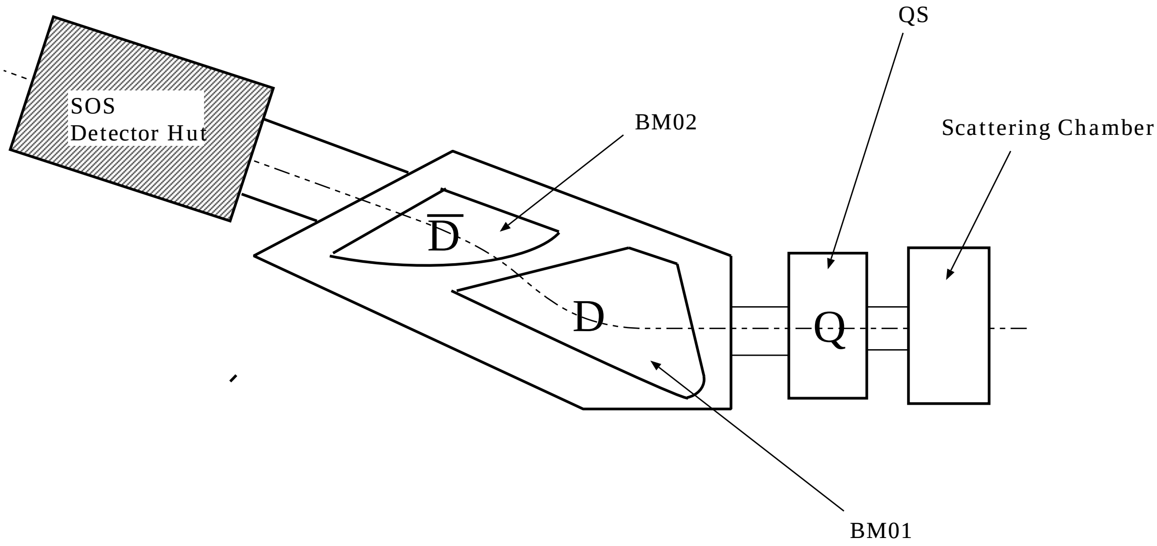

Figure 2.7: Side view of SOS Spectrometer.

Maximum central momentum	1.8 gev/c
Momentum bite$[(p_{max} - p_{min})/p_0]$	40 %
Momentum resolution $[\delta p/p]$	< 0.1 %
Solid angle (no collimator)	~ 9 msr
Angular acceptance - scattering angle	±60 mr
Angular acceptance - out of plane	±40 mr
Min. central scattering angle	14.5°
Scattering angle reconstruction	0.5 mr
Out of plane angle reconstruction	1.0 mr
Useful extended target acceptance	4 cm

Table 2.3: Summary of the SOS characteristics.

2.5 Detector Package

The detector packages of the short orbit spectrometer (SOS) and the high momentum spectrometer (HMS) and virtually identical. Both detector packages consist of two multiwire drift chambers, two sets of X-Y scintillator hodoscopes, a Čherenkov counter, and a lead glass shower counter. The drift chambers were used for tracking charged particles, the hodoscopes were used for time-of-flight; particle ID; and to form a primary trigger, the Čherenkov counter was used to discriminate between different charged particles. The shower counter was used for energy measurements. A schematic of the Hall C detector package is shown in Fig. 2.8. The detectors are discussed in detail in this chapter.

2.5.1 Multiwire Proportional Drift Chambers

Two drift chambers were used to provide tracking information in the HMS and SOS. Each chamber contained six planes of wires as shown in Fig. 2.9.

The spacing between the sense wires was 1 cm. The drift chambers functioned as an ionization detector. The chambers are filled with a argon-ethane gas mixture. Charged particles that pass through the chamber will ionize the gas molecules, freeing electrons that will accelerate to the nearest anode wire. The maximum drift time with this gas mixture was about 150 ns. The charge from the wires are amplified and discriminated, and the information is collected by a fastbus Time-to-Digital Converter (TDC).

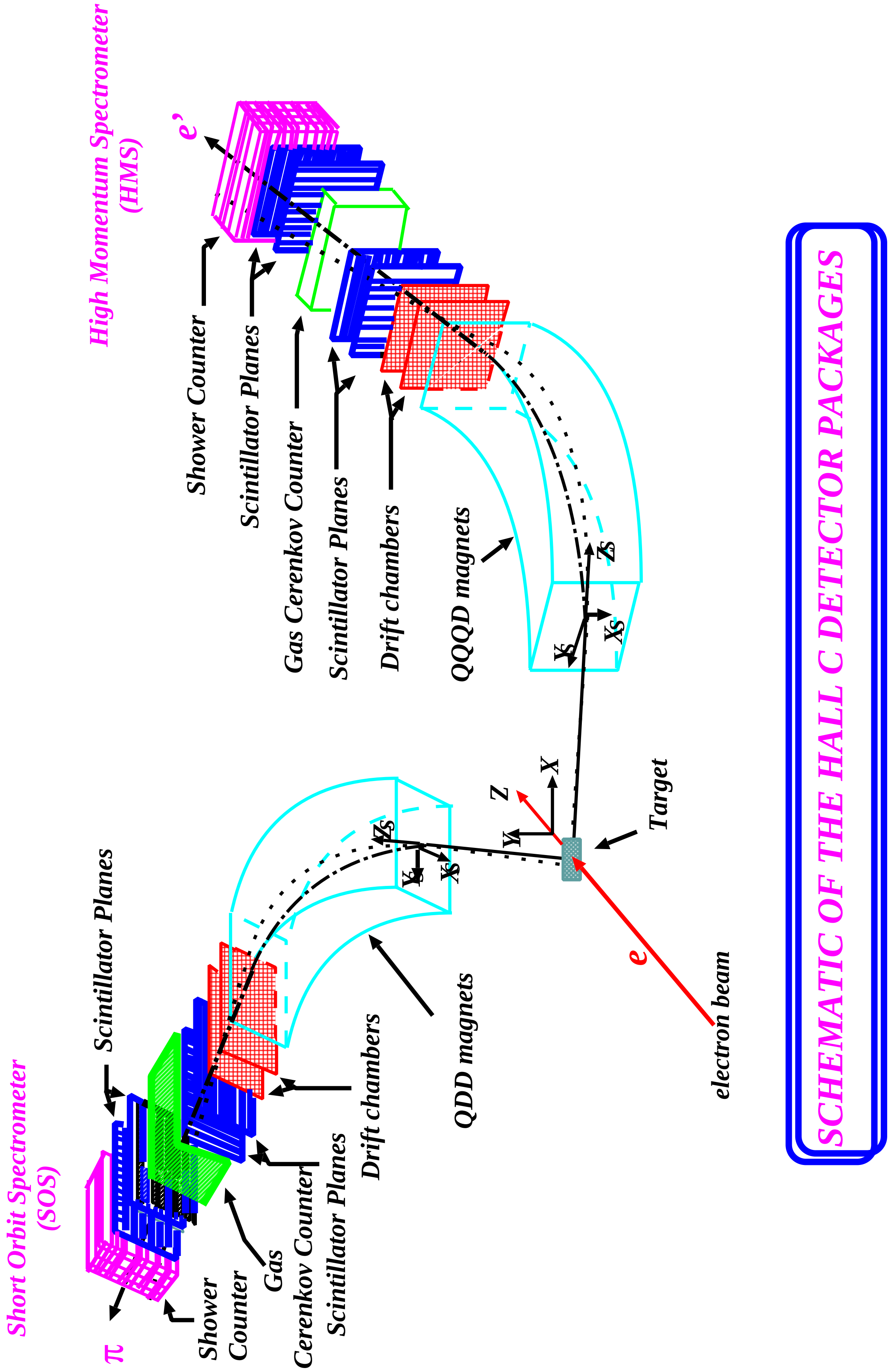

Figure 2.8: Hall C Spectrometer Detector Packages.

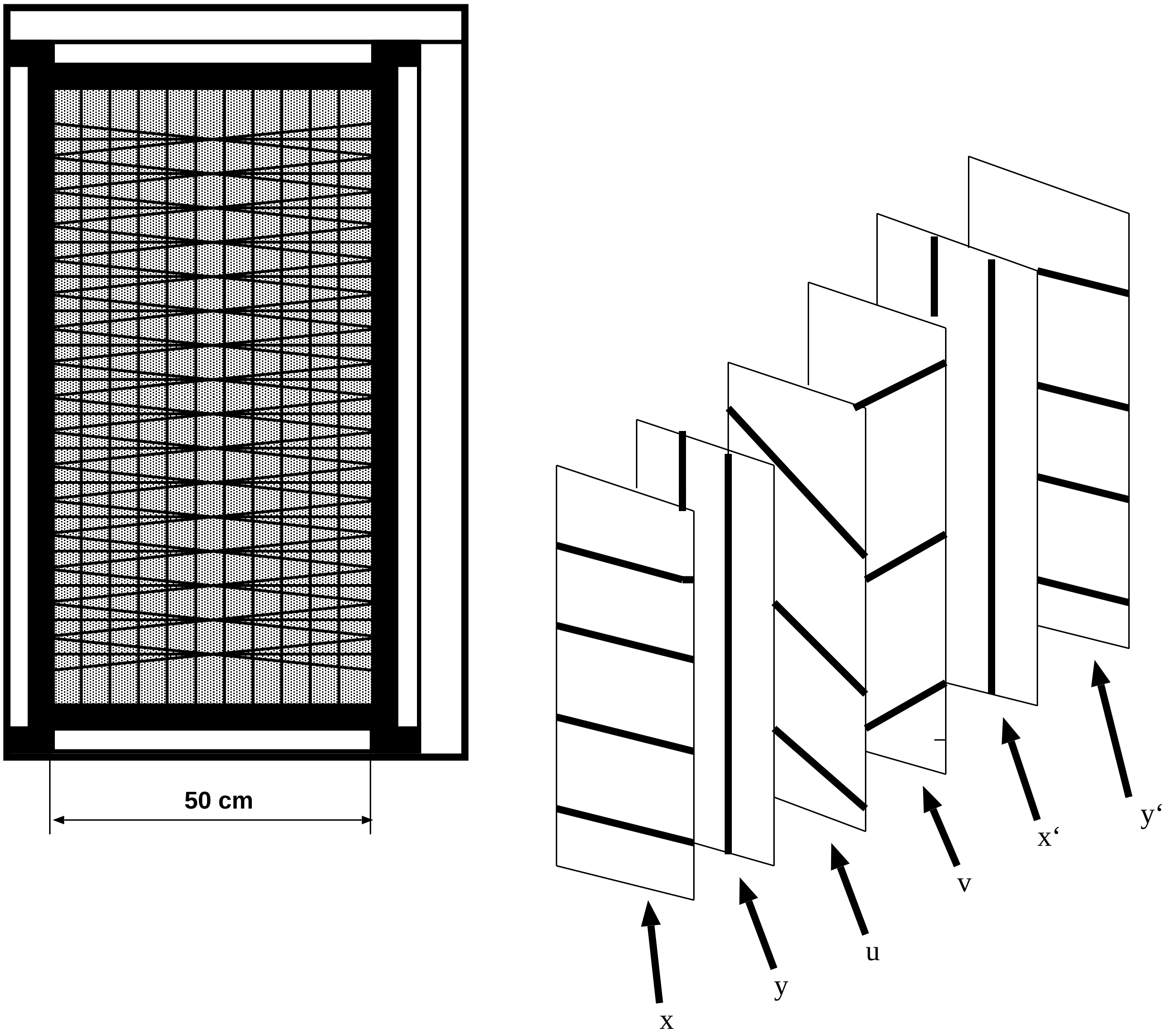

113 X,X’ wires.
107 U,V wires.
52 Y,Y’ wires.
1.000252 cm wire spacing.

Figure 2.9: Schematic view of multiwire proportional drift chamber.

2.5.2 Scintillator Hodoscopes

There are two sets of hodoscopes in each detector package, each set consist of two scintillator planes (X and Y). The individual planes contain 9-16 paddles. This position is used to ensure that the hodoscope hits correspond to the chosen focal plane track. The location of the hit on the scintillator, is taken from the tracking information. The track along the length of of the scintillator plane is used to make path length corrections that correspond to the time it takes light to propagate to the photomultiplier tubes, which are located at either end of the scintillator.

The hodoscope planes are 2 m apart, which makes a sufficient distance for time-of-flight (TOF) calculations. The HMS has 32 scintillators in the x-plane and 20 scintillators in the y-plane. The SOS has 9 scintillators in the front x-plane, 16 scintillators in the back x-plane and 9 scintillators in the y-plane.

In the HMS the hodoscopes were used to trigger the data acquisition system. The signals from the photomultplier tubes were sent to a discriminator and then to time-to-digital (TDC) converters, VME scalers and Lecroy 4654 logic modules. A requirement that 3 out of 4 scintillator planes had to be fired before data acquisition system was triggered. This layout of the hodoscope electronics are shown in Fig. 2.10.

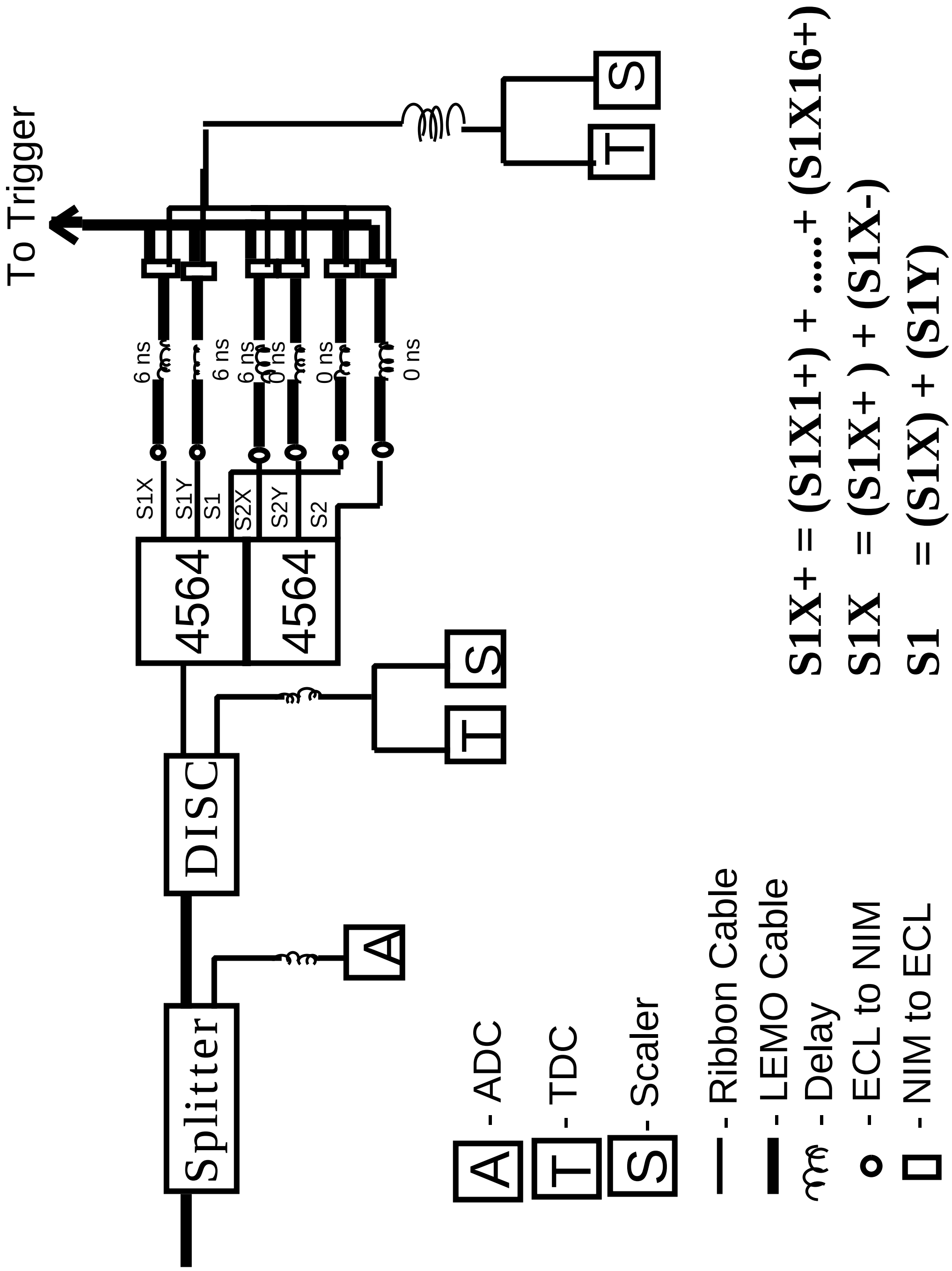

Figure 2.10: Scintillator hodoscope electronics

2.5.3 Gas Čherenkov Detector

The Čherenkov detector is used to discriminate between charged particles. In a medium, other then air, with an index of refraction n greater then air a charged particle can exceed the speed of light in that medium. When this occurs Čherenkov light is radiated at a fixed angle. This angle can be related to the index of refraction(n) for the medium and the velocity (β) by:

$$cos\Theta = \frac{1}{\beta n} \tag{2.2}$$

The HMS Čherenkov detector is a large cylindrical tank 152 cm long with a diameter of 150 cm. The detector is located between the first and second set of scintillator hodoscopes. The detector was filled with CO_2 gas at room temperature and atmospheric pressure. Using CO_2 yielded an index of refraction of $n = 1.00041$ and a velocity of $\beta = 0.999593$. Operating under these conditions the Čherenkov detector is very sensitive to electrons and insensitive to heavier particles, such as pions and kaons.

The light that is emitted from a radiating particle is collected by reflecting it off two mirrors, located in the back of the detector, into two PMTs on the side of the cylinder. The light is detected with two 5-inch Burle 8854 PMTs. Once the signals are sent to the counting house they are split into two sets. One set is sent through cable delay to an ADC and the other set is summed in a linear fan-in (Phillips 740) and then discrimated to give NIM logic signals. The logic signals Č and NOT Č are sent to a pretrigger logic module were it is used in conjunction with signals from the shower counter in order to reject pions. In the HMS the electron detection efficiency for a 2 photoelectron cut was ~ 98 %.

The SOS gas Čherenkov was designed and built at the University of Colorado. A complete description of the detector can be found in the CEBAF SOS Čherenkov Detector Handbook. The SOS Čherenkov detector is a rectangular aluminum box, 99 cm high, 73.7 cm wide, and 111 cm long. The detector was filled with Freon 12 (CCl_2F_2). The index of refraction for Freon 12 is 1.00108, resulting in an electron threshold of 11 MeV and a pion threshold of 3 GeV. The light is reflected onto four Burle 5" 8854 PMTs by four spherical mirrors. In the SOS the electron detection efficiency for a 2 photoelectron cut was ~ 98 %.

2.5.4 Shower Counter (Calorimeter)

A lead glass calorimeter was used for energy measurements and particle identification. When an electron is accelerated near Pb nuclei it emits Bremsstrahlung radiation. This Bremsstrahlung radiation creates electron-positron pairs which creates γ ray photons which produces a cascade of electron-positron pairs. These electrons and positrons generate Čherenkov light which is detected with photomultiplier tubes. The amplitude of the signal from the photomultiplier tube is proportional to the energy of the incident electrons. When a pion or other hadrons are accelerated near a Pb nuclei the interaction is different. They will strongly

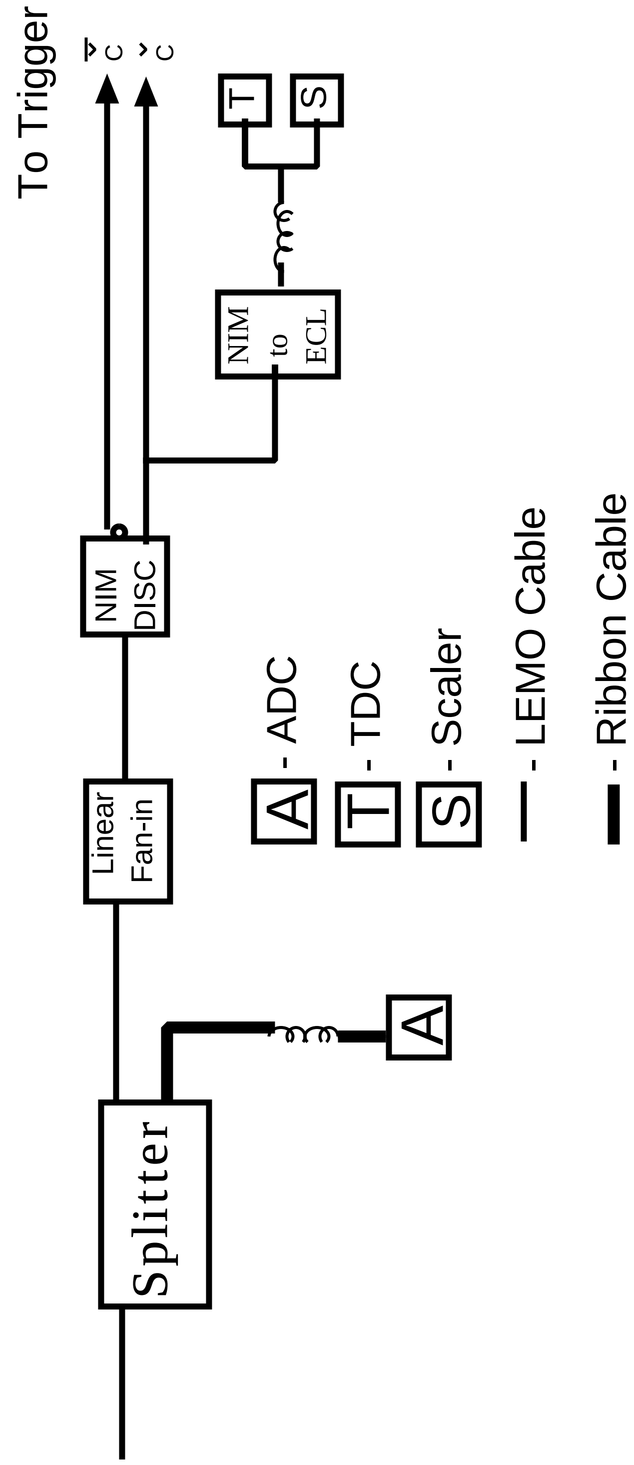

Figure 2.11: Gas Čherenkov counter electronics

interact with the Pb nuclei creating hadronic showers. The hadronic shower process is very complicated and will not be discussed in detail in this dissertation. Hadrons do not deposit as much energy as electrons therefore the signature they leave in the calorimeter is different from the one left for electrons. The differences between electromagnetic and hadronic showers make electron-hadron identification possible [20] [21].

The HMS shower counter is constructed from 10x10x70 cm^3 blocks of TF1 lead glass. The glass is composed of lead oxide and silicon dioxide (51.2% PbO, 41.3% SiO_2, 7% Na_2O). The glass has a density of 3.86 g/cm^3, an index of refraction of 1.67, and a radiation length of 2.5 cm. There are four layers of blocks, each layer is 13 blocks high for a total of 52 Pb blocks and an active area of 130x70 cm^2. The blocks are stacked transverse to the incoming electrons. The shower counter is rotated $\sim 5^\circ$ from the optical axis in order to avoid loss through the cracks between the blocks (see Fig. 2.12). Each block is wrapped with one layer of aluminized mylar and 2 layers of TEDLAR PVF film to increase reflection and make the blocks light tight. A detailed description of the shower counter can be found in ref. [22].

An 8-stage Phillips XP3462B 5–in. photomultiplier tube is connected to one end of the lead block. The signals are taken from the phototubes upstairs to the counting house. Here they are split into two sets - one set is sent to an ADC through delay cables and the other set is sent to LC740 linear fan-in modules

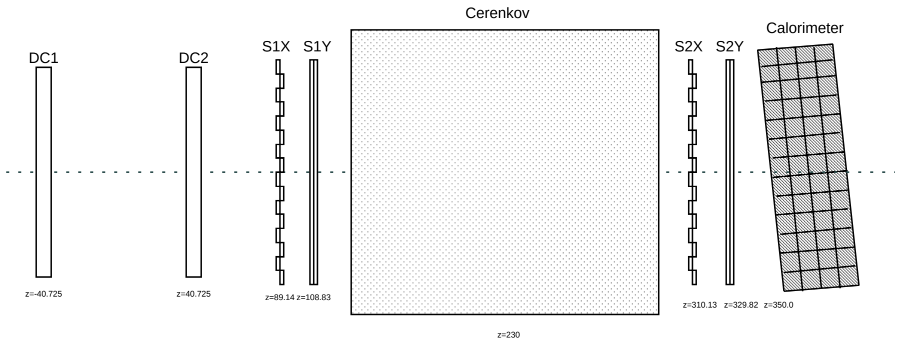

Figure 2.12: Side view of HMS detector hut

where they are summed. The sum of the first layer ($PRSUM$) and the sum of the entire shower counter ($SHSUM$) are discriminated to generate three logic signals ($PRHI$, $PRLO$, and $SHLO$) for the trigger. $PRHI$ and $PRLO$ are the high and low thresholds of the energy in the first layer of the shower counter and $SHLO$ is a threshold set on the total energy in the shower counter.

The SOS shower counter has the same design as the HMS, except the size is different. The SOS shower counter is constructed from 10x10x70 cm^3 blocks of TF1 lead glass. There are four layers of blocks, each layer is 11 blocks high for a total of 44 Pb blocks and an active area of 110x70 cm^2. The blocks are stacked transverse to the incoming particles. The shower counter is rotated $\sim 5°$, just as in the HMS shower counter, from the optical axis in order to avoid loss through the cracks between the blocks. The electronics and the data acquisition system of the SOS shower counter is identical to the HMS shower counter (see Fig. 2.13)

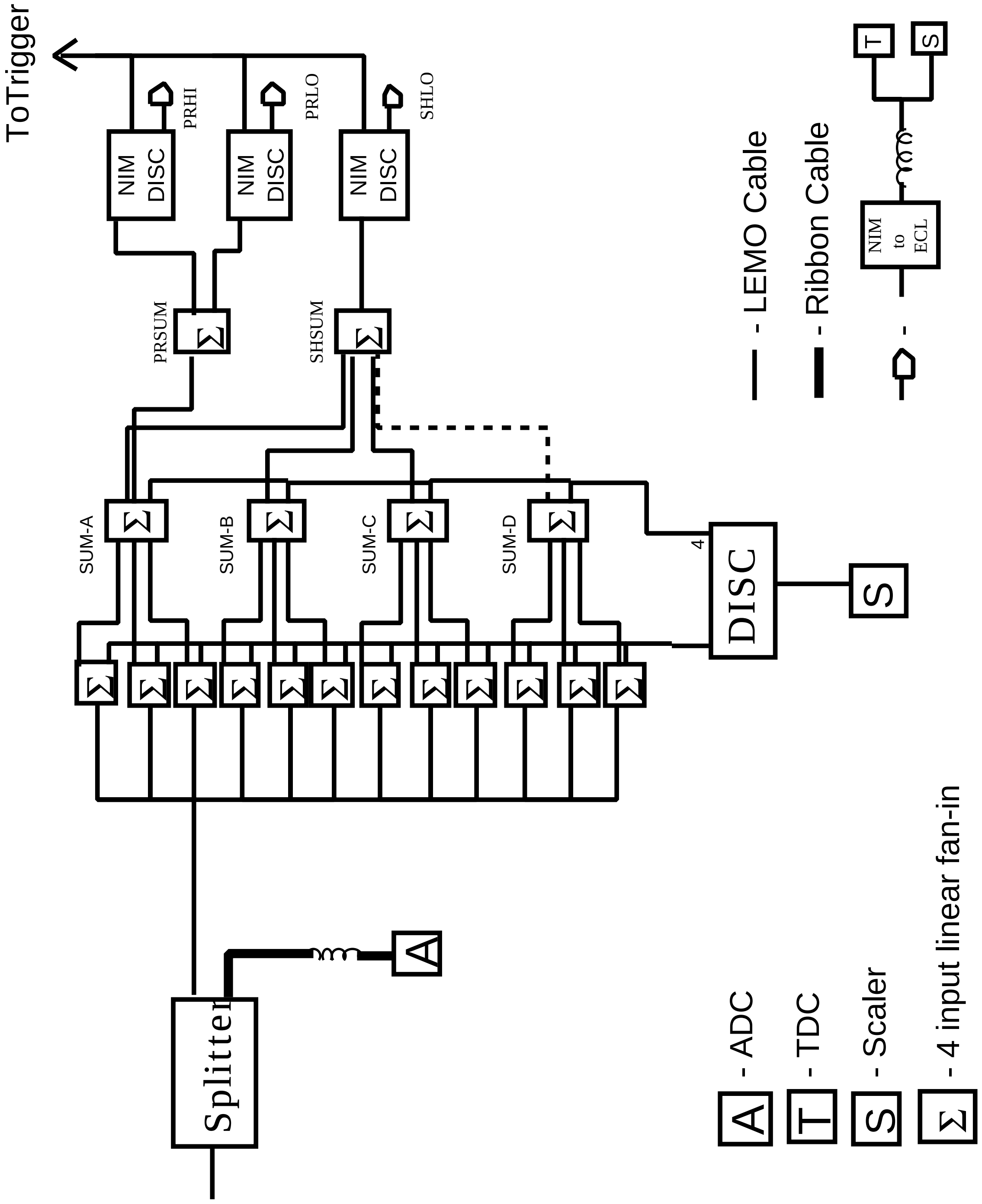

Figure 2.13: HMS/SOS shower counter electronics.

2.6 Trigger Electronics

The trigger is a set of detectors and electronics used to discriminate between certain particles. When a trigger signal is fired it's telling the computer it's o.k. to process that event. As charged particles traverse the spectrometer they form signals from the detectors which are used in different combinations to form triggers. Some events must first make it pass particle identification cuts before it's determined that a trigger is generated. For example, an electron trigger is accepted only if the Čherenkov fired or the shower counter had a signal. This ensures a high electron efficiency. The hodoscopes make up the first part of the trigger, creating two scintillator triggers - $STOF$ and $SCIN$. $STOF$ is the coincidence of one of the front planes and one of the back planes, which is the minimum required for good time-of-flight measurements. $SCIN$ is a much tighter trigger; it has the requirement that 3 out of the 4 scintillator planes give a signal.

The electron trigger ($ELREAL$) has two parts, electron high ($ELHI$) and electron low ($ELLO$). The electron high ($ELHI$) required a calorimeter signal, but no Čherenkov signal. It is made up of a preradiator ($PRHI$) in a three out of three coincidence with the scintillator ($SCIN$) signal and the shower counter signal ($SHLO$). The electron low ($ELLO$) trigger was designed for all electrons. ($ELLO$) needed the two scintillator triggers, $STOF$ and $SCIN$, as well as a shower counter signal ($PRLO$). The pion trigger required the $SCIN$ scintillator trigger vetoed by a Čherenkov signal. Once the trigger was formed additional logic provided the final trigger for the trigger supervisor (TS). The trigger supervisor created all the ADC gates and TDC start and stops signals for the event. Pretriggers were formed if the trigger supervisor was busy. A deadtime constituted the number between the pretrigger events and processed events. The logic for the spectrometer trigger is shown in fig. 2.14

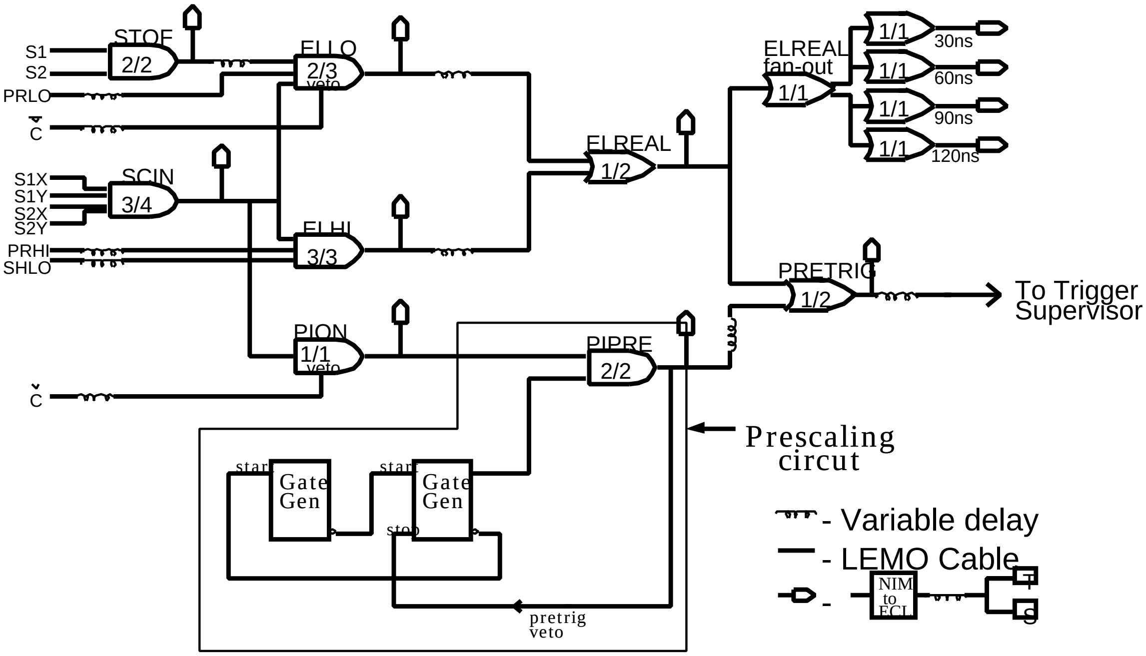

Figure 2.14: HMS/SOS single arm trigger electronics.

2.7 Data Acquisition

The data files for the runs contain the event information ($CODA$) and the slow controls readout ($EPICS$). $CODA$ (Cebaf Online Data Acquisition system) and the GUI (Graphical User Interface) was developed by the Jefferson Lab data acquisition group for this experiment. More information can be found on them in [23] [24] [25].

CODA provides the user interface and manages the data acquisition subsystems. When a run starts, *CODA* determines how to handle triggers from the trigger supervisor. These events are processed by an event builder which reads data fragments from the Fastbus and VME crates which house the ADCs and TDCs. The data from the *ROC*s (*R*ead*O*ut *C*ontrollers) are passed to the event builder which puts together the raw data along with the header information into the event file. The data can also be sent to a subsystem analyzer for online analysis of the data or pre-processing of the events before they are recorded to disk or tape.

Other events can be defined in *CODA* allowing readout of hardware scalers or execution of user scripts. Readout of the hardware HMS and SOS scalers were triggered every two seconds by an asynchronous process. Slow controls were read out by a script triggered by *CODA* every 2 minutes. The quantities for the slow controls variables were read out from the Jefferson Lab *EPICS* database. Values such as spectrometer magnet settings, accelerator settings, and target status variables were accessed this way. Also, separate processes allowed independent target data logging and magnet status logging.

CHAPTER 3

Monte Carlo

In order to account for spectrometer acceptance accurately, an accurate "Monte Carlo" simulation is necessary. This program was also used to compare quasifree pion electroproduction from nuclear targets to a free proton. To extract useful results from the data, radiative corrections, Fermi motion, and cross section modeling were also calculated in the simulation. The Monte Carlo simulation code for Hall C, used for this experiment, is called SIMC. The SIMC originated from a code written by Naomi Makins and T.G. O'Neill to study a color transparency (e,e'p) experiment at SLAC (NE18) [26] [27]. This code adapted existing SLAC radiative corrections and spectrometer models to analyze coincidence experiments. Past experiments have demonstrated that the SIMC has been successful in modeling kaon electroproduction [28] [29], pion electroproduction [30] [31], and quasifree electroproduction on heavy targets [32].

3.1 Event Generation

The simulation begins by creating an electron whose energy and position are determined by parameters given in a database, and then randomly generated within them, hence the term "Monte Carlo". The parameters match the parameters of the actual electron beam. The kinematics given are used to calculate all physics variables, such as momentum transfer, invariant mass, and missing mass. A scattering vertex is constructed by choosing the scattered electron and meson momenta and angle over a range of randomly-generated kinematics that is greater then the experimental acceptance. Events that are outside of the experimental acceptance are not counted as a “good” event. Once the scattering vertex is determined, the probability that the particle emits a real or virtual bremsstrahlung photon is calculated and the trajectories and energies are corrected in accordance with the calculation. The electron and pion are transported through the HMS and SOS spectrometers by using forward matrix elements. After the spectrometers the particle is focused at a point in the detector hut (focal plane). Here, the focal plane quantities are determined as in the data which has to be reconstructed back to the target where the missing energy and momentum are calculated.

Figures 3.1, 3.2, 3.3 illustrate how well the Monte Carlo compares with data at the focal plane. An event is recorded as a success if the electron and pion both make it to their respective focal planes. Each successful event is assigned a weight of

$$weight = SF * J * RAD * \sigma, \tag{3.1}$$

where

- SF is the model spectral function;

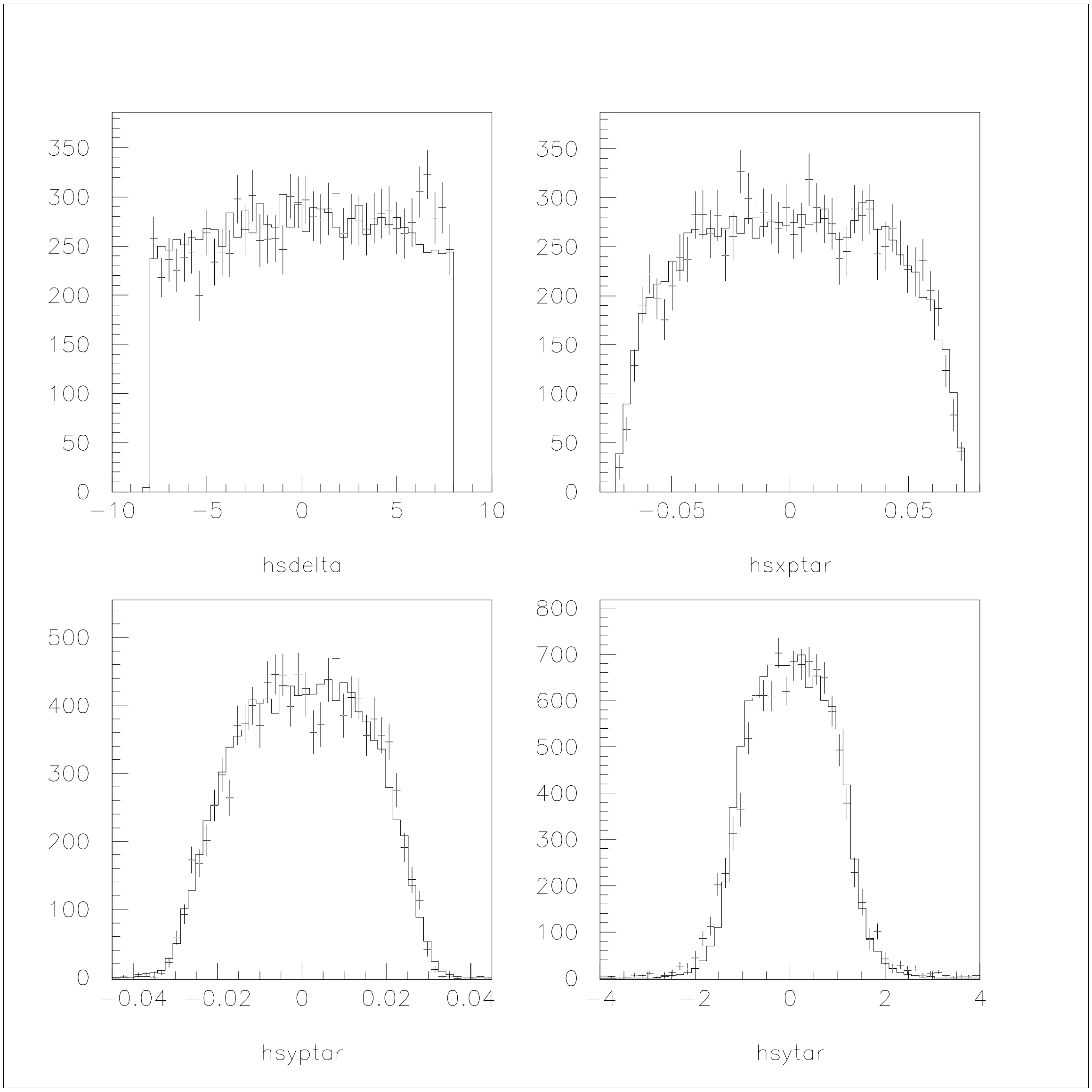

Figure 3.1: SIMC comparison for reconstructed HMS quantities. Cross bars are the data and the solid line is the Monte Carlo. The SIMC has been normalized to match to data yield.

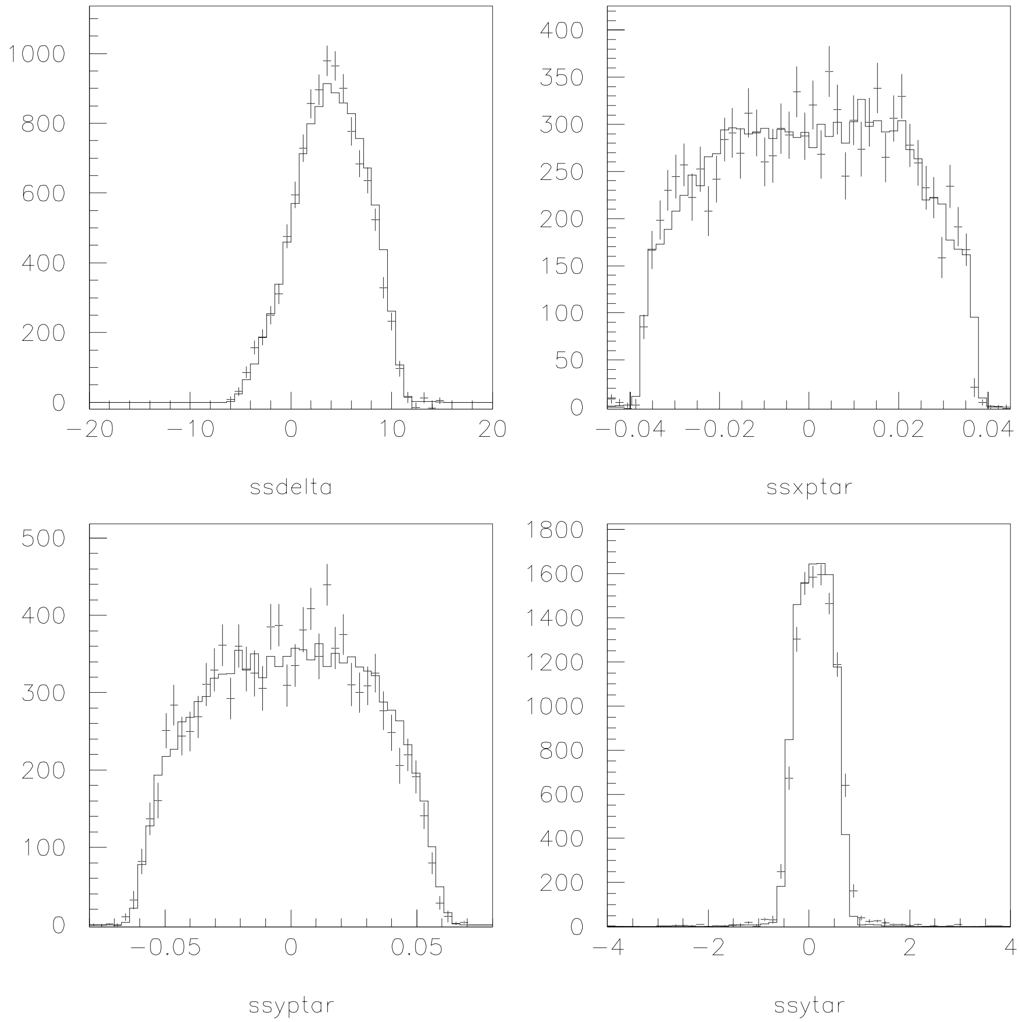

Figure 3.2: SIMC comparison for reconstructed SOS quantities. Cross bars are the data and the solid line is the Monte Carlo. The SIMC has been normalized to match to data yield.

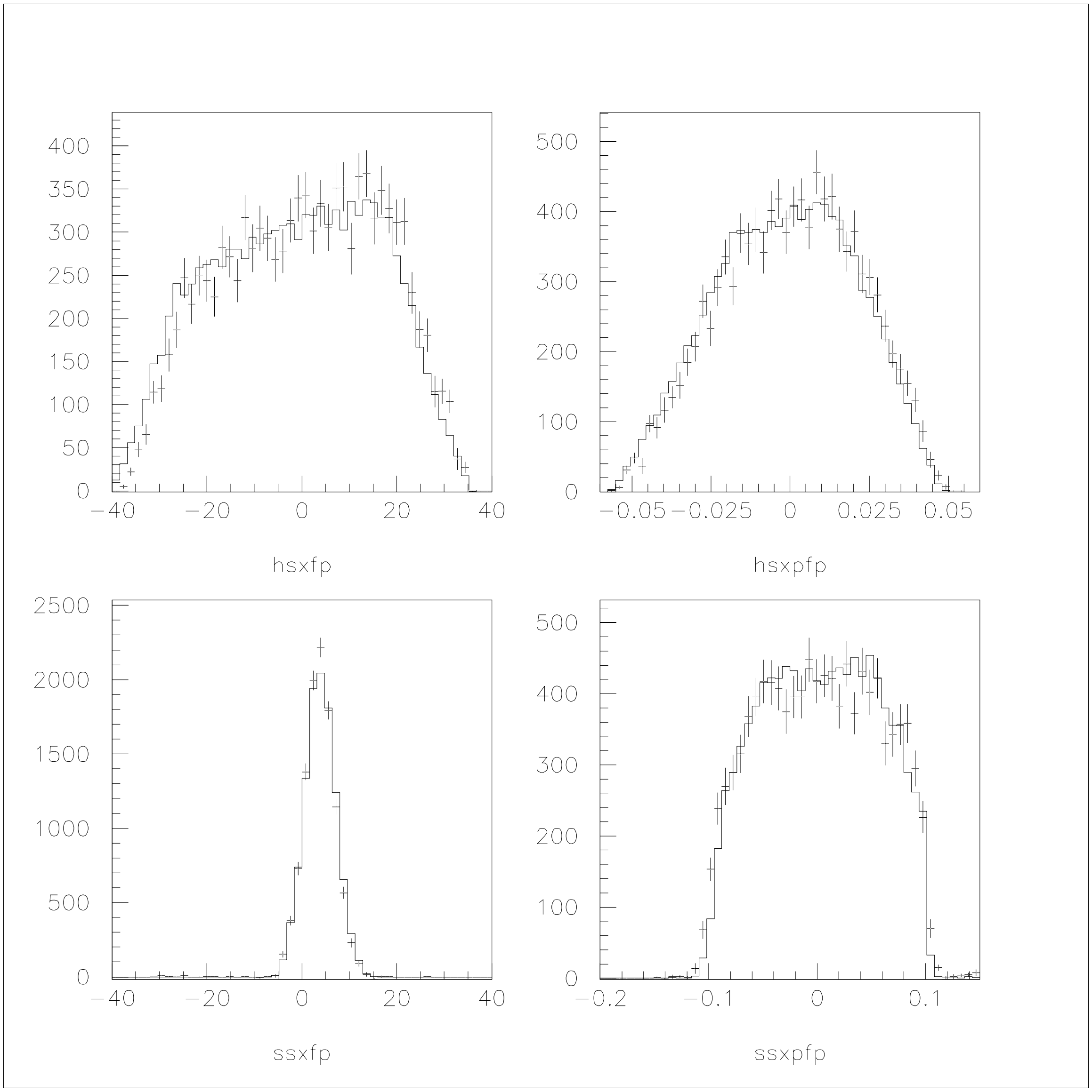

Figure 3.3: SIMC comparison for HMS and SOS focal plane quantities. Cross bars are the data and the solid line is the Monte Carlo. The SIMC has been normalized to match to data yield.

- J is the Jacobian which takes it from the center-of-mass frame to the laboratory frame;
- RAD is the radiative correction calculated on an event-by-event basis; and
- σ is the model cross section.

Any event that is outside of the experimental acceptance is given a weight equal to zero. Finally, all the events are weighted by

$$\frac{L * ACC}{N_{gen}}, \tag{3.2}$$

where L is the luminosity, ACC is the phase space volume, and N_{gen} are the number attempts.

The SIMC calculates a five-fold cross section (polar angles from electron and pion and electron final energy) for hydrogen, but for the nuclear targets an extra degree of freedom is introduced, due to the Fermi motion inside the nucleus, creating a six-fold cross section. For the nuclear targets we assume scattering off a single nucleon (quasifree scattering). In order to do quasifree scattering we must know the momentum distribution of the struck nucleon. In deuterium we used the Bonn potential calculation [28], and in helium-3 the Fadeev calculation was used [31].

3.2 Transport through the HMS and SOS

The path the electrons and pions take through the spectrometer and into the detector huts is determined by matrix elements that particles through the spectrometers to the detector hut. The matrix elements originate from the COSY INFINITY [33] transport program based on measured field maps or design specifications. The spectrometer is divided up into sections and different matrices are applied to their respective section. The particles are not passed to the matrix elements until the angles and energy have been calculated at the target. After each section multiple scattering and energy loss are calculated for the materials that the particles travel through. Tables 3.1 and 3.2 list all the materials that the particles traverse in the HMS and SOS.

SIMC uses a parameterization of a Moliere scattering calculation [34] to simulate the effect of multiple scattering. Multiple scattering can happen anywhere in the spectrometer, in the target, in air, or in any of the detector elements. In order to have a good comparison with data a reliable calculation is necessary in all places. Multiple scattering is not only applied to the scattered electron and pion, which are detected in the HMS and SOS respectively, but also to the initial electron. The energy loss, like multiple scattering, can occur anywhere throughout the experimental apparatus. SIMC calculates a Landau distributed energy loss for all materials.

Material	t(cm)	rho(g/cm^3)	$X_0(g/cm^2)$	r.l.(%)
Target				
Entrance cap	0.0071	2.7	24.01	0.080
LH2	4.36	0.0723	61.28	0.514
LD2	4.17	0.1670	122.6	0.568
LHe3	4.00	0.7690	64.77	0.474
Exit cap	0.0137	2.70	24.01	0.155
Chamber exit	0.0406	2.70	24.01	0.457
Spectrometer				
Air	$\approx$ 15	0.0021	36.66	$\approx$ 0.050
Kevlar entrance	0.0381	0.74	55.2	0.051
Mylar entrance	0.0127	1.39	39.95	0.044
Kevlar exit	0.0381	0.74	55.2	0.051
Mylar exit	0.0127	1.39	39.95	0.044
Detector Hut				
Air	$\approx$ 35	0.00121	36.66	$\approx$ 0.116
DC Mylar	0.0102	1.39	39.95	0.036
Ar/CH_4 gas	21.6	0.00154	$\approx$ 25.7	$\approx$ 0.129
Sense Wires(W)	0.00006	19.3	6.76	0.017
Field Wires(W)	0.00212	$\approx$ 3.5	$\approx$ 25	$\approx$ 0.030
Air	$\approx$ 210	0.00121	36.66	$\approx$ 0.693
S1X	1.067	1.03	43.8	2.510
S1Y	1.067	1.03	43.8	2.510
CER entr.	0.1	2.70	24.01	1.125
CER gas(Freon)	$\approx$ 150	0.0025	$\approx$ 23.7	$\approx$ 1.582
CER mirror	-	-	-	$\approx$ 0.5
CER exit	0.1	2.70	24.01	1.125
S2X	1.067	1.03	43.8	2.510
S2Y	1.067	1.03	43.8	2.510
Air	$\approx$ 18	0.00121	36.66	$\approx$ 0.600
Calorimeter	40	-	-	$\approx$ 1600

Table 3.1: HMS materials used to calculate multiple scattering in the Monte Carlo simulation.

Material	t(cm)	rho(g/cm^3)	$X_0 (g/cm^2)$	r.l.(%)
Target				
Entrance cap	0.0071	2.7	24.01	0.080
LH2	4.36	0.0723	61.28	0.514
LD2	4.17	0.1670	122.6	0.568
LHe3	4.00	0.7690	64.77	0.474
Exit cap	0.0137	2.70	24.01	0.155
Chamber exit	0.0203	2.70	24.01	0.288
Spectrometer				
Air	≈ 15	0.00121	36.66	≈ 0.050
Kevlar entrance	0.0127	0.74	55.2	0.017
Mylar entrance	0.0076	1.39	39.95	0.027
Kevlar exit	0.0381	0.74	55.2	0.051
Mylar exit	0.0127	1.39	39.95	0.044
Detector Hut				
Air	≈ 15	0.0021	36.66	≈ 0.050
DC Mylar	0.0178	1.39	39.95	0.062
Ar/CH_4 gas	7.41	0.00154	≈ 25.7	≈ 0.044
Sense Wires(W)	0.00008	19.3	6.76	0.022
Field Wires(W)	0.00034	19.3	6.76	0.098
Air	≈ 49.5	0.0021	36.66	≈ 0.1633
S1Y	1.098	1.03	43.8	2.582
S1X	1.04	1.03	43.8	2.446
CER entr.	0.05	2.70	24.01	0.056
CER gas(Freon)	≈ 100	0.0051	≈ 23.7	≈ 2.152
CER mirror	-	-	-	0.5
CER exit	0.05	2.70	24.01	0.056
S2Y	1.098	1.03	43.8	2.582
Aerogel entr.	0.0625	2.70	24.01	0.70
Aerogel	9.0	-	-	≈ 6
Aergel exit	0.0625	2.70	24.01	0.70
S2X	1.04	1.03	43.8	2.446
Air	≈ 20	0.00121	36.66	≈ 0.066
Calorimeter	40	-	-	≈ 1600

Table 3.2: SOS materials used to calculate multiple scattering in the Monte Carlo simulation.

3.3 Pion Decay

Pion decay is a major concern for E91003. As discussed in section 3.1, the Monte Carlo divides the spectrometer into sections. After each section it checks to see if the particle decays.

Decay Modes	Branching Ratio (%)	p (MeV/c)
$\mu^+\nu_\mu$	99.99 ± 0.00004	30
$\mu^+\nu_\mu\gamma$	(1.240 ± 0.25)x10^-4	30
$e^+\nu_e$	(1.230 ± 0.004)x10^-4	70
$e^+\nu_e\gamma$	(1.610 ± 0.23)x10^-7	70
$e^+\nu_e\pi^\circ$	(1.205 ± 0.034)x10^-8	4

Table 3.3: Table of π^+ decay channels. π^- modes are the charge conjugates of the modes shown above.

There are many decay channels of the pion, with the primary one being a pion decaying into a muon and muon neutrinos. Table 3.3 list the primary decay channel with a few channels with a branching ratio $< 1\%$. Any decay modes not shown can be found in any particle data book. The pion decay probability is equal to,

$$P(x) = 1 - e^{-x/(\beta\gamma c\tau)}, \tag{3.3}$$

- $P(x)$ is the probability for a pion not to decay after traveling a distance x,
- x is the distance the pion traveled,
- $\beta\gamma$ is the boost given to the pion to measure the decay in the lab frame,
- $c\tau$(=7.8045 m) is the decay length of the pion.

The SIMC was needed to correct for pions that decayed into muons that went out of the acceptance and pions that decay into muons and give a trigger as if it were a pion. In the data analysis, it's not easy to separate the muons from the pions because they are so close in mass($\mu_{mass} = 0.105$ GeV; $\pi_{mass} = 0.139$ GeV).

After each section the Monte Carlo determines the decay probability of the pion traveling a distance x. From this calculation the decay distance is determined. If the decay distance is less then the length for the section the pion is forced to decay. For our low momentum setting, muons are faster then the pions by 1ns. Therefore, we are able to see them in the data and can estimate the the contribution on muon contamination and compare it to the Monte Carlo to see how well it modeled the pion decay. For our high momentum setting the pion and muon arrive at the same time leaving us totally dependent on the Monte Carlo.

3.4 Radiative Corrections

In electron scattering, the incoming and/or outgoing electron and/or hadron can emit a real or virtual photon. The degree to which this occurs can significantly change the cross section. We used SIMC to deal with these radiative corrections. Radiative corrections to electron scattering have been studied extensively [35]. The formalism we used is based on the work of Mo and Tsai [36] [37], to correct for effects from higher order Feynman diagrams. Originally the code was used for single arm experiments, but it has been modified to be used for coincidence experiments. Refs. [26] [27] [31] will give more explanation into how the modifications were done. The first use of these changes were done for (e,e‘p) reactions. For pion electroproduction, the same was calculated for radiative correction but instead of a p (proton) we have a pion. Since the contribution to the radiative corrections that are directly related to the outgoing pion should be small, the approximation should be satisfactory. SIMC calculates the probability in each arm that it will radiate. Once the probability is computed a radiated photon is assigned to one of the arms (incoming/outgoing electron, outgoing pion). If the outgoing electron is outside of the delta acceptance without radiating, the radiated photon will be assigned to that arm, and the events weighted by the relative probability that the outgoing electron would have radiated. The spectrometer delta acceptance for the outgoing electron is made large to include all events that might radiate into the acceptance, but a range in the final electron momentum, such that an event would fall into the acceptance, is not determined. This procedure would make the calculation of the overall weight very difficult.

There are two main contributions to the radiative correction calculation, external Bremsstrahlung and internal (soft and hard). The external Bremsstrahlung correction (see Fig. 3.4) are needed because the incoming/outgoing electron or outgoing pion emit real photons due to the interactions with its surroundings, outside the field of the target nuclei. This correction is easier to deal with then the internal contributions, because the target is far enough away that the amplitudes add in-

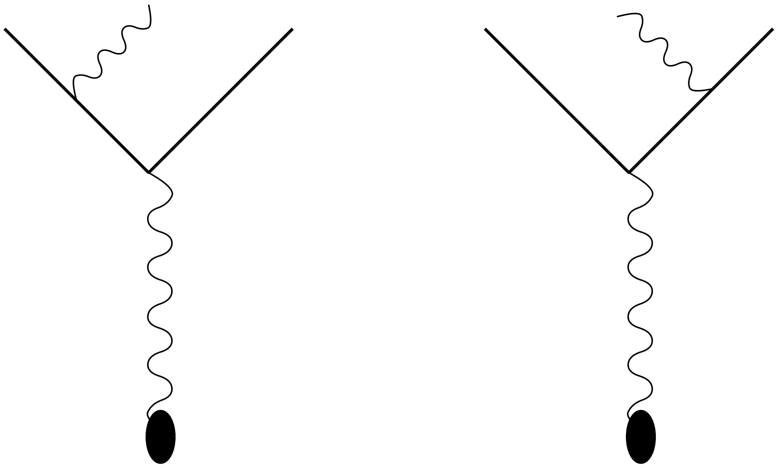

Figure 3.4: External Bremsstrahlung diagram.

coherently and interference effects do not pose a problem. Internal contributions, on the other hand, are more difficult to deal with. The internal (soft) corrections (see fig. 3.5) has an incoming/outgoing electron or pion radiate in the field of the target nuclei, resulting in interference terms due to the amplitudes having to be added coherently. This is the main difference between the internal and external soft radiative corrections. The internal (hard) corrections are calculated by QED. They contain the vacuum polarization or self-energy diagrams (see fig. 3.6). These processes do not include the emission of real photons and the modification of vertex kinematics. Since the finals states for the internal hard processes are indistinguishable from the Born term they create a background underneath the cross section that needs to be measured.

Basically, the SIMC radiative correction calculation is based on two approximations. First, the *extended peaking approximation* assumes the Bremsstrahlung radiation of one photon is in the same direction as the radiating particle. The

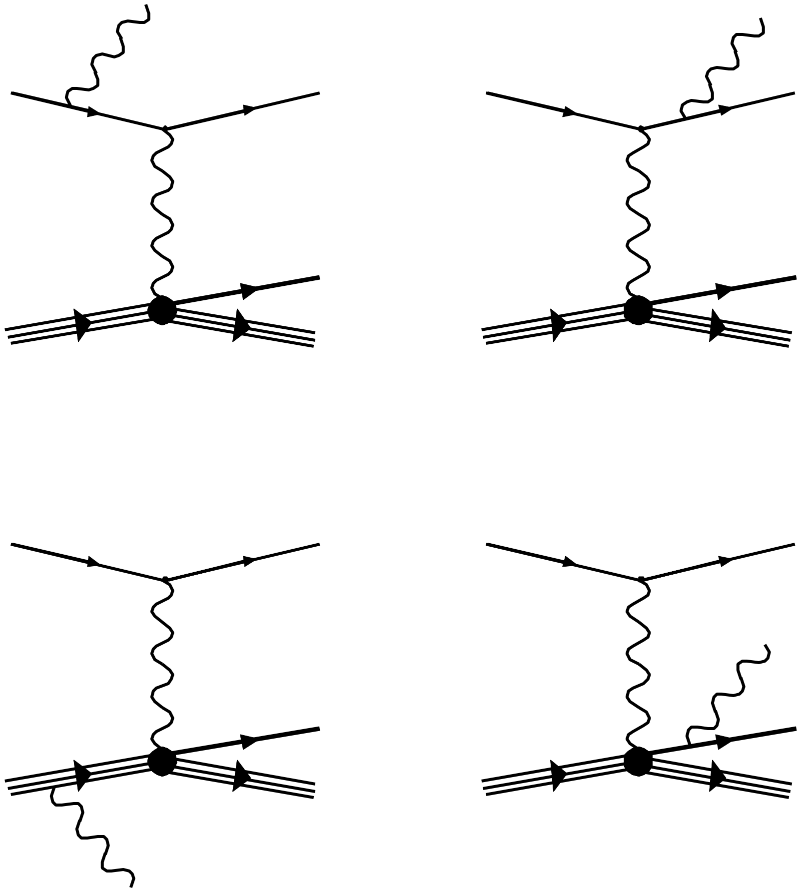

Figure 3.5: Feynman diagrams for the internal (soft) radiative corrections which contribute to the cross section.

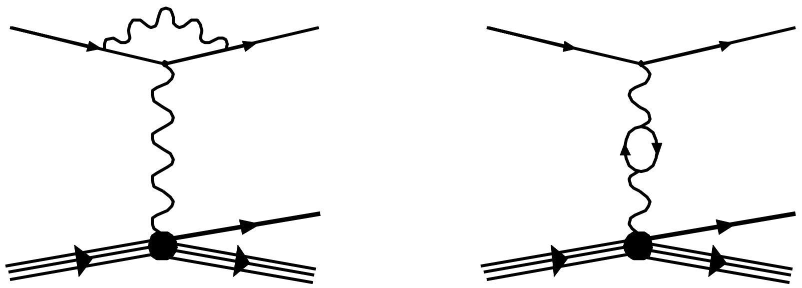

Figure 3.6: Feynman diagrams for the internal (hard) radiative corrections which contribute to the cross section.

energy of this photon is calculated based on a ω^{r-1} distribution function, where ω is the photon energy and r is determined by the formulas used for radiative corrections. Second, the *soft photon approximation* requires the energy of the radiated photon be small compared to the energies of the incident and scattered particles. Finally, all radiative correction weights are combined with the physics cross section weight.

3.5 Physics Models

SIMC weights each event with a cross section model that is calculated at the vertex. The SIMC writes the pion electroproduction cross section as

$$\frac{d^5\sigma}{dE_{e\prime}d\Omega_{e\prime}d\Omega_\pi} = \Gamma J \frac{d\sigma}{d\Omega_\pi{}^*} \tag{3.4}$$

where the virtual photon flux Γ, is

$$\Gamma = \frac{\alpha}{2\pi^2}\frac{E'K_{eq}}{EQ^2(1-\epsilon)} \tag{3.5}$$

and $\frac{d\sigma}{d\Omega_\pi{}^*}$ is the center of mass virtual photon cross section. The energy required for a real photon to excite a nucleon to a mass W is called the equivalent photon energy, K_{eq}. K_{eq} is defined as

$$K_{eq} = \frac{W^2 - m_n}{2m_n} \tag{3.6}$$

where m_n is the mass of the nucleon. The center of mass cross section is written in terms of transverse, longitudinal, and the interference terms(transverse-longitudinal,transverse-transverse),

$$\frac{d\sigma}{d\Omega^*}_{\pi} = \frac{d\sigma_T}{d\Omega^*} + \varepsilon_L \frac{d\sigma_L}{d\Omega^*} + \sqrt{2\varepsilon_L(\varepsilon+1)} \frac{d\sigma_{LT}}{d\Omega^*} \cos\phi + \varepsilon \frac{d\sigma_{TT}}{d\Omega^*} \cos 2\phi \tag{3.7}$$

where

$$\varepsilon = \frac{1}{1 + 2\frac{|\vec{q}|^2}{Q^2} \tan^2 \frac{\theta_{e'}}{2}} \tag{3.8}$$

$$\varepsilon_L = \frac{Q^2}{\omega^2} \varepsilon \tag{3.9}$$

3.5.1 Proton Target

We used two different models to calculate the cross section. They were the MAID and and Multipole models. Both models calculated the cross section differently. The Maid model was done at the University of Mainz [**?**]. The Maid model calculates resonant and non-resonant multipoles constrained by existing data. It takes W, Q^2, and $\cos\theta^*{}_\pi$ as inputs to the model to calculate the multipoles using an analytical parameterization. The Multipole model [39] [40] [41] just uses a look-up table of multipoles that are binned in K_{eq} and Q^2. Both the Maid and the Multipole end up with response functions that are multiplied by a kinematic factor to get the center-of-mass cross section. The kinematic factors are the same for both models. The individual terms are:

$$\frac{d\sigma_T}{d\Omega_\pi^*} = \frac{p_\pi W}{2K_{eq}m_n} R_T \tag{3.10}$$

$$\frac{d\sigma_L}{d\Omega_\pi^*} = \frac{p_\pi W}{K_{eq}m_n} R_L \tag{3.11}$$

$$\frac{d\sigma_{TL}}{d\Omega_\pi^*} = 2\frac{p_\pi W}{K_{eq}m_n} REAL(R_{TL}) \tag{3.12}$$

$$\frac{d\sigma_{TT}}{d\Omega_\pi^*} = \frac{p_\pi W}{2K_{eq}m_n} R_{TT}. \tag{3.13}$$

For scattering off the proton, one needs to calculate Γ_ν in the lab frame and boost the pion to the center-of-mass frame to calculate $\frac{d\sigma}{d\Omega_\pi{}^*}$. Finally, you have to transform the virtual cross section back to the lab by using a Jacobian (J), $J = d\cos\theta^*/d\cos\theta$.

3.5.2 Nuclear Targets

For the nuclear targets, SIMC assumes scattering off a single proton(neutron) with the other nucleons as spectators. The difference here is that the target nucleon is now allowed to move. Since the target is allowed to move we must account for the relative velocity of the target particle by correcting the incident flux by a factor of $[1 - \vec{p}_{fermi} \cdot \vec{p}_e/(E_{target} \cdot p_e)]$. K_{eq} stays the same for a moving target as it was used for a stationary target, because it gives the correct W dependence. Although W is calculated differently:

$$W^2 = (E_{target} + \omega)^2 - (\vec{p}_{fermi} + \vec{q})^2 \tag{3.14}$$

The main problem is how to deal with the target nucleon being off-shell. When an event is generated the target is off-shell while the spectator is on-shell, the models we use assume the target is on-shell. To get around this problem we choose a target nucleon energy so that the particle is on-shell. Next, both models require that their amplitudes be multiplied by some kinematic factor. For the Multipole model, once a method on how to to calculate the off-shell K_{eq} has been determined there are no doubts. For the MAID model the problem occurs from the fact that we calculated W and $\cos\theta^*$ under the assumption that we are using an off-shell method. When MAID determines ω^* from the input quantities, it assumes the target nucleon is on shell so that the virtual photon energy, momentum, and the amplitudes it returns may not be consistent with the kinematics that we generated for the event. This is not a problem if we change the event generation scheme and put the target nucleon on shell and the spectator off-shell.

CHAPTER 4

Data Analysis

The offline data analysis of the raw data was done using the dedicated Hall C replay $ENGINE$ [43]. This Fortran based code is designed for use in single-arm or coincidence experiments. Basically, $ENGINE$ reads each raw event, determines which detectors were fired, reconstructs trajectories, and generates particle identification information for each event. The software interfaces with two different packages:

- CODA (*C*ebaf *O*nline *D*ata *A*cquisition) [44] for event readout and decoding,
- CERN libraries [53] for access to fitting, plotting and data presentation such as PAW, HBOOK, etc.

After processing the data through the replay $ENGINE$, the output is stored in three different forms: 1) ASCII files which contain information on detector efficiencies as well as hardware and software scalers, 2) A standard set of histograms files, in HBOOK format, to check the performances of detectors[1], and 3) N-tuple files which contain event-by-event information. The calibration of the detector packages for both spectrometers are done with separate softwares.

---

[1] The code is also run online to monitor the experiment during data acquisition.

4.1 Hall C Replay ENGINE

The Hall C replay *ENGINE* takes the raw data sets from the ADCs, TDCs, and scalar values from the HMS and SOS detector packages as input to the program. Fig. 4.1 shows a flowchart of the Hall C replay *ENGINE*. It takes this information and finds the particles which fit the criteria of the analysis while rejecting the ones that lay outside. Once the particle has been determined to be a good one, the *ENGINE* reconstructs the track of that particle. This is done on an event-by-event basis. Raw signals from detector elements, beamline elements, and integrated charge are stored in scalar files from which an overall efficiency is calculated.

4.1.1 Initialization

When the *ENGINE* starts it reads a configuration file (replay.parm), which contains all the specifications of the output needed to properly analyze the data. It includes: (*i*) name and location of the raw data, files containing the histograms and tests definitions, parameter files, and kinematics file; (*ii*) information on how ADC/TDC channels are connected to the various detectors; (*iii*) which flags should be on/off; (*iv*) how the output scaler reports should be produced, and; (*v*) how N-tuples and histograms should be produced.

After all the parameters have been initialized, the raw data file is opened and information on the corresponding run is read, i.e. beam energy, target, HMS and

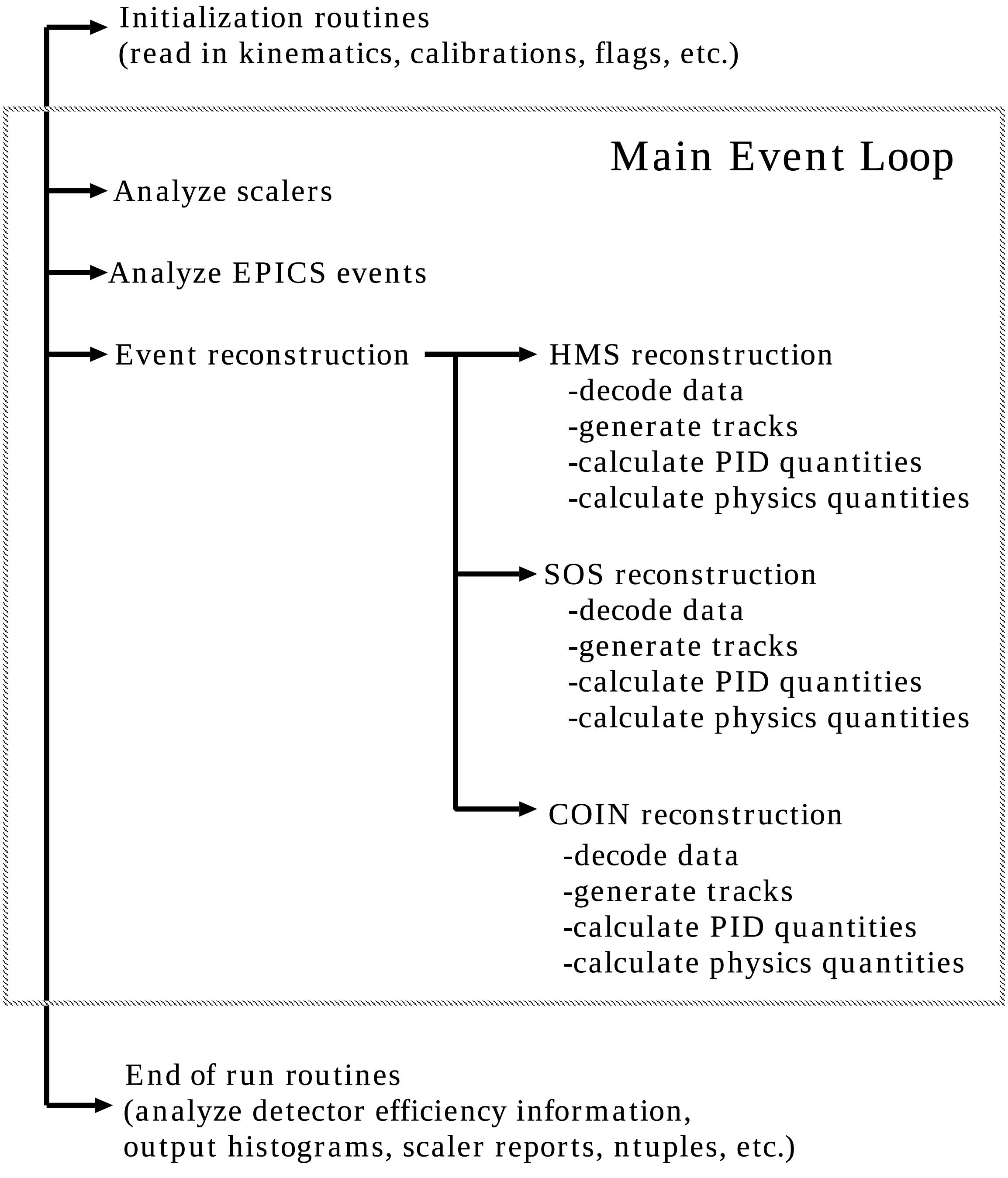

Figure 4.1: Hall C replay *ENGINE* flowchart.

SOS angles, central momenta, etc. Once the initialization procedure is complete the main loop begins. The main loop processes each event type in a series of steps.

4.1.2 Main Event Loop

The main event loop reads and processes each event based on the event type which can be either scaler, EPICS, or physics. Scaler events correspond to the total number of counts recored for a specific element. EPICS events are readouts from the HMS and SOS hardware scalers, target variables and accelerator settings. The physics events can either be HMS, SOS, or COIN generated by spectrometer triggers. Each physics event is reconstructed and information is recorded for each spectrometer. Physics quantities are calculated and recorded for coincident and single events.

When the scaler events are analyzed, all corresponding hardware scalers are then incremented, including the time and charge since the last event. The total charge and running time are also computed.

The EPICS events monitor the status of the cryotarget, settings for the magnetic spectrometer, monitor beam position, etc. The output from those events are stored in ASCII files where they can be analyzed separately.

The physics events can be classified into four groups: pedestal, HMS, SOS, and COIN events. At the beginning of each run, 1000 random trigger events are generated and are used to obtain a measurement of the ADC/TDC pedestals. The

HMS, SOS, and COIN events are generated by real spectrometer triggers. The detector hits for each event are read in and passed to the main reconstruction routine for the HMS and SOS. After reconstruction, particle identification information is computed and saved for each spectrometer. Finally, the physics quantities are calculated for single triggers and coincidence events in each spectrometer.

4.1.3 Event Reconstruction

The reconstruction codes for the HMS and SOS are nearly the same. The only differences are the variable names, which distinguish between the two spectrometers. The code starts out with the hodoscope hits for each event. They are then converted from raw ADC/TDC values to pulse heights and times. Timing corrections, due to pulse height variations, jitter (timing walk), temperature and cable length offsets, were applied and events outside the timing window are eliminated to reduce random hits. The other signals are used to compute the velocity of the particle and the time when the particle passes through the drift chambers, the drift time calculation uses this information as a start time. After the hodoscopes have been analyzed and the start time determined, the data from the other detectors (Čherenkov, shower counter) are analyzed and the track independent quantities are calculated via a dedicated tracking routine.

In the tracking routine, the basic idea is to use the information from the drift chambers to reconstruct the path for charged particles through the detector stack. When a wire from a drift chamber is fired, the position of the wire and the drift time of the electron-ion pairs created from that particle inside the gas mixture of the drift chamber are extracted. However, the question of did the particle pass to the left or the right of the wire needs to be answered. The analysis of the chamber gives $\approx 2^6$ possibilities that need to be tested. To reconstruct the track, the trajectory of the particle is tested for all possible combinations and the track with the lowest χ^2 is chosen as the trajectory.

The particle velocity is calculated, using the hodoscope time-of-flight information for all hits along the track. To find a good time-of-flight measurement, at least one hit was required on the front and back planes of the hodoscope. The energy from each track in the shower counter is determined by summing all bunches of hits found in the lead glass blocks. In the end, each track is reconstructed back to the target in addition to the momentum, position and angles of the particle.

To determine the final best track, last cuts are applied on the particle velocity and the shower counter. The track chosen is the one that makes it through these cuts and has the best fitted χ^2. Finally, all the physics quantities are calculated, and the coincidence tests and histograms are filled. A more detailed discussion can be found in [30].

4.1.4 Output

When the run comes to an end, the replay *ENGINE* writes the output scaler, histogram, and N-tuple files. The scaler files consists of the beam current, detector efficiencies, hardware/software scalers, and dead time correction factors. The histogram files contain information on detector performances which can be used to check various calibrations. Event-by-event information consisting of tracking, particle identification, and the reconstructed quantities are stored in row wise N-tuple files, which give the ability to make cuts on reconstructed and particle identification quantities by keeping the correlation between variables.[2]

4.2 Reconstruction of Target Quantities

After the final track is determined, and having an understanding of the optical properties of the spectrometers one can calculate the position of the particle at the focal plane, and the momentum and direction of the particle at the target. The original particle propagation program, *TRANSPORT* [45], involves a Taylor expansion of the equations of motion for a charged particle in magnetic fields to second order around the central path trajectory. Currently, the transport program in use is called *COSY INFINITY* [46]. A matrix describes the transformation between the focal plane variables $(x_{fp}, x'_{fp}, y_{fp}, y'_{fp})$, and the target variables $(\delta(p), x'_{tar}, y'_{tar}, y_{tar})$. Restrictions on the matrix elements include requir-

---

[2] This correlation is lost when using a standard 2D histogram.

ing a point-to-point focus to make the position at the focal plane independent of the angle and making the necessary matrix elements to be zero to allow for midplane symmetry. In order to find a set of matrix elements that describes the particles trajectory through the spectrometer, a reliable description of the drift distances and magnetic components is needed. The HMS uses models of the dipole and quadrupoles, while the SOS were field mapped and inputted in $COSY$.

4.3 Time-of-Flight

The particle velocity was determined by using timing information from planes of hodoscopes in conjunction with known distances between them. This information was vital because it allowed one to separate pions from protons in the SOS. Each time an event occurred the pulse height variation, the fluctuation times taken by the scintillation light to travel from the π, p point of interaction in the scintillator to the photomultiplier tubes (PMT), and offsets from cable lengths and electronic delays were corrected, in order to measure the "time-of-flight" of the particles.

In the experiment described in this thesis, the particle velocities were calibrated using the Hall C time-of-flight (TOF) fitting code [47] which used timing and scintillator information from $ENGINE$. The code corrects the pulse height variation by parameterizing the shape of the pulse and fitting the timing information. To correct for the time it took light to travel to the PMT in a given scintillator paddle, the time difference between signals from both ends of the scintillator hodoscopes were fitted.

To select out clean samples of pions in our experiment, the relative velocity from each event using the momentum and energy was calculated,

$$\beta_{tof} = \frac{|\vec{p}|}{E} = \frac{|\vec{p}|}{\sqrt{|\vec{p}|^2 + m^2}} = \frac{v}{c} = \frac{d}{ct}. \tag{4.1}$$

Since the distance (d) between hodoscope planes is known and the time (t) it takes a particle to travel from one plane to the next is measured, one can calculate by $time = distance/(\beta_{tof}c)$[3] the velocity of the particle relative to the speed of light. The Hall C Time-of-Flight fitting code adjusts for offsets and gives the correct value of the time for each event. Once the calibrations are completed, the relative velocity (β_{tof}) is calculated for each event during the replay of a run. A typical raw spectrum is shown in Figure 4.2. The differing mass of pions and protons yields, for the same fixed spectrometer momentum, substantially different velocities. Therefore, they are distinguished by their β_{TOF}, as in the figure.

During data analysis we found that a PMT was not functioning properly in one of the *SOS* hodoscope bars. This PMT was consequently removed from the *ENGINE* software. This did not cause a problem for the TOF calculation because it only needed the signal from one side of the paddle to get the time of

---

[3] In eqn. 4.1, one needs a mass input which was taken to be m = m_π. Consequently, if one plots β vs. cointime, only π angle will be straight since timing for the other particles is off (i.e. slanted).

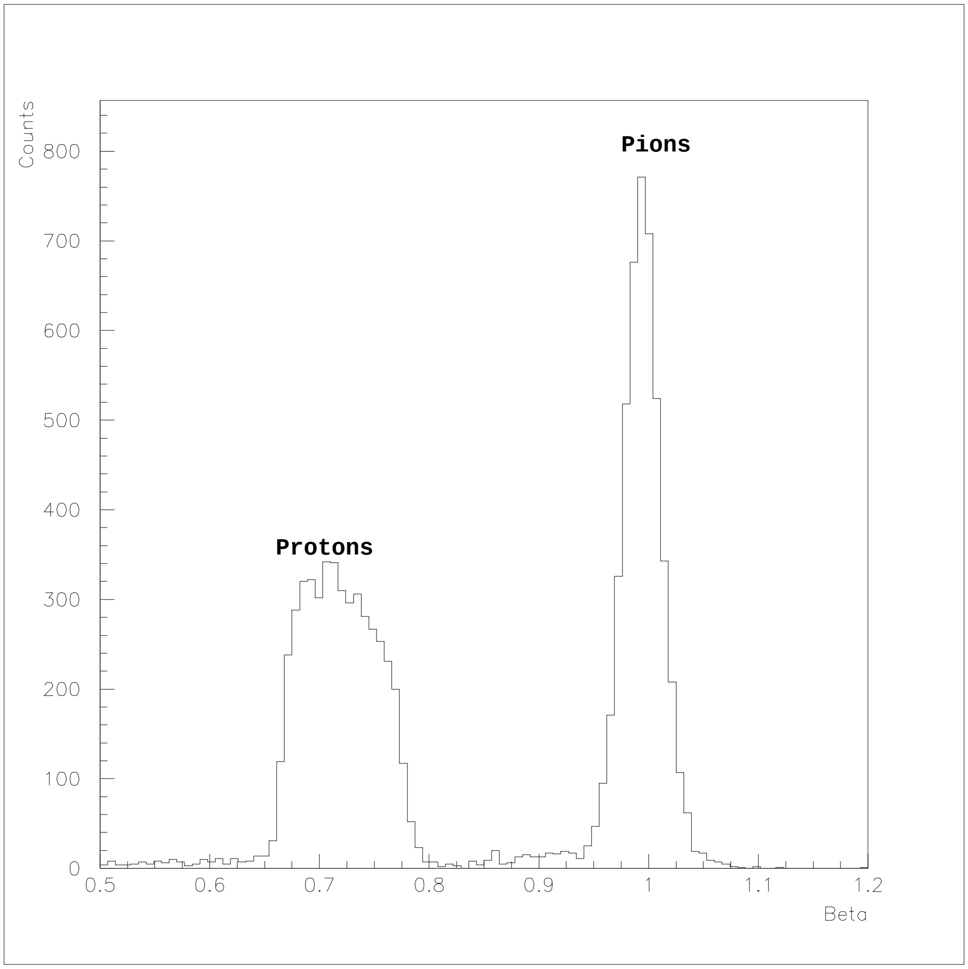

Figure 4.2: Typical raw β_{tof} for the SOS.

flight information.

4.4 Identification of Good Events

The goal of **E91003** was to select out a clean sample of pions to search for a signature of pion enhancement. From the target many particles are produced and accepted into the detector huts as a valid event. During the analysis of the

Cuts used for data and Monte Carlo ($SIMC$)		
$\lvert hsdelta \rvert$	$<$	8.0 (%)
$\lvert hsxptar * 166.37 \rvert$	$<$	12.2 (rad)
$\lvert hsyptar + 166.37 * hsyptar \rvert$	$<$	4.9 (rad)
$\lvert ssdelta \rvert$	$<$	15.0 (%)
$\lvert ssxptar * 126.3 \rvert$	$<$	7.0 (rad)
$\lvert ssyptar + 126.3 * ssyptar \rvert$	$<$	7.7 (rad)
Particle ID cuts for data only.		
$\lvert cointime - 1.2463 \rvert$	$<$	3.0 (ns) ; coincidence time cut for real events
$\lvert cointime - 1.2463 + 6.1 \rvert$	$<$	3.0 (ns) ; coincidence time cut for random events
β_{tof}	$>$	0.8 ;
missing mass	$>$	0.89 GeV
missing mass	$<$	1.0 GeV; below two pion threshold
scernpe	$<$	2 ; number of SOS Čerenkov photoelectrons
hcernpe	$>$	2 ; number of HMS Čerenkov photoelectrons

Table 4.1: Cuts summary table for π electro-production data and Monte Carlo (SIMC) for W=1.6 GeV. The definition of the variables can be found in Appendix B.

data various cuts on the detector packages were used for both spectrometers, in addition, to other variables such as β_{tof}, missing mass, $\frac{\Delta P}{P}$, etc. The cuts used to select pions at both values of invariant mass are shown in Tables 4.1 and 4.2.

4.4.1 Electron Identification

In the reaction p(e,e' π)n the scattered electron is detected in the HMS in addition to a considerable background of π^- which contaminates the "true coincident" sample. It is not possible to separate π^- and e^- with the TOF information from the HMS hodoscopes because the resolution is not fine enough. Instead, the HMS gas Čherenkov was used by requiring more than 2 photoelectrons. No cut

Cuts used for data and Monte Carlo($SIMC$)		
$\|hsdelta\|$	$<$	8.0 (%)
$\|hsxptar * 166.37\|$	$<$	14.2 (rad)
$\|hsyptar + 166.37 * hsyptar\|$	$<$	5.9 (rad)
$\|ssdelta\|$	$<$	15.0 (%)
$\|ssxptar * 126.3\|$	$<$	7.0 (rad)
$\|ssyptar + 126.3 * ssyptar\|$	$<$	9.7 (rad)
Particle ID cuts for data only.		
$\|cointime - 1.2463\|$	$<$	3.0 (ns) ; coincidence time cut for real events
$\|cointime - 1.2463 + 6.1\|$	$<$	3.0 (ns) ; coincidence time cut for random events
β_{tof}	$>$	0.6 ;
missing mass	$>$	0.89 GeV
missing mass	$<$	1.0 GeV; below two pion threshold
scernpe	$<$	2 ; number of SOS Čerenkov photoelectrons
hcernpe	$>$	2 ; number of HMS Čerenkov photoelectrons

Table 4.2: Cuts summary table for π electro-production data and Monte Carlo (SIMC) for W=1.15 GeV. The definition of the variables can be found in Appendix B.

was set on the shower counter although it was part of the trigger. A thorough study of these detectors have shown the shower counter to be $> 99.7\%$ efficient and the Čherenkov to be $> 99.8\%$ efficient [48]. For this analysis the detection efficiency is taken to be 99.7%.

4.4.2 Pion Identification

For pion identification in the SOS, two cuts were used to separate the pions from the proton background. The first was a cut on the velocity of the particle as measured from the Time-Of-Flight. The other cut is from the number of photoelectrons detected in the gas Čherekov. Both of these cuts were used for the two SOS polarities, i.e. positive (detection of π^+) and negative (detection π^-).

The pion/proton separation was accomplished by applying a beta cut > 0.8 for W=1.6 GeV and beta > 0.6 for W=1.15 GeV. Beta for the pion was calculated in a similar manner as shown in Equation 4.1, but requiring that the particle is a π. When this cut was applied it eliminated the majority of protons.

$$\beta_\pi \equiv \beta_{momentum}(pion) = \frac{|\vec{p}|}{E} = \frac{|\vec{p}|}{\sqrt{|\vec{p}|^2 + m_\pi^2}}. \tag{4.2}$$

The cut on the Čherenkov detector was used to reject any positrons in the sample. Positrons and protons that survived these cuts were eliminated by random background subtraction (discussed in the next section). The same cuts are used to detect π^- in the SOS at negative polarity. The efficiency is the same for both particles.

4.4.3 Random Coincidence Subtraction

After the cuts have been applied and the pions which correspond to a scattered electron have been selected, it is necessary to remove random coincidence events from the data sample. The random coincidences come from uncorrelated events forming a coincidence, i.e. events from both spectrometers falling within the coincidence time window. These uncorrelated events have to be corrected to get an accurate count of the pion yield.

To determine the coincidence time "**cointime**" a HMS pretrigger starts a time-to-digital converter (TDC), which defines the start clock. This clock is stopped by a pretrigger signal from the *SOS*. This forms the raw coincidence time for the *SOS*. The **cointime** is then corrected for the variations in particle velocity and pathlengths traveled. An offset is added to the electron so that the corresponding pion arrives at the same time. These offsets are due to cable length differences which cause the electronics to have a longer time period to record the event.

Figure 4.3 shows a spectrum of β vs. **cointime** for the *SOS* with no cuts applied. In the top panel, the top row consists of pions and the bottom row consists of protons. The bottom panel shows the electron and in-time pion electroproduction events at 0 ns. The events that do not have the electron and pion events in coincidence are known as "random events". These events are located to the left and right sides of 0 ns and originate from different beam bunches. One can also notice the RF structure of the beam due to the 2.004 ns intervals of the beam bunches delivered in Hall C.

After the particle identification cuts are applied the random events are drastically reduced. The "real" coincidence peak is clearly dominating over the random coincidences. Figure 4.4 shows that the applied cuts mainly reduce the number of counts in the random peaks. Even though the real coincident peak is prominent, there still exist a random pion background underneath this peak. To remove this background, three random peaks were selected to the right of the real

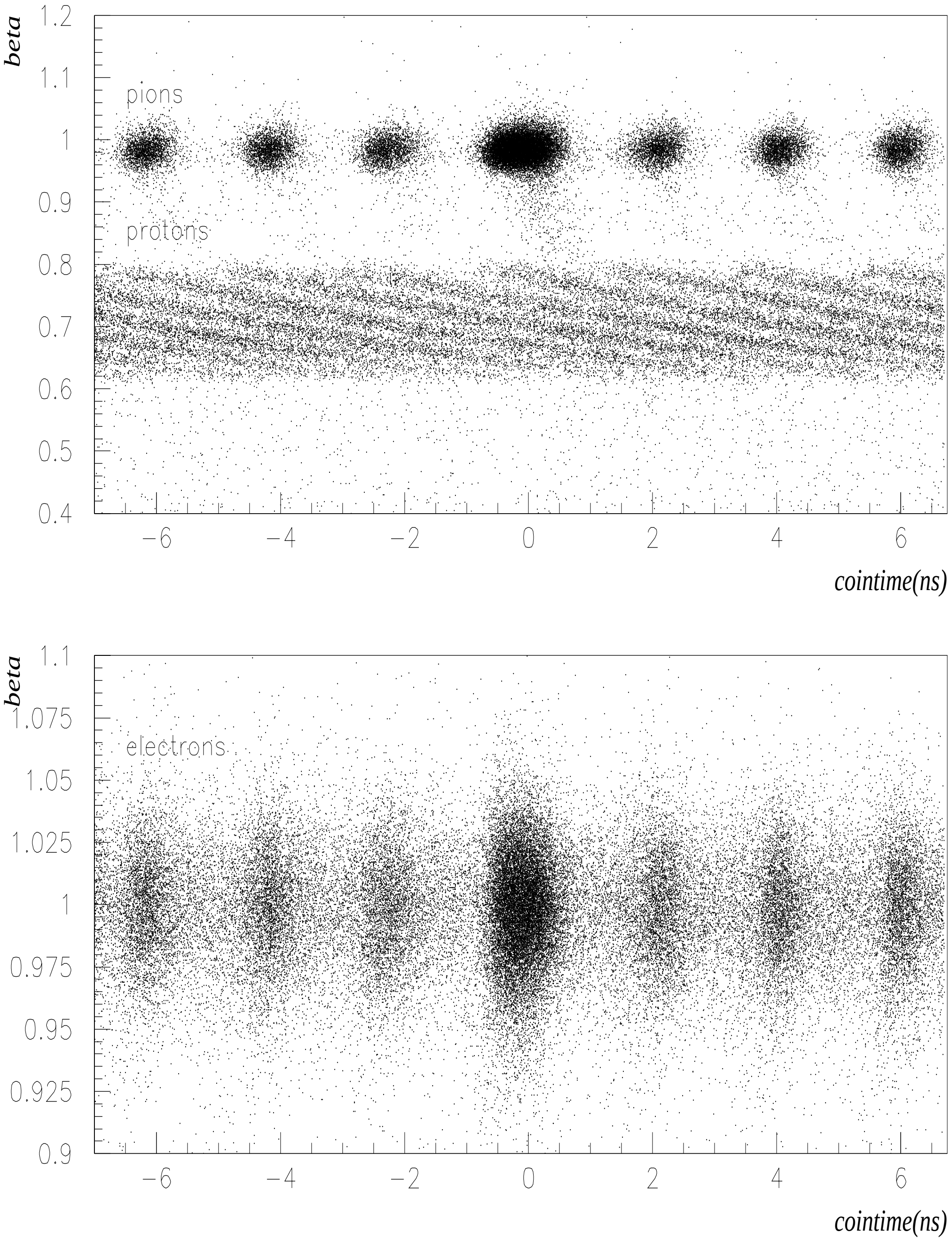

Figure 4.3: Plot of β vs. cointime. In the top figure, the first band corresponds to the pions and the next band corresponds to the protons in the SOS. The bottom figure shows the electrons in the HMS. The electron and in-time pion electroproduction events are at a coincident time of 0 ns.

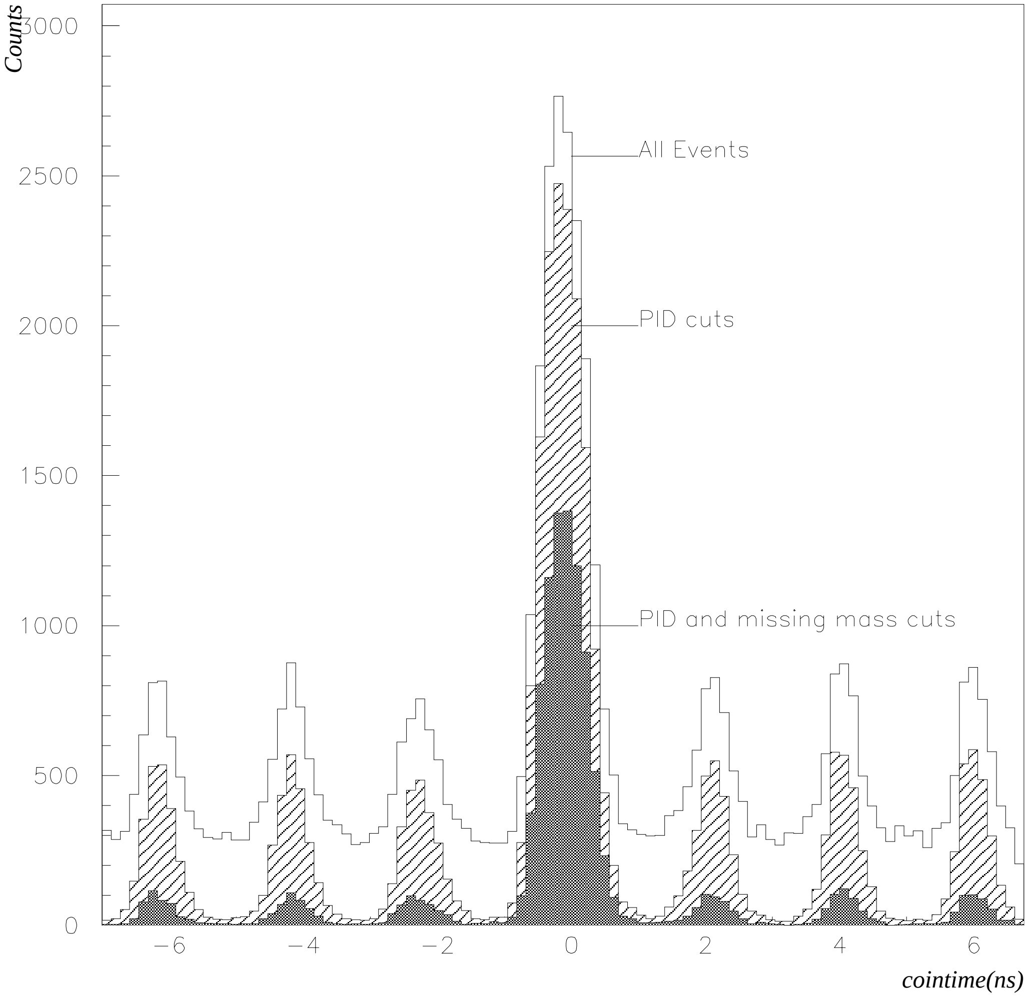

Figure 4.4: Plot of counts vs. cointime. The effect the cuts have on the data is depicted in this figure. The biggest reduction is in the random peaks, while the real coincident peak remains prominent.

coincident peak. Then, the average was subtracted from the real peak. When analyzing the data, we noticed that the cointime drifted from run-to-run up to 2 ns. Which may originate from the fluctuations in the temperature of the electronics room [49]. To correct for this offset, each real coincident peak was fitted and the offset was applied on a run-to-run basis.

4.5 Corrections to Raw Data

In the previous sections, we have described our procedure in extracting a clean sample of pions from the E91003 raw data by applying various particle identification cuts and removing the random background. In order to extract the pion electroproduction cross section we need to account for various additional corrections such as: losses due to absorption, deadtime, detector inefficiencies, etc. In the next sections those corrections and how we estimate their associated errors are discussed.

4.5.1 Trigger Efficiency

The trigger requirements for both the HMS and SOS were that three out of the four scintillators fire. The corresponding probability was calculated from the efficiency of individual scintillators (which was $> 99.8\%$) and is given as:

$$P_{3/4} = P_1P_2P_3P_4 + P_1P_2P_3(1-P_4) + P_1P_2(1-P_3)P_4 + P_1(1-P_2)P_3P_4 + (1-P_1)P_2P_3P_4, \tag{4.3}$$

where $P_1P_2P_3P_4$ is the probability that all four scintillators were fired and P_n the individual nth scintillator plane efficiency. Calculating the probability in this way produced a trigger efficiency of $> 99.8\%$.

4.5.2 Tracking Efficiency

The tracking efficiency was calculated on a run-to-run basis. It is defined as the number of good tracks divided by the number of anticipated tracks. An "anticipated" track is one that has passed through the drift chambers, formed a trigger in the spectrometer, time-of-flight has been calculated, but a good track was not formed. For each run, events that hit the fiducial area of the four scintillator planes are marked. A small area is defined around each mark, which results in a long rectangular tube, and this represents particles that traveled from the drift chamber and have a reconstructed track. The corresponding tracking efficiency for both spectrometers were $95 - 98\%$.

4.5.3 Electronic Deadtime

Electronic deadtime is defined as a lost event due to the simultaneous arrival of two events in front of a logic module. When a signal reaches the discriminator in the trigger logic the electronics generate a 30 ns gate window. If another signal arrives at the module while it is processing the former event, this signal will be lost. These lost events are part of what is called the electronic deadtime.

The probability that a time is allocated between events can be calculated by:

$$P(t) = Re^{-Rt}. \tag{4.4}$$

This equation comes from Poisson statistics which calculates the probability P(t) that events will be lost during a time (t) given the rate (R) of the signals at the input. If τ represents the delay time for the second event to arrive after the first is processed, the electronic live time (ELT) probability is:

$$ELT = \int_{\tau}^{\infty} P(t)dt = \int_{\tau}^{\infty} Re^{-Rt}dt = e^{-R\tau}. \tag{4.5}$$

Assuming R$\tau \ll$1, the ELT can be approximated as ELT = 1 - Rτ. The electronic dead time is not measured directly, but determined by comparing the number of triggers when using logic gates.

During the analysis it was found that the true gate width was 50 ns. The corresponding electronic deadtime is determined by:

$$DT_{elec} = \frac{5}{6}(N_{EL60} - N_{EL120}). \tag{4.6}$$

Where N_{EL60} and N_{EL120} are modules that take pretriggers and put them into gates of 60 and 120 ns, respectively. With this calculation the electronic deadtime is determined for the HMS and SOS and the correction is applied to the data. The determination of the electronic deadtime is discussed in [50].

4.5.4 Computer Deadtime

The computer dead time occurs when the data acquisition is busy processing events and events that come after are lost. This is usually due to a high event rate. The data acquisition system was run in buffered mode to alleviate the load on the system. When the computer is busy, buffered mode takes events waiting to be processed and puts them on standby. Once the computer is finished, it grabs the buffered events for further processing. This dramatically reduces the number of lost events. The computer deadtime is measured directly and is calculated by dividing the triggers by the pretriggers[4]:

$$Computer D.T. = \frac{N_{triggers}}{N_{pretriggers}} - 1 \tag{4.7}$$

4.5.5 Coincidence Blocking

The coincident time is used to relate a scattered electron with a pion from the same reaction. In some cases, a non-coincident or random event can interfere with the timing causing events to be lost due to the cuts in coincidence time. This is referred to as the coincidence blocking. Figure 4.5 depicts how coincidence blocking events can occur in the data. The real coincidences are illustrated by the shaded area, the region to the left shows events created in the SOS from random pions stopping the TDC prematurely. The result is that it gives an early coincident

---

[4] Triggers are the events processed by the trigger supervisor and pretriggers are the total number of triggers created.

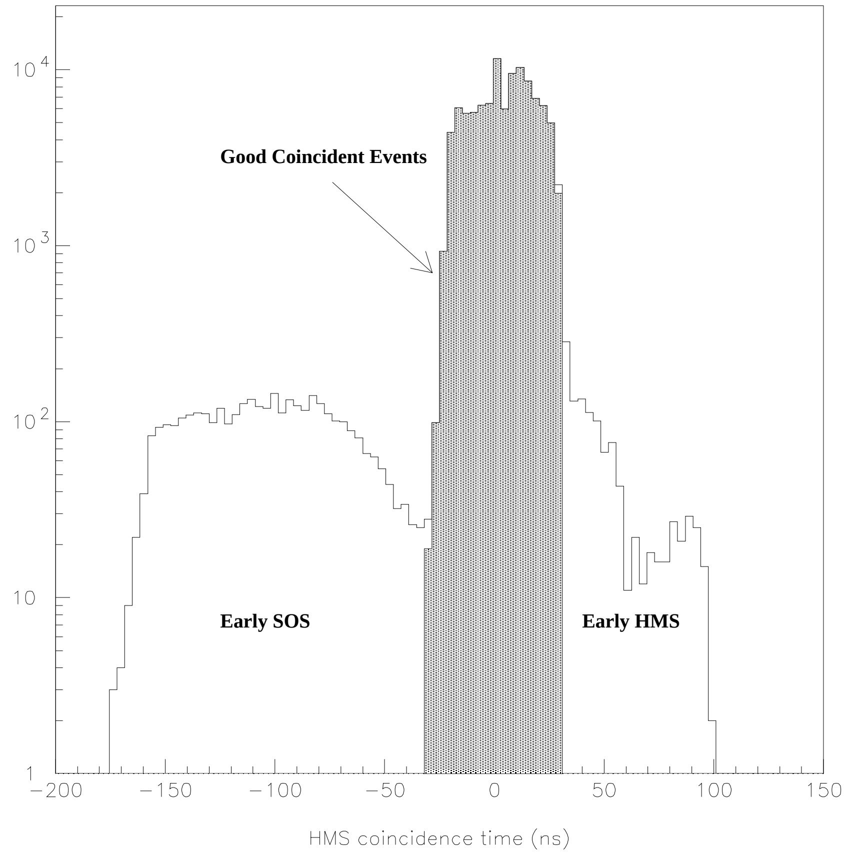

Figure 4.5: Coincidence timing in the HMS illustrating coincidence blocking events. The unshaded areas show early events from the HMS and SOS.

time and the real coincident pion event is never recorded. The region to the right is due to non-coincident electrons starting the TDC too soon. When the coincident pion comes along and “stops the clock”, the coincident time is $\gg$0 and the event is never recorded. A more detailed explanation of coincidence blocking can be found in [50].

4.5.6 ^3He Pressure Correction

During the experiment the helium-3 target cell acquired a small leak. The leak wasn’t big enough to stop operations, however it did affect the target density because the helium-3 target was at high pressure. Consequently, the target pressure was continuously monitored during the run, which allowed one to find the average pressure for the run and apply a normalization factor to the data. The correction was applied on a run-to-run basis at a pressure 130 psi (considered as our ideal pressure), but it fluctuated between 122 and 140 psi. The pressure dependence was approximated using tables which gave an absolute density to an accuracy of about 1% [51]. The pressure fluctuated within 7% for all runs of E91003, which translated to an uncertainty of 0.4%. More details can be found in [31].

4.5.7 Pion Absorption

As the pion travels from the target through the detector stack, it can be absorbed by the materials it passes through. Pions are lost because they experience interactions with nuclei from various materials (see table 3.2). The pion absorption correction was calculated by D. Gaskell and a detailed explanation of the calculation can be found in his thesis [31]. This is one of the larger corrections calculated in the analysis.

Materials with of atomic mass A>4 use a parameterization of the cross section defined by:

$$\sigma_A = \sigma_0 A^q. \tag{4.8}$$

For each material, the cross section is extrapolated from tabulated values of σ_0 and q. Once the cross section is determined, the interaction length is calculated:

$$\lambda = \rho N_A \frac{\sigma_A}{A}, \tag{4.9}$$

where ρ is the density and N_A is Avogadro's number.

The amount of pions that are not absorbed is defined as:

$$T = e^{-\Sigma \lambda_i t_i}, \tag{4.10}$$

with t_i the thickness of the ith material. For materials with A<3, actual data was used where available. Taking all materials into account, a 5.8% correction to the cross section was applied for W = 1.15 GeV and a 3.5% correction for W = 1.6 GeV.

4.5.8 Beta=0

When track reconstruction has failed, due to disagreement of scintillator hits with the track that is found from the wire chambers, the event is given a $\beta = 0$. When an insufficient amount of scintillator hits are recorded, from TDCs/ADCs, the timing information is incorrect and the calculation for β fails.

The effect of $\beta = 0$ was calculated by comparing events with all cuts applied to events with all cuts, except the β one. This gives an error of 0.5% which was assigned to the data.

CHAPTER 5

Results and Conclusions

5.1 Overview

To extract the differential cross section, an iteration technique was especially developed for this analysis. The theoretically-based input models used in the simulation did not include cross section calculations for the deuteron and helium nuclei. To account for those, Fermi motion was added to the nucleon cross section (proton and neutron). This procedure is explained in section 5.2.1.

The cross section depends on three Lorentz invariants. For hydrogen, the variables used were (Q^2, W, and t), but for the nuclear targets the variables used were (Q^2, W, t, ϕ, and P_π). The extra variables in the nuclear targets were introduced because of extra degrees of freedom. The final cross sections to be quoted are a result of cross section models developed to agree with our measured data:

$$\frac{d\sigma}{d\Omega}(Q^2, W, t)_{hydrogen} = \frac{d\sigma}{d\Omega}(Q^2, W, t)_{initial} A(Q^2) B(W) C(t), and \tag{5.1}$$

$$\frac{d\sigma}{d\Omega}(Q^2, W, t, P_\pi, \phi)_{nuclear} = \frac{d\sigma}{d\Omega}(Q^2, W, t, P_\pi, \phi)_{initial} A(Q^2) B(W) C(t) D(P_\pi) E(\phi). \tag{5.2}$$

$A(Q^2)$, $B(W)$, $C(t)$, $D(P_\pi)$, and $E(\phi)$ are correction functions that account for initial inequalities between the data and input Monte Carlo models. While $A(Q^2)$, $B(W)$, and $C(t)$ were determined in part by applying two dimensional cuts to make the cross section dependence as independent as possible of other variables, the $D(P_\pi)$ and $E(\phi)$ correction factors were done by applying one dimensional cuts. This will be discussed in detail.

$\frac{d\sigma}{d\Omega}_{initial}$ corresponds to the model cross section with no iterations. The cross section is extracted using:

$$\left\{\frac{d\sigma}{d\Omega}\right\}_{data} = \frac{Yield_{data}}{Yield_{model}} * \left\{\frac{d\sigma}{d\Omega}\right\}_{model} \tag{5.3}$$

where $Yield_{SIMC}$ is the number of pions generated from the Monte Carlo, $\left\{\frac{d\sigma}{d\Omega}\right\}_{SIMC}$ is the model cross section, and $Yield_{data}$ is the number of pions in the data.

As mentioned earlier, the nuclear targets require extra degrees of freedom due to the Fermi motion inside the nucleus. Therefore, the cross section was first evaluated at a point, corresponding to a particular Q^2, W, and t kinematic value, integration over all possible pion momenta. In this way the six-fold integration of the cross section reduces down to a five-fold cross section. This method was achieved using the Monte Carlo in what is referred to as a “point spectrometer mode”, also to be discussed below.

5.2 Cross Section Extraction

As mentioned earlier, the cross section was not extracted purely from data. Instead, the ratio of the data yield was compared to the Monte Carlo yield and then a data cross section was calculated by multiplying the yield ratio by the model cross section after a model was developed to be in good agreement with data. Hence, the model developed was a crucial procedure.

In addition to this, it was necessary to account properly for corrections and inefficiencies in the experimental data.

The measured yield is defined as:

$$Y(\Delta V) = N_e N_T \frac{d^5\sigma}{dV^5} \Delta V R, \tag{5.4}$$

where

- $N_e = \frac{(Q)}{(e)}$ is the number of electrons incident on the target;
- $N_T = \frac{\rho t}{A N_A}$ is the number of target nuclei;
- N_A is Avagadro's number;
- ρ is the target density;
- t is the target thickness;
- A is the mass number;

- $\frac{d^5\sigma}{dV^5}$ is the five-fold differential cross section;
- ΔV is the phase space volume; and
- R is the radiative corrections multiplicative factor.

The first major goal of the analysis was to get from measured yields to the five-fold differential cross section. The data yield is:

$$Y(\Delta V) = N_e N_T \int_{\Delta V} \frac{d^5\sigma}{dV^5} C_n J A(V) R(V) dV \tag{5.5}$$

where

- C_n are the correction factors, such as π decay, detector inefficiencies, etc.;
- J is the Jacobian that transforms the cross section from lab to center-of-mass coordinates and is calculated on an event-by-event basis using J = $|\frac{dcos\theta}{dcos\theta^*}|$;
- $A(V)$ are the spectrometer acceptance corrections;
- $R(V)$ are the radiative corrections; and
- $\Delta V = \Delta\Omega_e \Delta E_e \Delta\Omega_\pi$.

The radiative effects occur spontaneously in nature. The acceptance reflects the probability that a particle is transported through the spectrometer to the detectors, and depends on spectrometer geometry, magnetic fields, detector size, etc. In practice these effects are accounted for in the data by simulation in the Monte

Carlo spectrometer model and compared with data. This procedure is validated by ensuring that the data/Monte Carlo ratio goes to 1. It is difficult to include all the physics in the Monte Carlo, so the major effects are explicitly implemented, while others are estimated, and some are included in the error analysis. This last case is for final state interactions in this work. An ideal Monte Carlo would contain all possible physics.

Equation 5.5 illustrates the case for pion production off a hydrogen target. The cross section depends on the magnitude and direction of the electron, and the pion 4-momentum. When going to deuterium and helium-3, the case is a little different because one has to take into account the momentum of the recoil (spectator) nucleon. The corresponding yield is then:

$$Y(\Delta V) = N_e N_T \int_{\Delta V} \frac{d^6\sigma}{dV^6} C_n J A(V) R(V) dV dP_\pi, \tag{5.6}$$

where

$$\Delta V = \Delta\Omega_e \delta E_e \Delta\Omega_\pi \Delta P_\pi. \tag{5.7}$$

P_π is a function of the nucleon momentum[1]. The objective here was to isolate the quasifree part of the reaction to compare that cross section to hydrogen, after integrating out the contribution from the nuclear momentum distribution. Once

---

[1] Compared to the hydrogen case, the nucleon involved in the reaction mechanism is not at rest anymore. Hence, the integration over P_π takes into account the Fermi motion of nucleons in the nucleus.

the five-fold cross sections were obtained, the cross sections were expressed in terms of the center-of-mass variables:

$$\frac{d^5\sigma}{d\Omega_e dE_e d\Omega_\pi} = \Gamma J \frac{d\sigma^{CM}}{d\Omega_{\pi^\pm}}, \tag{5.8}$$

where the transverse virtual photon flux factor Γ is expressed as

$$\Gamma = \frac{\alpha}{2\pi^2} \frac{E' K_{eq}}{E Q^2 (1-\epsilon)}. \tag{5.9}$$

The equivalent photon energy K_{eq} was defined as

$$K_{eq} = \frac{W^2 - m_N}{2m_N}, \tag{5.10}$$

using the mass (m_N) of the nucleus for all targets.

As a reminder, the input model calculated the cross section per nucleon. It did not contain a calculation for nuclear targets.

5.2.1 Iteration Method

The general flowchart of the method is displayed in figure 5.1. The iteration of the Monte Carlo cross section for agreement with data starts with the phase space distributions of Q^2, W, and t. To extract the individual dependencies the variables have on each other, the iteration procedure began with first plotting two

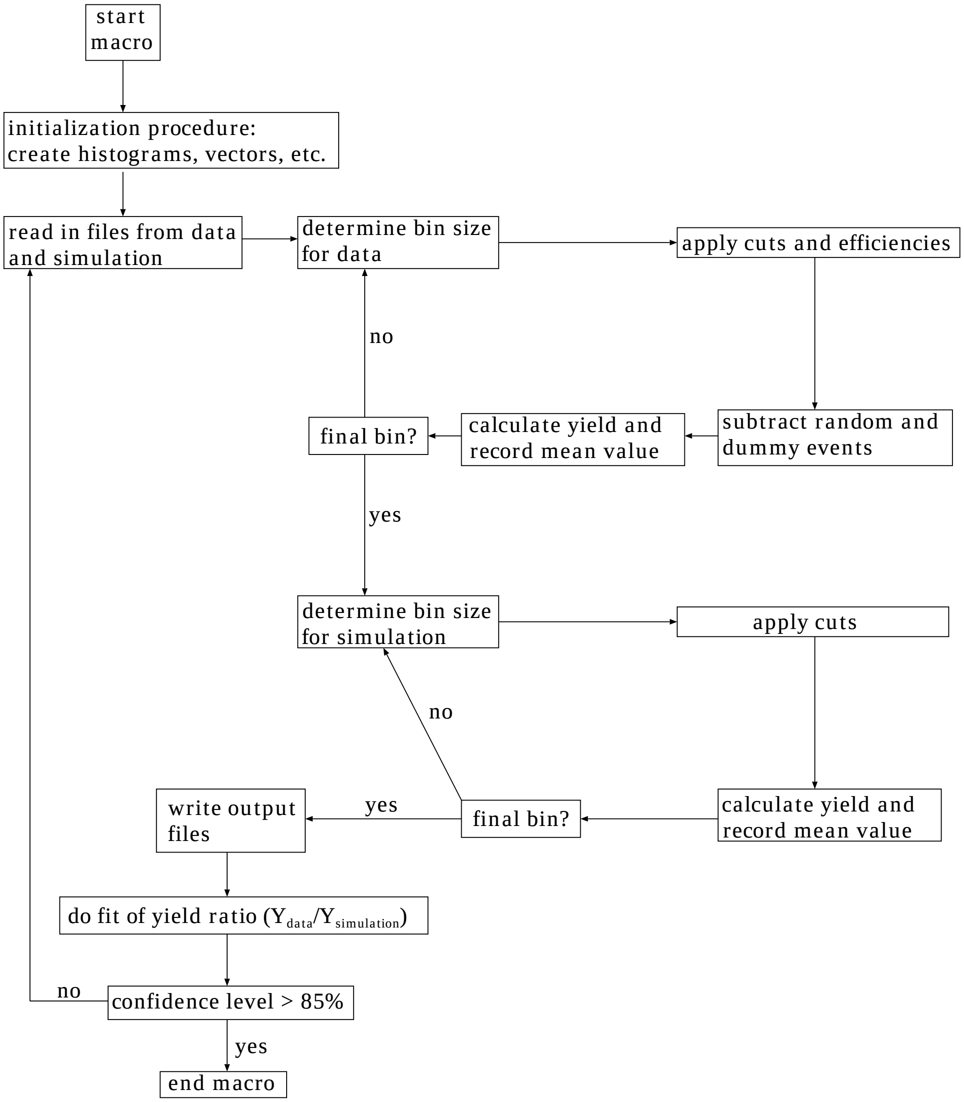

Figure 5.1: General flowchart of iteration procedure.

dimensional histograms of the three variables as a function of each other to see their relationship with one another, figure 5.2. For all kinematic settings, the full range in all variables were taken. A graphical display package, *PAW* (*P*hysics *A*nalysis *W*orkstation) [53], was utilized to analyze and interpret experimental and simulated data. A macro program, a list of PAW commands, was written for each variable at each setting to determine the dependency on the variable. The macro initializes histograms, applies all necessary cuts [2], applies corrections for inefficiencies, compares the data to Monte Carlo yields, and extracts the correction functions for each variable of the phase space to obtain the new model. Each time a correction function for a variable is calculated it is multiplied to the model and the next correction function calculated has the new input model.

After the first iteration, the "new" iterated model become:

$$\sigma^{iterated}_{hydrogen} = \sigma^{initial} * f(Q^2) * f(W) * f(t) \tag{5.11}$$

$$\sigma^{iterated}_{nuclear} = \sigma^{initial} * f(Q^2) * f(W) * f(t) * f(\phi) * f(P_\pi) \tag{5.12}$$

For the next iteration, the routine starts at Q^2 and scrolls through all functions until the data and Monte Carlo are in agreement to a confidence level of $> 85\%$. Typically, it took 1-3 iterations for the model to converge.

---

[2] HMS and SOS delta, missing mass, SOS beta, detector cuts.

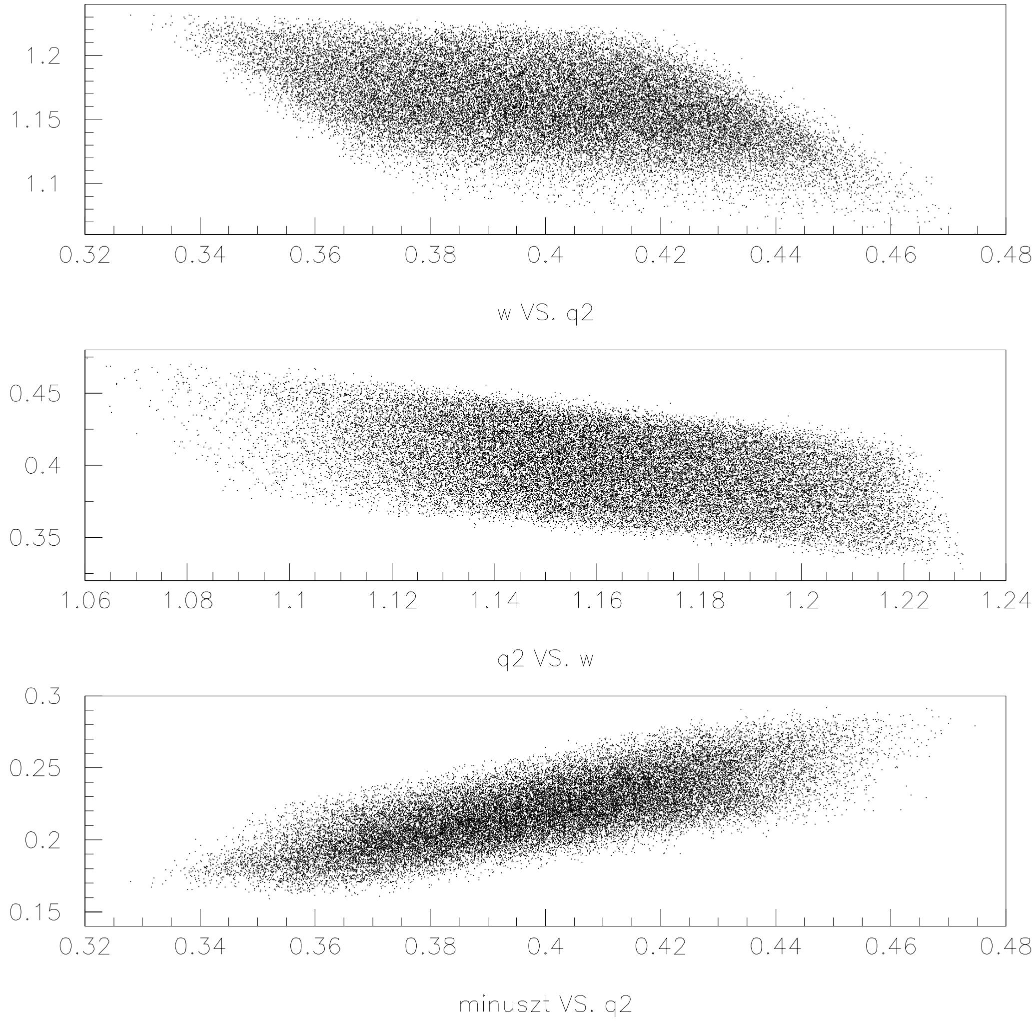

Figure 5.2: The Q^2, W, and t coverage at W=1.15 GeV, ϵ=0.86 of **E91003**. The distributions are from the Monte Carlo and are examples of the starting points for the iteration procedure.

There were three main processes to the iteration procedure: determination of the two dimensional cuts, determination of the best fit, and extracting the cross section.

Determining the best 2-D cuts for the two dimensional distributions was a crucial component of the iteration procedure. Starting with Q^2 was an artbitary choice; any other variable would have been appropriate. The diagonal cuts served as a way to quickly remove the dependencies between variables.

The relationship between Q^2 and W is easily seen through:

$$W = M_p^2 + 2\nu M_p - Q^2 \tag{5.13}$$

$$Q^2 = 4EE'sin^2\frac{\theta_e}{2} \tag{5.14}$$

where E and E' are the initial and scattered electron energy, θ_e is the angle of the scattered electron w.r.t. the initial electron, M_p is the mass of the proton, and ν = (E-E'). The relationship with the Mandelstam variable t follows from:

$$t = (q - P_\pi)^2 \tag{5.15}$$

$$-t = -Q^2 + M_{hadron}^2 - 2 \cdot [\nu \cdot E_\pi - (\vec{q} \cdot \vec{P}_\pi)] \tag{5.16}$$

where M_{hadron} is the mass of the hadron, E_π is the energy of the pion, and $\vec{q} \cdot \vec{P}_\pi$ is the scalar product between the virtual photon and the pion.

The iteration procedure attempts to create independent correction functions. To illustrate the technique, figures 5.3 and 5.4 shows the (W, Q^2) phase space for their full range and on a bin-to-bin basis, respectively. The diagonal cut results from a linear relation:

$$y = mx + b, \tag{5.17}$$

where y is W and x is Q^2.

Once the cuts are determined with the appropriate binning, each bin is analyzed run-by-run, see figure 5.4. Corrections for all ineffiencies, subtraction of random events and subtraction of target endcap contributions are accounted for during the procedure. With all runs analyzed, the mean value for the bin was calculated and the macro moved to the next bin until all bins have been analyzed. For each data bin, the routine will repeat the same procedure using Monte Carlo events.

When the macro finished, the data and Monte Carlo were compared to see how well they were in agreement by fitting the yield ratio data-to-Monte Carlo, with a 2nd degree polynomial via the use of a separate Fortran function. The determination of the "best fit" was done in a series of steps and with a list of criteria. This will be discussed in the next section. For each iteration, the model is corrected using the Fortran based function until convergence is achieved. Figure 5.5 gives an example of what the data to Monte Carlo yield ratios looks like before and after corrections have been done on the model. Once the model accurately

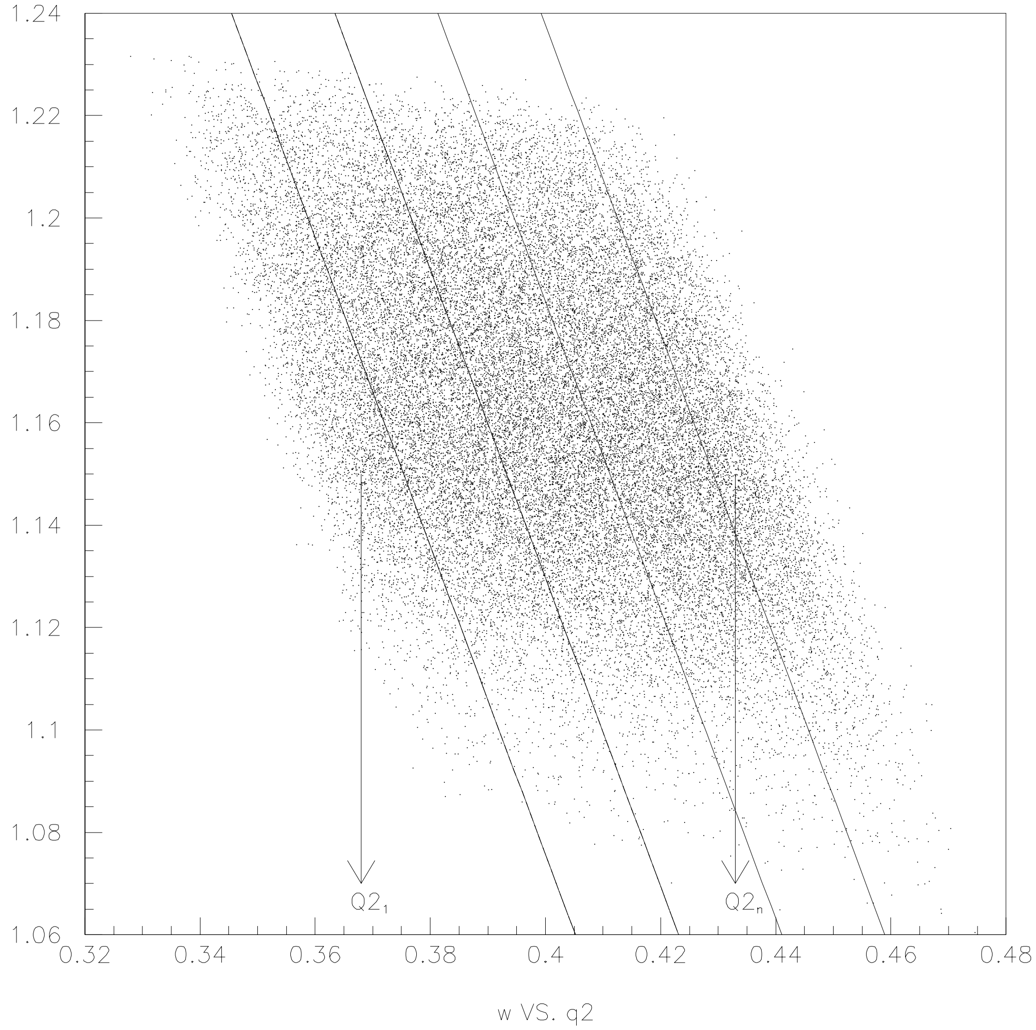

Figure 5.3: The (Q^2,W) 2D cut as used in our analysis procedure. Each band corresponds to a range in Q^2 for a fixed W value obtained by a weighted mean average.

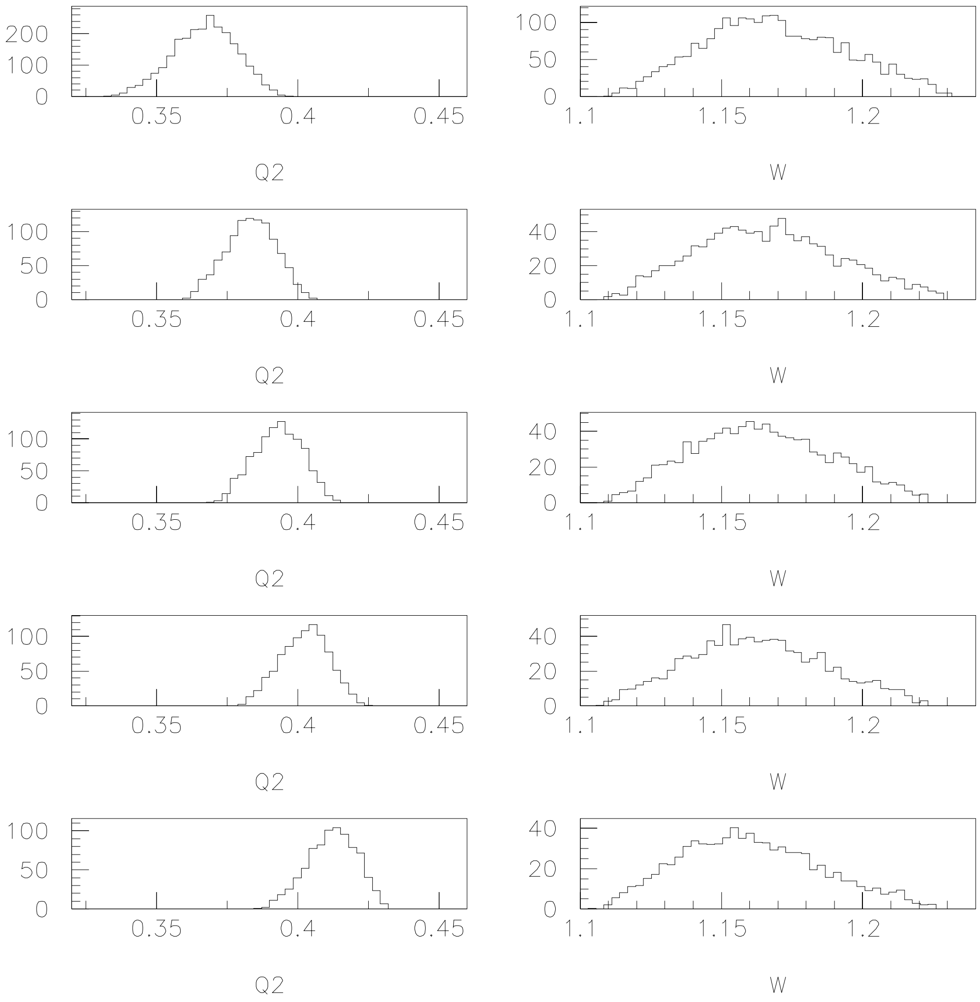

Figure 5.4: Bin-to-bin Q^2 and W distributions. Notice how Q^2 changes while W remains fairly constant.

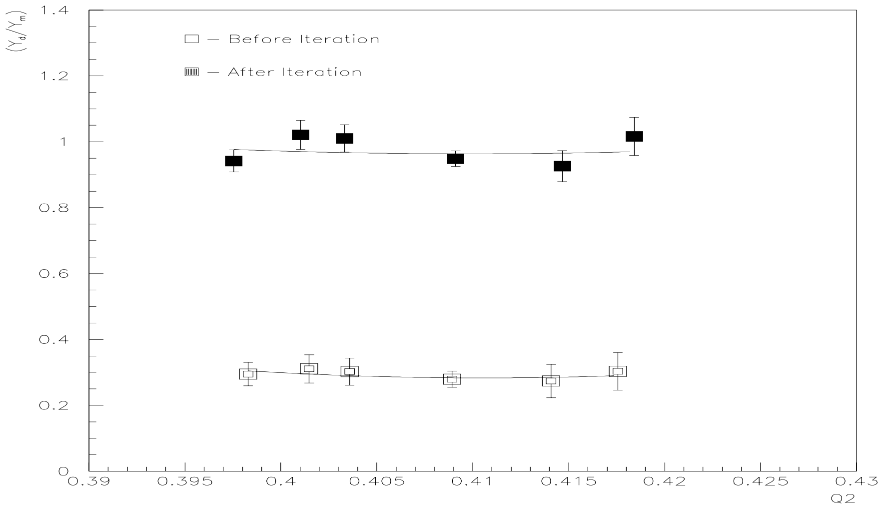

Figure 5.5: Before (open squares) and after (filled squares) the iteration procedure for Q^2. The kinematics are at W=1.15 GeV and ϵ of 0.43. The error bars shown are statistical only.

depicted the data (yield ratio ≈1), the cross section was calculated.

Determining the best parameters from the iteration procedure required finding the best fit when comparing data to Monte Carlo. The standard measure of "goodness of fit" called χ^2, was utilized.

$$\chi^2 = \sum_{i=1}^{n} \frac{(y_i - f(x)_i)^2}{\sigma_i^2}, \tag{5.18}$$

where y_i are the data points we are trying to fit to a function $f(x)_i$. σ_i^2 is the standard deviation of the measurement i. The best fit is the one for which this parameter is at its minimum, i.e. the smallest.

The confidence level required for determining the parameters from the iteration method was $> 85\%$. After the correction function was completed for a given variable, a hypothesis test was done to determine if the optimum set of parameters were chosen. Basically, the test consisted of finding the reduced χ^2, then extracting the confidence level. If it was below 85%, the cuts for the given variable were adjusted and the process was done over again until the desired confidence level was achieved. This assured that the best parameters were chosen.

Once the model converged, plots of various physics variables were done for data to Monte Carlo comparison. As a secondary test for the reliability of the model, χ^2 was calculated for target, focal plane and physics variables to see if there were any remaining big discrepancies between the data and Monte Carlo.

5.2.2 Data to Monte Carlo Comparison

This section demonstrates how well the iterated model simulates the data. After running the iteration procedure and making the necessary checks to ensure the optimum model had been achieved, the simulated yield was compared with the data. Twenty different variables[3] are compared which included target, focal plane, momentum, and physics quantities.

Only one final state is possible for the hydrogen target: $^1H(e,e'\,\pi^+)$n. The cross sections from hydrogen will be used as a reference for the quasifree production on the nuclear targets. On the deuterium, there are two possible reactions, each

---

[3] See Appendix B

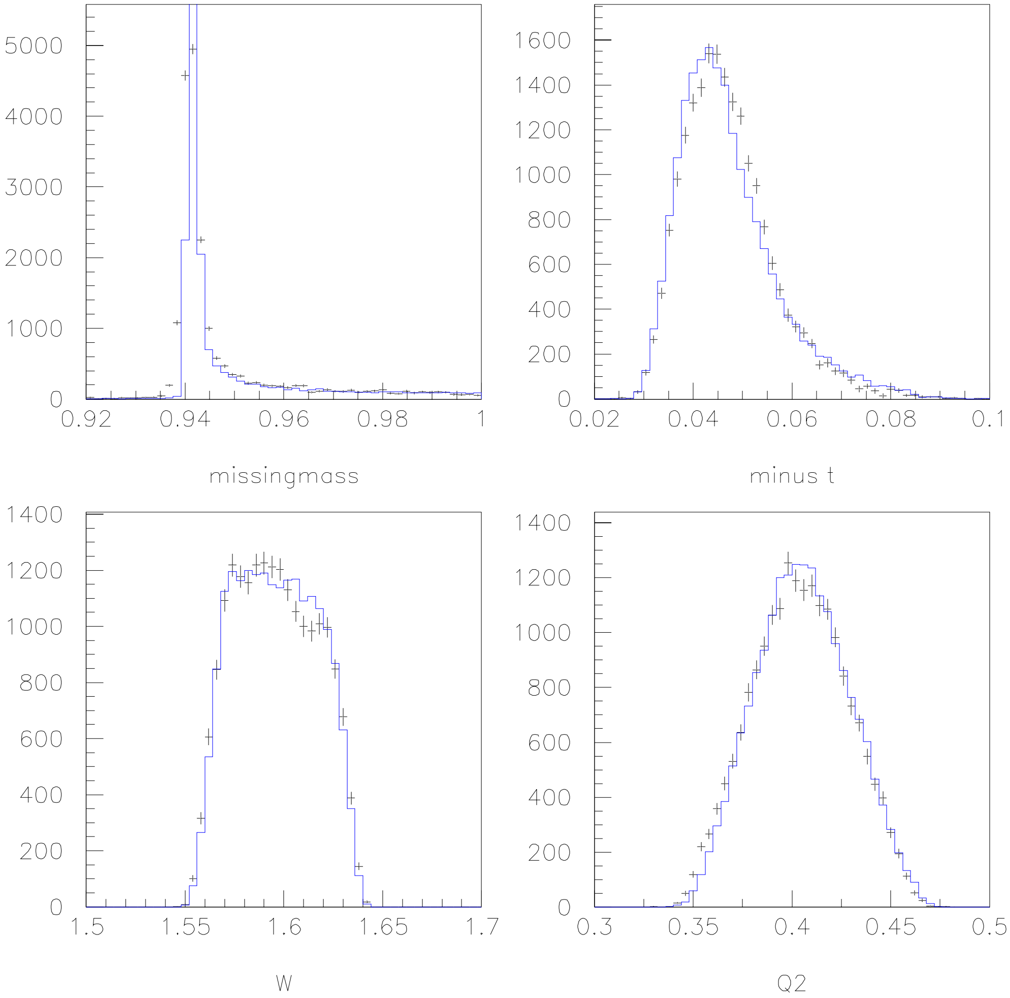

Figure 5.6: Spectra for hydrogen at W = 1.6 GeV, $Q^2 = 0.4 GeV^2$, and $\epsilon = 0.49$. The model shows good agreement with data.

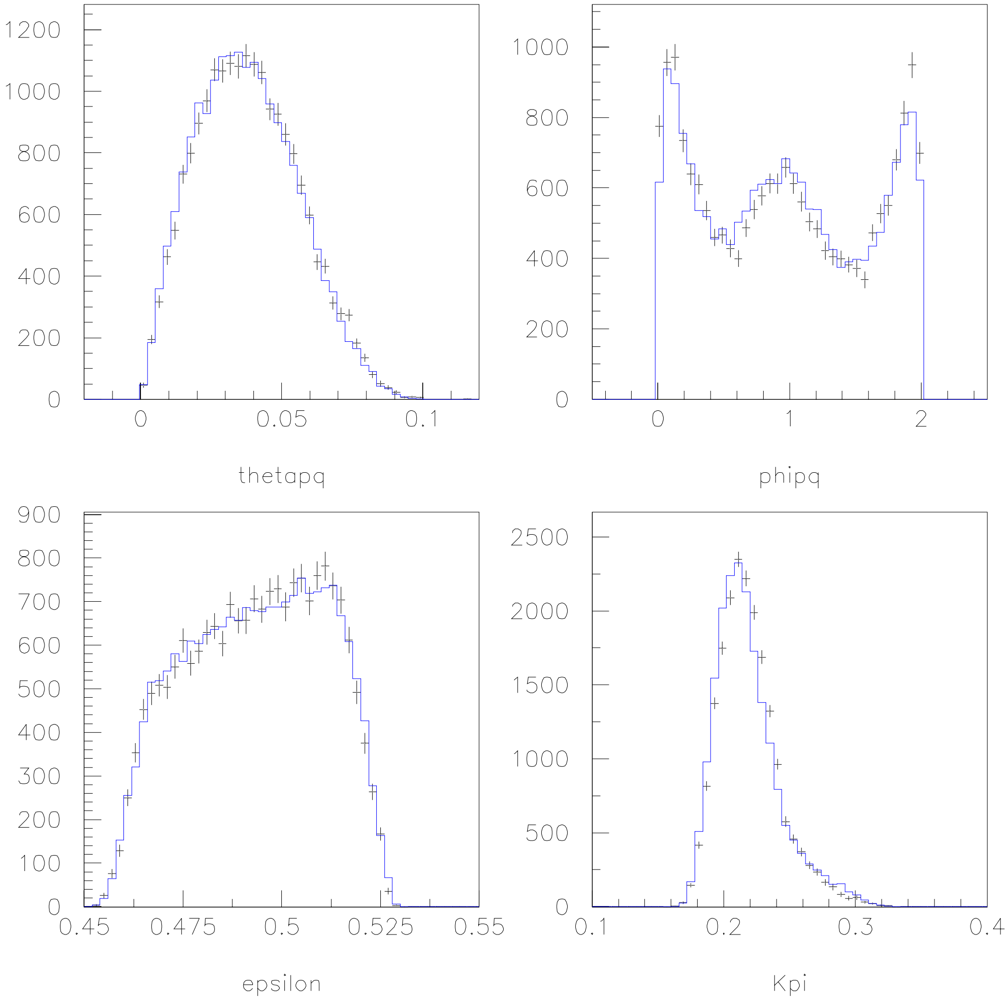

Figure 5.7: Spectra for hydrogen at W = 1.6 GeV, $Q^2 = 0.4 GeV^2$, and $\epsilon = 0.49$. The model shows good agreement with data.

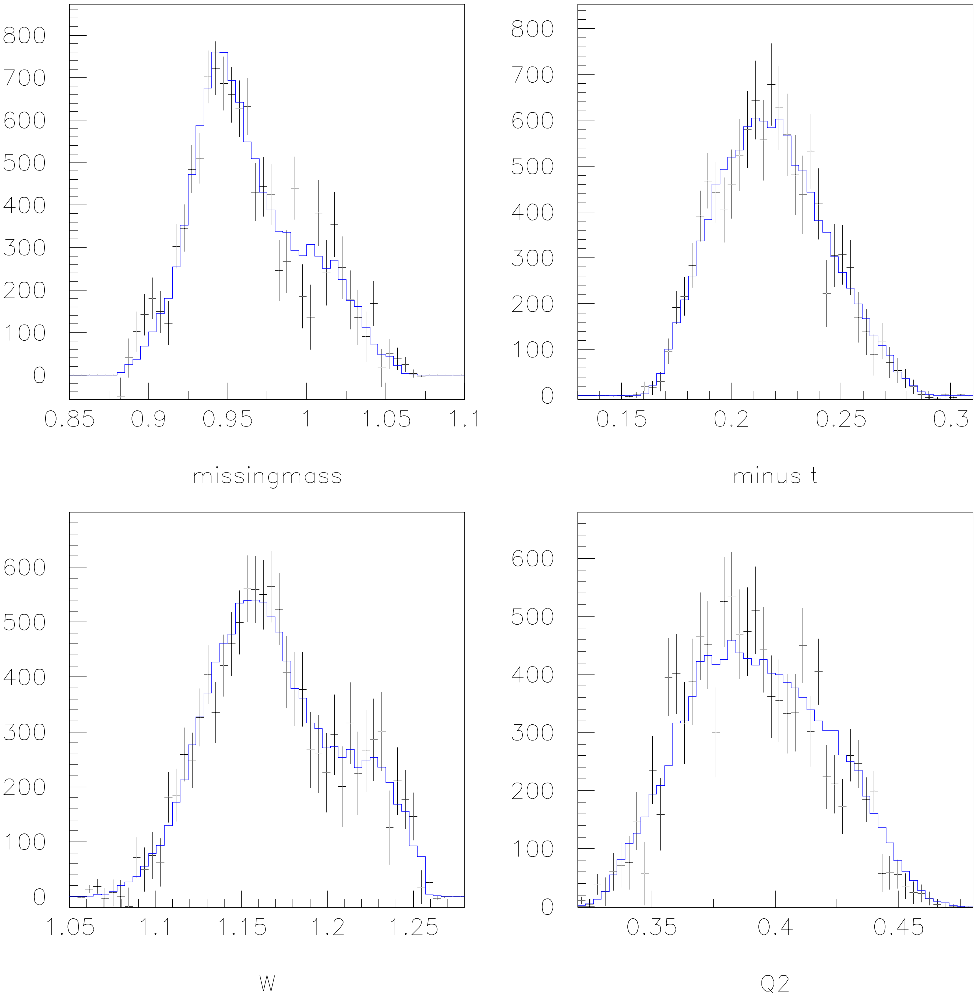

Figure 5.8: Deuterium target of the reaction $^2H(e,e'\ \pi^+)$nn for W = 1.15 GeV, $Q^2 = 0.4GeV^2$, and $\epsilon = 0.86$. The effects of Fermi smearing can be seen in the missing mass plot when compared to hydrogen.

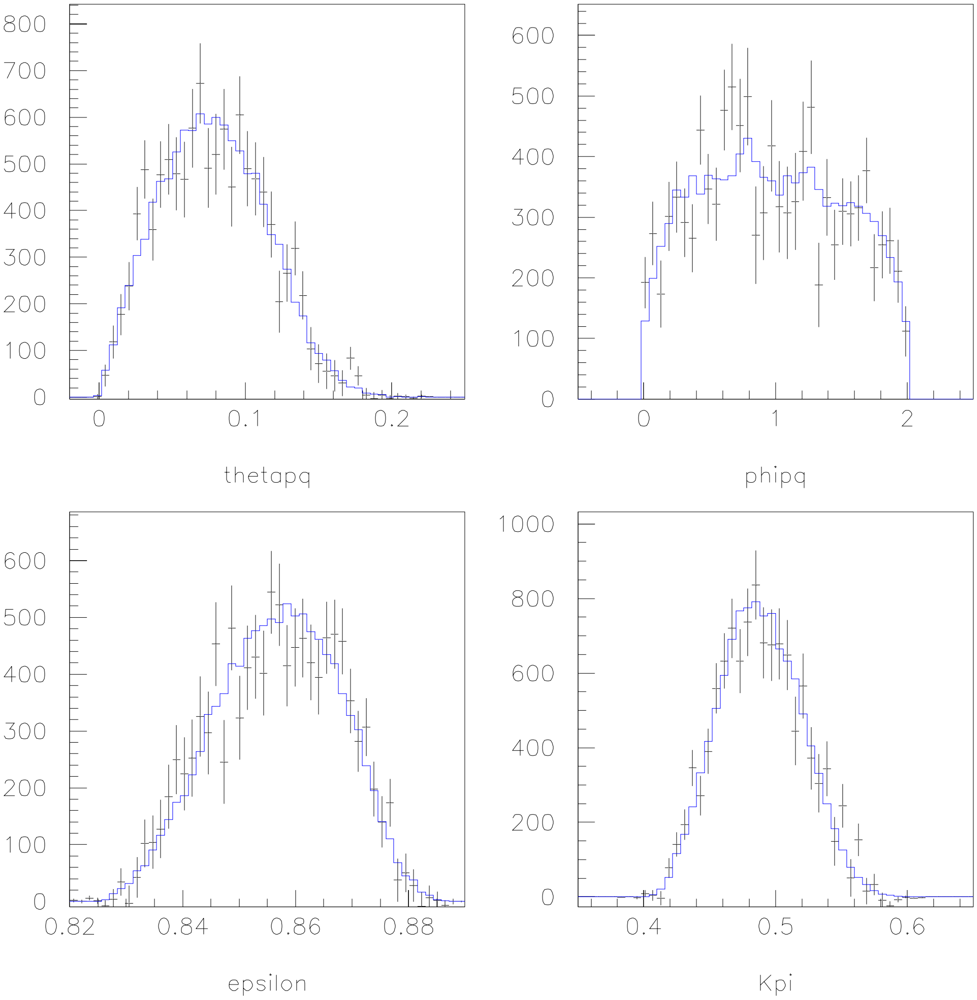

Figure 5.9: Deuterium target with the reaction ${}^{2}H(e,e'\ \pi^{+})$nn for W = 1.15 GeV, $Q^2 = 0.4\ GeV^2$, and $\epsilon = 0.86$

having one final state: ${}^2H(e,e'\pi^+)$nn, and ${}^2H(e,e'\pi^-)$pp. As one moves from hydrogen to deuterium, the effect of Fermi smearing in the missing mass spectra is apparent. The momentum shared by the nuclei is taken into account when the cross section is calculated.

In the case of helium-3, there are multiple final states for π^+ production and one final state for π^- production. At $W = 1.6$ GeV the recoil momentum of the struck nucleon is strong enough to clearly show the ${}^3H$ bound state. But for $W =$ 1.15 GeV this coherent channel does not have enough energy to be “kicked” out and therefore cannot be seen. The possible reactions on ${}^3He$ are: ${}^3He(e,e'\pi^+){}^3H$, ${}^3He(e,e'\pi^+){}^2Hp$, ${}^3He(e,e'\pi^+)$pnn, and ${}^3He(e,e'\pi^-)$ppp.

π^+ production from ${}^3He$, at W=1.6 GeV is unique from the other targets because of its multiple final states: the π^+ coherent production from ${}^3He$ as well as the deuterium-neutron bound state and the quasifree production. To extract the cross section, all final states were modeled separately in the Monte Carlo. A hard cut was placed on the triton state and then it is fitted to find the portion of the curve that is in the Dn and pnn continuum states. The Dn and pnn continuum states were convoluted and could not be separated. Therefore, it was taken to be one state in the iteration procedure. A missing mass spectrum for π^+ production from ${}^3He$, at W=1.6 GeV, is shown in fig. 5.12. All final states are represented and the data (crosses) are superimposed on the model (solid line).

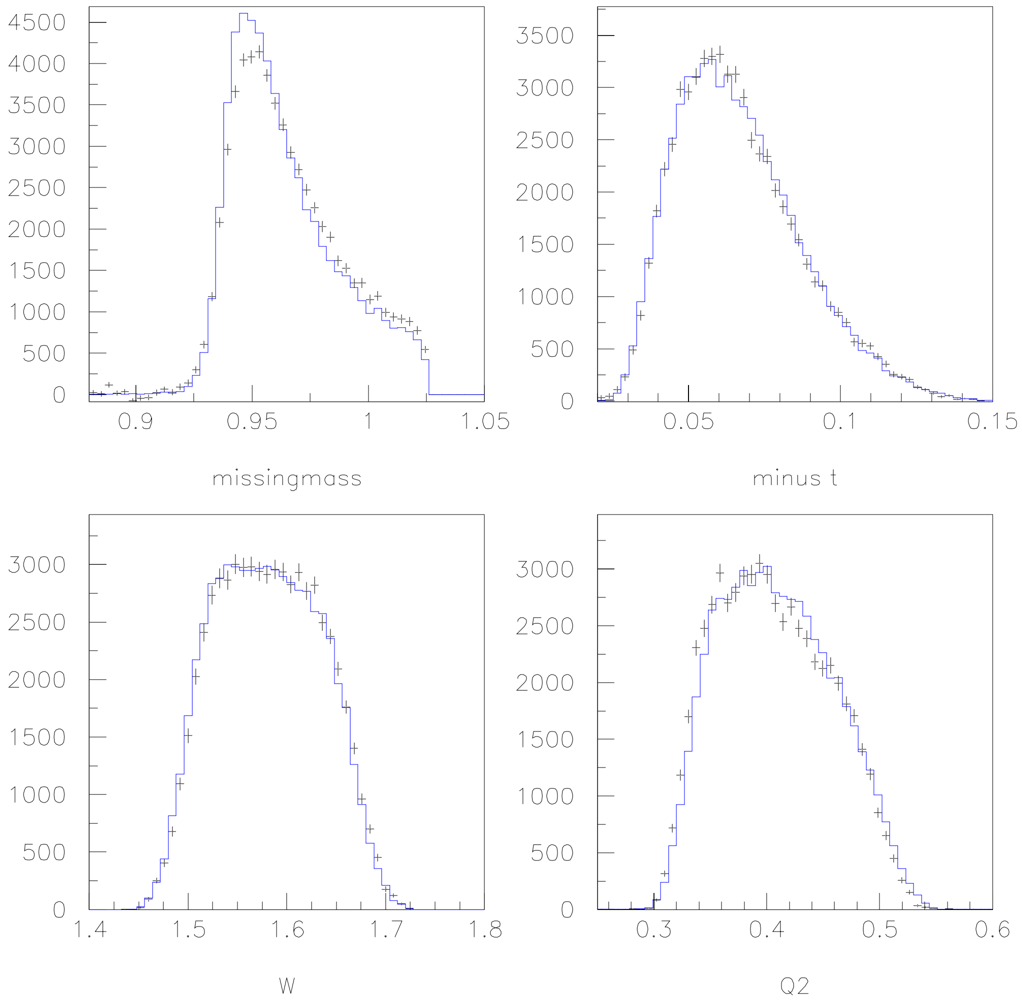

Figure 5.10: Plot of $^3He(e,e'\pi^-)ppp$ reaction, at $W = 1.6$ GeV $\epsilon = 0.89$, for invariant quantities. The model does a good job in reproducing the data, but there are areas where the model over-compensates or under-compensate.

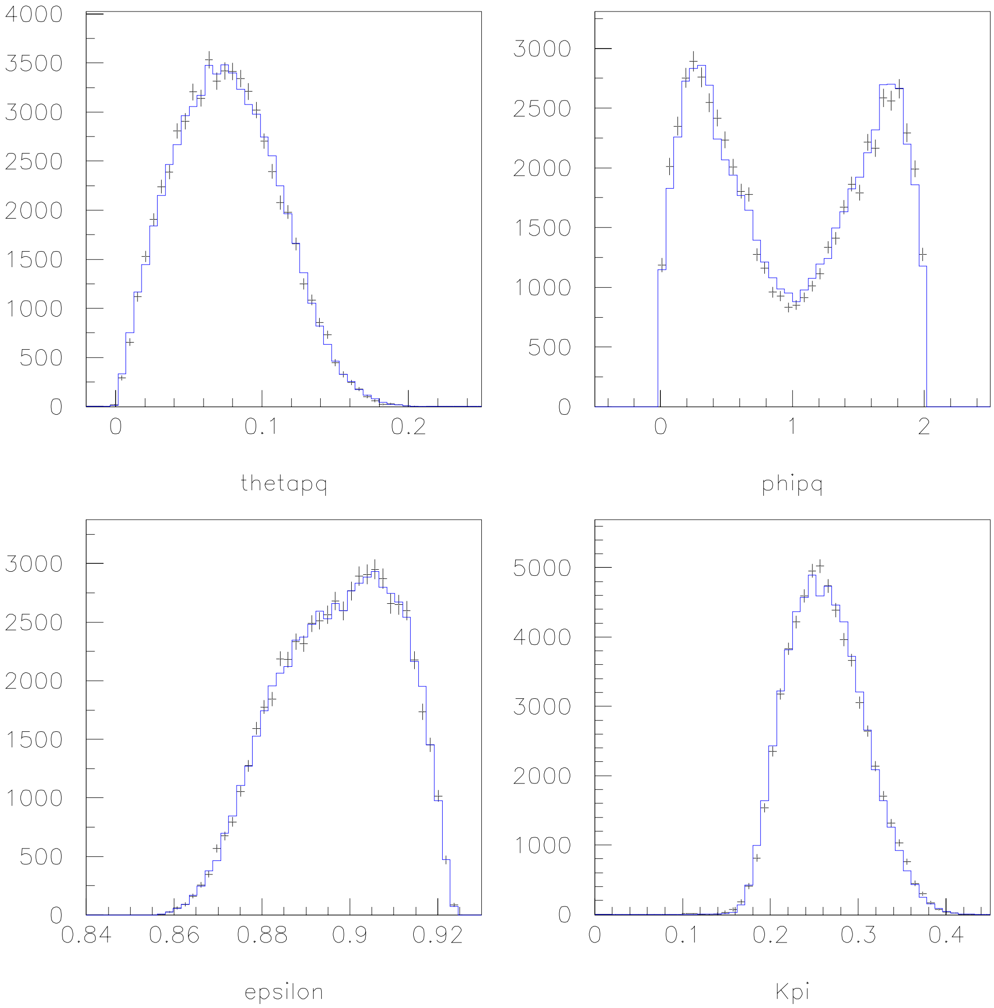

Figure 5.11: Data to Monte Carlo comparisons of $^{3}He(e,e'\pi^{-})ppp$ reaction, at W = 1.6 GeV ϵ = 0.89

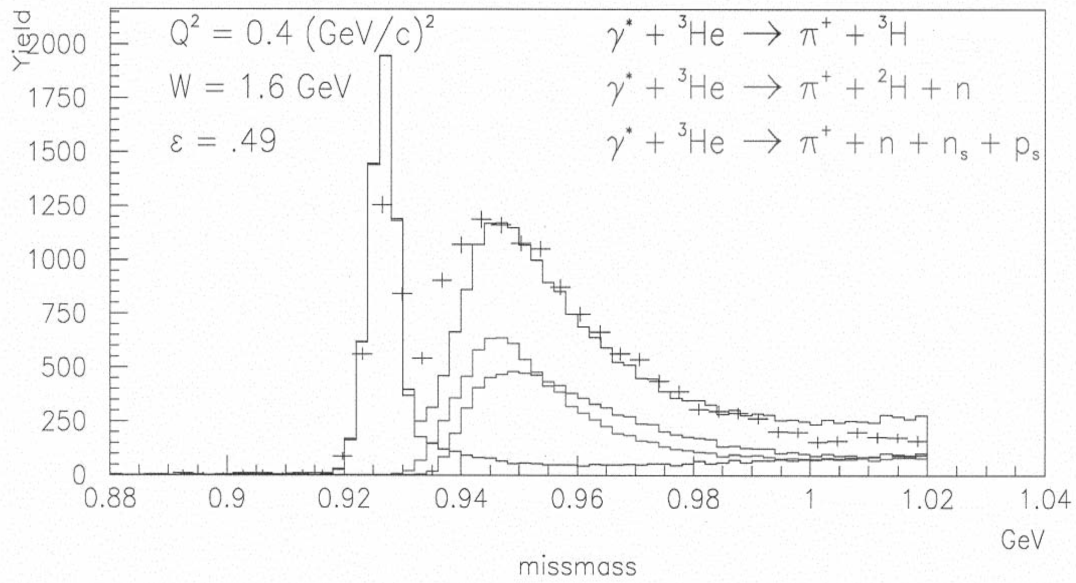

Figure 5.12: Helium-3 target with the reaction ${}^3He(e,e'\ \pi^+)$nnp, Dn, ${}^3H$ for W = 1.6 GeV, $Q^2 = 0.4\ GeV^2$, and $\epsilon = 0.49$.

5.2.3 Error Analysis

Error analysis is necessary because not only one cannot exactly measure how nature behaves or reacts in a given situation, but also any man-made apparatus is not perfect. Any measurement is prone to some degree of uncertainty. Experimental uncertainties can be put into two cateorgies - statistical and systematic. Systematic uncertainties are not random, but are known uncertainties in measurement. They are typically associated with calibration errors and can be hard to quantify. In the calibration process, one measures known values, or compare the values obtained from a particular equipment with those obtained from a more accurate instrument. They arise when the device is not operating correctly or if the experimental procedure is inappropriate or incorrectly applied. Errors of this kind are more difficult to find, but usually a problem with the experiment will become apparent as the analysis continues. Nevertheless, understanding the magnitude of systematic errors are crucial.

Systematic errors can be broken down into two groups: “random” (uncorrelated) and “scale” (correlated) errors. Random errors, like dead times and detector efficiencies, are exclusive to a particular kinematic setting. When performing an L-T separation, random systematic errors must be included at each ϵ setting since they can affect the outcome of the linear fit. Scale errors affect all kinematic settings in the same manner, making it a global quantity. Examples of scale systematic errors would be the charge measurement and target thickness.

The sources and magnitudes of uncertainties are listed in Table 5.1. Further discussion of the uncertainties that were measured, for experiment E91003, can be found throughout this thesis.

5.3 Unseparated Cross Sections

The unseparated cross sections are calculated by integrating the 6-fold cross section over the pion momentum acceptance. Of course, for hydrogen this is simply a five-fold cross section because the pion momentum for hydrogen depends on the direction of the pion and the magnitude of the electron. Integration over the pion momentum acceptance simply gives a delta function. Deuterium and helium-3 have an extra degree of freedom and the cross section has a 6-fold dependence. The right side of eqn. 1.8 can be written as:

$$\frac{d\sigma^{CM}}{d\Omega_\pi dP_\pi} = \frac{d\sigma_T}{d\Omega_\pi dP_\pi} + \varepsilon_L \frac{d\sigma_L}{d\Omega_\pi dP_\pi} + \sqrt{2\varepsilon_L(\varepsilon+1)}\frac{d\sigma_{LT}}{d\Omega_\pi dP_\pi}\cos\phi + \varepsilon\frac{d\sigma_{TT}}{d\Omega_\pi dP_\pi}\cos 2\phi. \tag{5.19}$$

The integration over dP_π is done with the Monte Carlo using the so-called "*point spectrometer*" mode, which works as follows. Once the desired model has been reached, the Monte Carlo is run with all physics calculations turned off (i.e., radiation, multiple scattering, etc.). It only generates events, at a desired kinematics, with the new iterated (corrected) model. The most important feature is that it takes into account Fermi motion when generating events for nuclear targets. After

Item	**Random** (%)	**Scale** (%)
Corrections		
Tracking efficiency	1.0	-
Trigger efficiency	0.1	-
Electric deadtime	0.1	-
Computer deadtime	0.3	-
Coincidence blocking	0.2	-
^{3}He Pressure correction	0.4	-
π Absorption	-	5.8
β=0 correction	0.5	-
SIMC(Monte Carlo)		
π Decay	0.5	-
Radiative Corrections	1.0	1.0
Acceptance Corrections	-	2.0
Iteration Correction	0.8	-
Model Dependence	0.5	-
Fitting error(LT)	0.3	-
N-N FSI	-	1.0
Target		
Charge	-	1.0
Target thicknesses		
19K Hydrogen	0.68	-
18K Hydrogen	0.89	-
LH_2	0.83	-
(^{3}He)	1.24	-
Kinematics		
Beam energy	0.25-0.5	-
Electron angle	0.4-1.3	-
Electron energy	0.1-0.5	-
Pion angle	0.1-0.2	-
Pion momentum	-	0.1-0.5
Total in Quadrature Sum	**2.4-3.1**	**6.3-6.4**

Table 5.1: Table of systematic errors from E91003 analysis. These errors can be broken down into scale and random errors. Random errors are exclusive to a particular kinematic setting, while scale error are global quantities that affect all settings.

Target	**W** (GeV)	ϵ	**polarity** π^+ or π^-	$\sigma_\mathbf{T} + \epsilon\sigma_\mathbf{L}$ (μb/sr)
H	1.15	0.86	π^+	22.35±0.76
H	1.15	0.43	π^+	14.69±0.46
H	1.6	0.89	π^+	60.96±1.95
H	1.6	0.49	π^+	46.86±0.99
^2H	1.15	0.86	π^+	11.68±0.36
^2H	1.15	0.43	π^+	8.07±0.26
^2H	1.15	0.86	π^-	12.06±0.42
^2H	1.15	0.43	π^-	6.61±0.18
^2H	1.6	0.89	π^+	45.52±1.39
^2H	1.6	0.49	π^+	34.59±0.98
^2H	1.6	0.89	π^-	49.32±1.27
^2H	1.6	0.49	π^-	32.11±0.85
^3He	1.15	0.86	π^+	16.93±0.61
^3He	1.15	0.43	π^+	12.34±0.49
^3He	1.15	0.86	π^-	6.56±0.26
^3He	1.15	0.43	π^-	4.14±0.19
^3He	1.6	0.89	π^+	77.91±2.36
^3He	1.6	0.49	π^+	59.96±1.74
^3He	1.6	0.89	π^-	30.01±0.97
^3He	1.6	0.49	π^-	21.41±0.56

Table 5.2: Results for the unseparated cross sections from the X(e,e'π)Y. The cross sections are in the lab frame and $\sigma_T + \epsilon\sigma_L$ was acquired by dividing out the photon flux factor after integrating over the pion momentum acceptance. These cross sections do not include the scale error. All data were taken at $Q^2 = 0.4$ $(GeV/c)^2$.

the Monte Carlo is finished, one integrates over the pion momentum acceptance to get the five-fold cross section. The Monte Carlo is first being used to generate the model cross sections, but this makes the P_π integration simple. The results of our unseparated lab cross sections for all W and ϵ settings of E91003 are listed in table 5.2.

5.4 L-T Separation

Now that the laboratory five-fold cross section has been extracted the next step is to separate the longitudinal and transverse components of the cross section via a *Rosenbluth Separation* (which is possible because we have full ϕ coverage for all ϵ points), and results in cancellation of the interference terms σ_{LT} and σ_{TT} as illustrated in equation 5.32:

$$\frac{d\sigma}{d\Omega_\pi} = \frac{d\sigma_T}{d\Omega_\pi} + \varepsilon_L \frac{d\sigma_L}{d\Omega_\pi} \tag{5.20}$$

With the interference terms gone, one is left with the longitudinal and transverse terms and may proceed with the separation by doing a *least square fitting* as explained in Appendix A. For this analysis, there were only two ϵ points so the longitudinal and transverse cross sections can be written as

$$\frac{d\sigma_L}{d\Omega_\pi} = \frac{\sigma_1 - \sigma_2}{\epsilon_1 - \epsilon_2}, \tag{5.21}$$

$$\frac{d\sigma_T}{d\Omega_\pi} = \frac{\epsilon_1\sigma_2 - \epsilon_2\sigma_1}{\epsilon_1 - \epsilon_2}. \tag{5.22}$$

Target	W (GeV)	σ_L (μb/sr)	σ_T (μb/sr)	R = $\frac{\sigma_L}{\sigma_T}$
H_{π^+}	1.15	17.81±2.07	7.03±1.19	2.53±0.38
$^2H_{\pi^+}$	”	8.40±0.79	4.28±0.48	2.06±0.37
$^2H_{\pi^-}$	”	12.67±1.06	1.16±0.55	10.92±4.61
$^3He_{\pi^+}$	”	10.67±1.82	7.75±1.15	1.38±0.27
$^3He_{\pi^-}$	”	5.63±0.75	1.72±0.46	3.27±1.33
H_{π^+}	1.6	35.25±5.46	29.58±3.24	1.19±0.18
$^2H_{\pi^+}$	”	27.33±4.25	21.20±2.76	1.29±0.20
$^2H_{\pi^-}$	”	43.02±3.83	11.03±2.45	3.90±0.78
$^3He_{\pi^+}$	”	44.88±7.34	37.97±4.84	1.18±0.18
$^3He_{\pi^-}$	”	21.50±2.79	10.88±1.72	1.98 ±0.24

Table 5.3: Results for the separated cross sections from the X(e,e‘π)Y reaction. The cross sections are in the lab frame and both statistical and systematic errors are shown. Cross sections are $\int \sigma_L dP_\pi$ for $0.248 < P_\pi < 0.350$ at W = 1.15 GeV and $P_\pi > 0.936$ for W=1.6 GeV.

5.5 Cross Section Ratios

The separated cross section ratios are listed in table 5.4 and illustrated in figure 5.13. The errors include both statistical and systematic added in quadrature. The helium-3 π^+ data was divided by 2 to account for the fact that there are two protons inside the nucleus. The photon flux factor (eqn.5.29) contains the equivalent photon energy, K_{eq}, which equals (W^2 - M^2)/2M where M is the mass of the nucleus, and should be the mass for a single nucleon for all targets. Correcting for this mass dependent term and applying them to the cross section ratios in table 5.4 gives one the “reduced” cross section ratios or the cross section ratio “per nucleon”. These are listed in table 5.5 and illustrated in figure 5.14.

Target Ratio	W(GeV)	Γ correction
${}^2H_{\pi^+}/H_{\pi^+}$	1.15	1.45
${}^3He_{\pi^+}/H_{\pi^+}$	"	1.61
${}^2H_{\pi^-}/{}^2H_{\pi^+}$	"	1.00
${}^3He_{\pi^-}/{}^2H_{\pi^-}$	"	1.10
${}^2H_{\pi^+}/H_{\pi^+}$	1.6	1.12
${}^3He_{\pi^+}/H_{\pi^+}$	"	1.16
${}^2H_{\pi^-}/{}^2H_{\pi^+}$	"	1.00
${}^3He_{\pi^-}/{}^2H_{\pi^-}$	"	1.03

Table 5.4: Corrections for the equivalent photon energy(K_{eq}) for each ratio. These corrections are multiplied by the raw ratios to calculate the "reduced" cross section ratios.

5.6 Quasifree Comparison

Comparing the (unmodified) cross section of a nuclear target with a proton target will not give a ratio of 1. What is being compared is the cross section for a moving target to that of a free proton. As stated earlier, the initial model is for a free proton, we add Fermi motion when we apply the point spectrometer. With the quasifree comparison we remove the Fermi motion to compare two free nucleons. When comparing data ratios to Monte Carlo ratios, there's the question of describing the Fermi motion of the nucleons at W = 1.15 GeV. Here, it is possible that a moving nucleon could fall below two pion threshold which would affect the outcome of the cross section. Two pion threshold is at 1.07 GeV and cuts were placed at 1.0 GeV so it wouldn't contribute to the cross section.

Starting with a model without nuclear pions (uniterated model) and using the point spectrometer, the ratio of the longitudinal cross sections were calculated as:

$$R^{model}_{A/H} = \frac{\int \sigma^A_L dP_\pi}{\sigma^H_L} \tag{5.23}$$

where no physics effects (radiative corrections, decay, etc.) were applied. Only P_π cuts were applied to compare directly with the data calculation. The model calculated ratios were determined with the same constraints as the data. The corrected super ratio is defined as:

$$R^{corr}_L = \frac{R^{data}_L}{R^{model}_L} \tag{5.24}$$

Table 5.7 lists the calculated longitudinal quasifree ratios. The corrected ratios are compared with points from a previous analysis of the data in figure 5.15 [**?**]. At low k_π one observes a suppression in the helium-to-hydrogen ratio and the deuterium-to-hydrogen ratio. At high k_π, however, it's difficult to conclude there's an enhancement.

5.7 Conclusions

The aim of **E91003** was to extract the longitudinal cross section and compare the ratios of the nuclear targets to that of a single proton to search for any target-dependent mass effects (ie pion excess). After necessary corrections were applied to the raw data, two models (multipole and maid) were modified iteratively until they were in agreement with the data. The iteration procedure included the

Target Ratio	W(GeV)	σ_L	σ_T
$^2H_{\pi^+}/H_{\pi^+}$	1.15	0.49±0.07	0.61±0.01
$^3He_{\pi^+}/H_{\pi^+}$	”	0.30±0.06	0.55±0.12
$^2H_{\pi^-}/^2H_{\pi^+}$	”	1.43±0.18	0.27±0.13
$^3He_{\pi^-}/^2H_{\pi^-}$	”	0.44±0.07	1.48±0.80
$^2H_{\pi^+}/H_{\pi^+}$	1.6	0.78±0.17	0.72±0.12
$^3He_{\pi^+}/H_{\pi^+}$	”	0.64±0.14	0.64±0.11
$^2H_{\pi^-}/^2H_{\pi^+}$	”	1.57±0.28	0.52±0.13
$^3He_{\pi^-}/^2H_{\pi^-}$	”	0.49±0.08	0.99±0.27

Table 5.5: Results for the separated cross section ratios from the X(e,e‘π)Y reaction. The cross sections are in the lab frame and include both statistical and systematic errors.

Target Ratio	W(GeV)	σ_L
$^2H_{\pi^+}/H_{\pi^+}$	1.15	0.71±0.19
$^3He_{\pi^+}/H_{\pi^+}$	”	0.48±0.14
$^2H_{\pi^-}/^2H_{\pi^+}$	”	1.43±0.18
$^3He_{\pi^-}/^2H_{\pi^-}$	”	0.48±0.13
$^2H_{\pi^+}/H_{\pi^+}$	1.6	0.87±0.17
$^3He_{\pi^+}/H_{\pi^+}$	”	0.74±0.14
$^2H_{\pi^-}/^2H_{\pi^+}$	”	1.57±0.28
$^3He_{\pi^-}/^2H_{\pi^-}$	”	0.50±0.08

Table 5.6: Results for the longitudinal cross section ratios from the X(e,e‘π)Y reaction. The cross sections are in the lab frame and include both statistical and systematic errors.

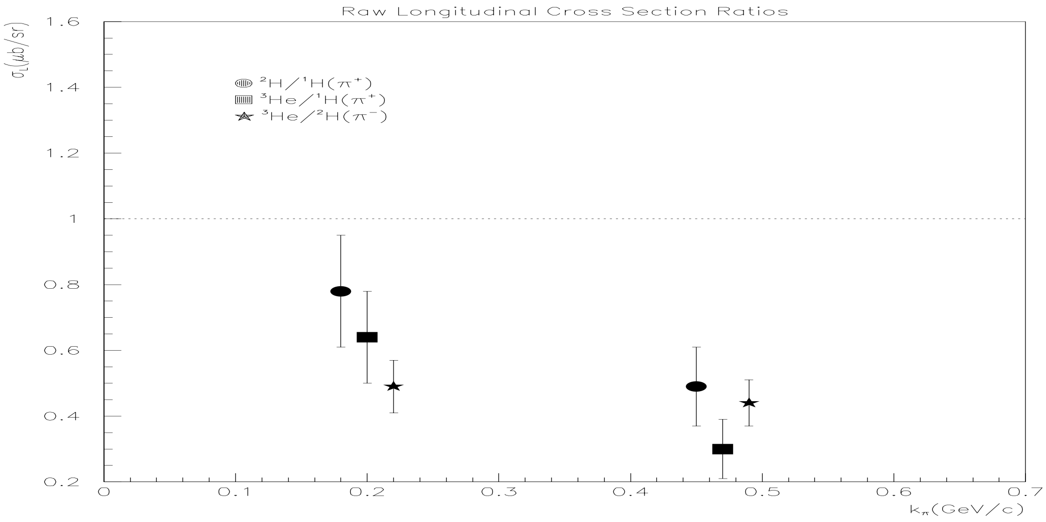

Figure 5.13: Raw Longitudinal cross section ratios for the reaction X(e,e‘π)Y.

application of two dimensional cuts to different permutations of Lorentz invariants Q^2, W, and t for hydrogen, and one dimensional cuts from ϕ and $\vec{p}_\pi$ for the nuclear targets. Once the iterations were completed, the cross section was integrated over the pion momentum acceptance to account for the extra degree of freedom due to Fermi motion. Cross sections were obtained by utilizing our Monte Carlo program in “point spectrometer” mode in a small kinematic bin. For hydrogen, this simply resulted in a delta function. But, for the nuclear targets, it helped to account simply for the part of the cross section due to the nucleons moving inside the nucleus. By plotting the cross section as a function of epsilon, for fixed W and Q^2, we were able to separate the longitudinal and transverse components of the cross section via a Rosenbluth separation. These results could then be compared

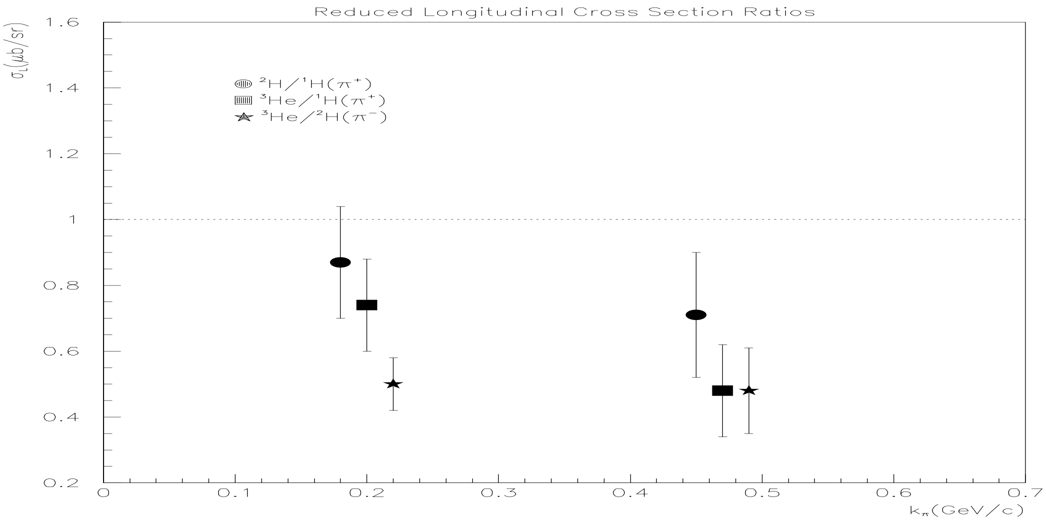

Figure 5.14: Reduced Longitudinal cross section ratios for the reaction X(e,e‘π)Y. Correction for mass in photon flux factor has been added.

to theory.

Friman et al. [5] calculated a expected suppression at low $k_\pi \approx 0.2$ (GeV/c) and enhancement at high $k_\pi \approx 0.47$ (GeV/c). This corresponds to our experimental W values of 1.6 and 1.15 GeV, respectively. See figure 5.15. At low k_π, in the data, there seems to be an apparent suppression consistent with the theoretical prediction. However, at high k_π there's no evidence of an enhancement. We believe the latter maybe due in part to the two pion threshold being so close to the low W value. For a nuclear target it is not inconceivable that some pions are kinematically below two pion threshold where they cannot be measured [58].

To test the pole dominance of the longitudinal cross section, the ratio of π^- to π^+ (table 5.6) is calculated. If the pole term is indeed dominant, one would

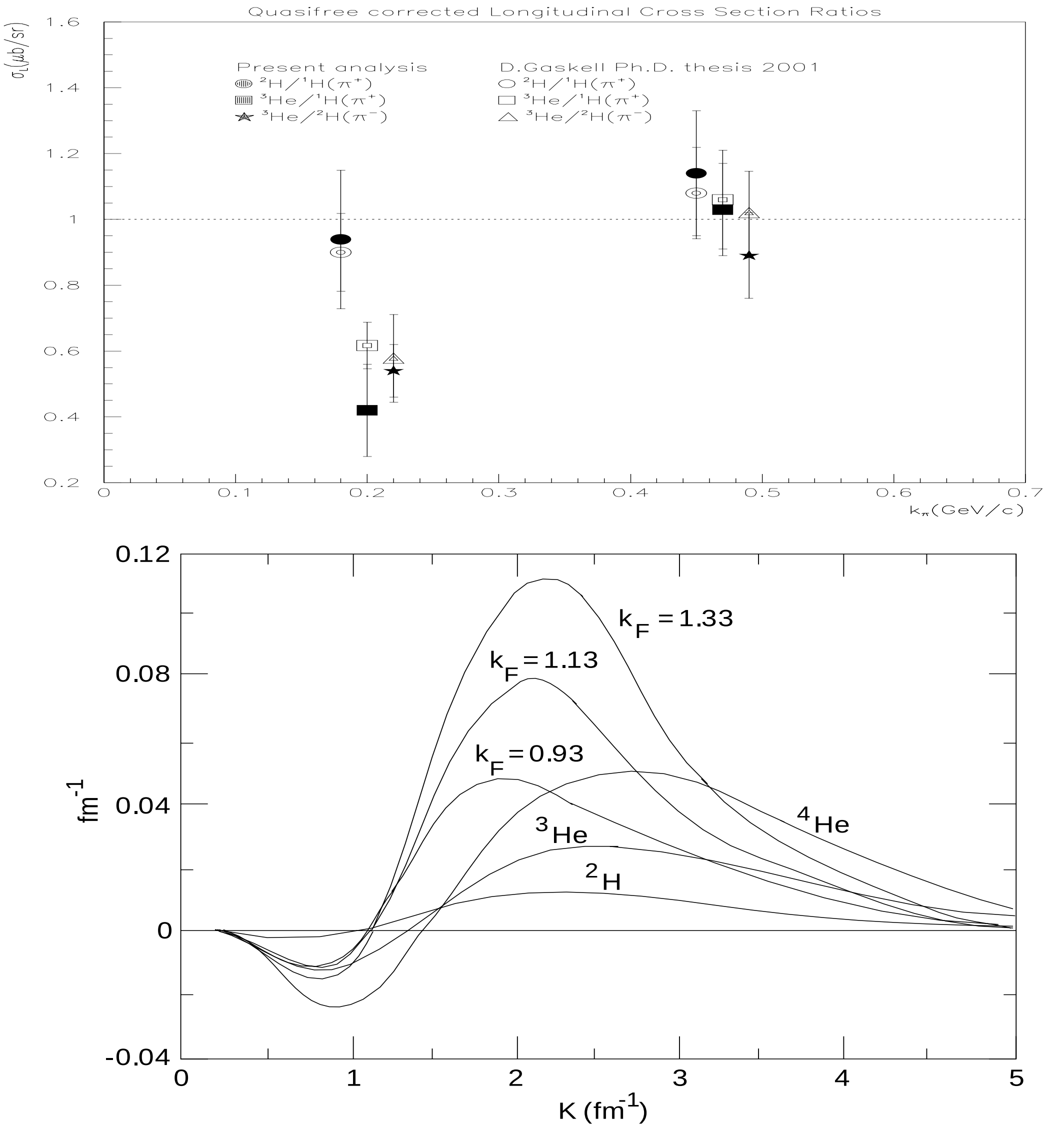

Figure 5.15: (Top) Corrected Longitudinal cross section ratios for the reaction X(e,e‘π)Y; (Bottom) Friman et al. calculation showing where a suppression and an enhancement are expected. Measurements for E91003 concentrated at K(fm^{-1}) of 1.01 and 2.3 which corresponds to a k_π of 0.2 and 0.47, respectively.

Target Ratio	W(GeV)	Longitudinal Cross Section Ratio
$^2H_{\pi^+}/H_{\pi^+}$	1.15	0.59±0.032
$^3He_{\pi^+}/H_{\pi^+}$	"	0.54±0.034
$^3He_{\pi^-}/^2H_{\pi^-}$	"	0.59±0.037
$^2H_{\pi^+}/H_{\pi^+}$	1.6	0.92±0.019
$^3He_{\pi^+}/H_{\pi^+}$	"	1.54±0.012
$^3He_{\pi^-}/^2H_{\pi^-}$	"	0.86±0.025

Table 5.7: Final longitudinal cross section ratios, including quasifree correction, as discussed. Cross sections are $\int \sigma_L dP_\pi$ for $0.248 < P_\pi < 0.350$ at W = 1.15 GeV and $P_\pi > 0.936$ for W=1.6 GeV.

expect this ratio to be one. The $\frac{\pi^+}{\pi^-}$ ratio $\neq 1$, signifying that there are non-pole contributions to the measured cross section. When probing the pion field, other reactions occurred which diluted the pion field.

In conclusion, we think it's fair to say that there's evidence of a small suppression at low k_π and no evidence for a large enhancement at high k_π. This analysis doesn't give conclusive evidence for or against nuclear pions, but it does give motivation in continuing the search for them. The search for nuclear pions is a phenomenological question that needs to be addressed.

At least three recommendations could be given for improving this experiment and having a better understanding of the results: (1) extend the experiment to include helium-4, where the a larger enhancement is calculated to be found. Larger effects are predicted for even heavier nuclei, but final state interactions can become more of a problem; (2) choose kinematics outside the resonance region, somewhere in the deep inelastic scattering (DIS) region, where the cross section is smoother and; (3) find theorists interested in calculating a relationship between σ_L and pion excess. Presently, there isn't a large effort to calculate this relationship.

Instead of measuring the pion, one could measure the recoil nucleus [59]. This would give a different perspective to the measurement, and perhaps contribute useful information. This experiment could be attempted with the use of a low-pressure multiwire proportional chamber (MWPC). This approach to the experiment would be difficult, a study would need to be done to find out it's feasibility. The construction of this detector is discussed in [60].

There has been some explanation to support the theory of nuclear pions, even given the disturbingly negative results. The idea of Brown-Rho scaling [57] has been introduced. This argument is based on the idea that, at a finite density hadrons increase in size or "swell" making it harder for a pion to get out.

Until either nuclear pions are directly and unambiguously observed, or a testable theory to explain why they are not is tested, the question "Where are the nuclear pions?" will remain a key issue in nuclear physics. It is a question of fundamental importance in our understanding of the nuclear force and the structure of nuclei.

Appendix A

Least Square Fitting

The method of least squares assumes that the best-fit function of a given type is the one that has the minimal sum of the deviations squared (least square error) from a given set of data. Suppose that the data points are (x_1, y_1), (x_2, y_2) , ..., (x_n, y_n) where x is the independent variable and y is the dependent variable. The function $f(x)$ of the line fitting the data points has a deviation d from each data point, with $d_1 = y_1 - f(x_1)$, $d_2 = y_2 - f(x_2)$, ..., $d_n = y_n - f(x_n)$. According to the method of least squares, the best fitting curve has the property that:

$$minimum = d_1^2 + d_2^2 + ... + d_n^2 = \sum_{i=1}^{n} d_i^2 = \sum_{i=1}^{n} [y_i - f(x_i)]^2 \tag{A.1}$$

Our fitted function has the linear general form

$$\sigma = \sigma_T + \epsilon \sigma_L \rightarrow f(x) = b + xa \tag{A.2}$$

where $a = \sigma_L$ and $b = \sigma_T$ are our unknown parameters. Plotting the cross section as a function of ϵ gives σ_L as the slope of the line and σ_T as the y-intercept. This is illustrated in figure A.1.

To find a method to measure the probability that a function really represents the data, however, takes an additional step. The general form of a mathematical function will have a number of free parameters, that can be adjusted to change the shape of the function. For example, if a program tries to fit a line from a set of data points using the slope-intercept formula, it will adjusts the slope (m) and

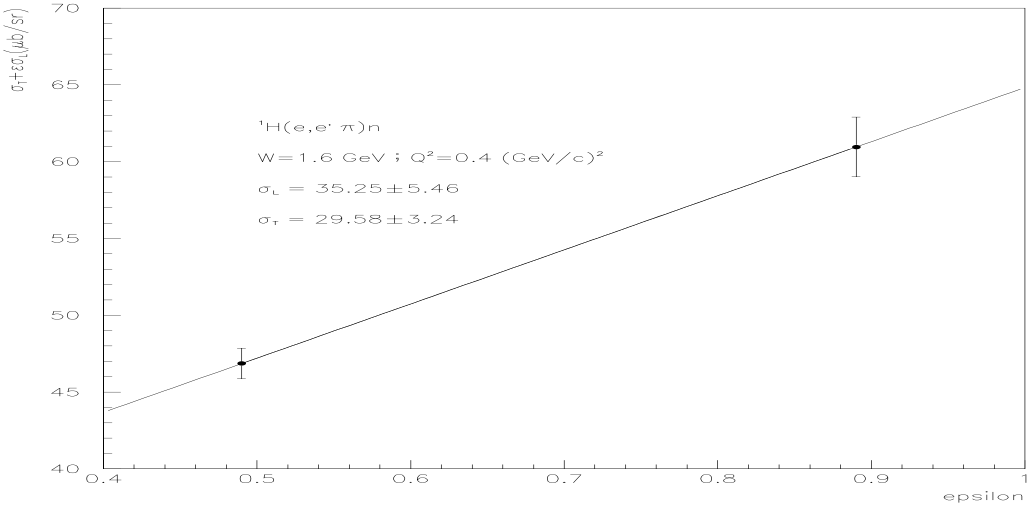

Figure A.1: Example of the extraction of L/T separated cross sections for the reaction $^1H(e,e'\pi^+)n$ at $W = 1.6$ GeV and $Q^2 = 0.4$ $(GeV/c)^2$.

the intercept (b) until χ^2 has reached a minimum value. If there are only two data points, this minimum value will always be zero, because two points define a line. The same thing happens if we try to fit three points to a quadratic curve, four points to a cubic, etc. Because of this, the first few data points don't give us any real information about the "goodness of fit". To address this issue the concept of $degrees\ of\ freedom$ is introduced. We say that any attempt to fit a function to a dataset has d = N - f degrees of freedom, where N is the number of data points and f is the number of free parameters in the function. To work out the probability that our function represents the data set, we use the "reduced" χ^2, which is just χ^2 divided by the number of degrees of freedom. This is a way of partitioning the deviancy of our function evenly between the significant data points. Since the expected value of any single deviation is σ, it's fair to say that the expected value of the reduced χ^2 is 1, if the fit really does represent the data. If it comes out to much less than one, you probably overestimated your uncertainties, and if it comes out to more than one, the probability that the fit is reasonable drops accordingly. For further discussion refer to reference [52].

Once one has the reduced χ^2, one can calculate the "confidence level" given by:

$$P_x(\chi^2, d) = \frac{1}{2^{(\frac{d}{2})}\Gamma(\frac{d}{2})} \int_{\chi^2}^{\infty} x^{(d-2)/2} e^{-x/2} dx. \tag{A.3}$$

The confidence level tells how sure a χ^2 fit can be. In other words, the confidence level is the probability value (1-α) associated with a confidence interval, and α is sometimes called the risk level and is a tabulated variable [54].

Appendix B

Relevant variable definitions

Hall C variables	Definition
HMS Quantities	
hsdelta	$\equiv \delta = \frac{\mathbf{p}-p_{HMS}}{p_{HMS}}$. The percentage a particle deviates from the central momentum setting in the HMS.
hsxptar	= $\tan\phi_{particle}$. Slope of the projection of the trajectory in the x-z plane at the target in the HMS.
hsyptar	= $\tan\theta_{particle}$. Slope of the projection of the trajectory in the y-z plane at the target in the HMS.
hsytar	The position of the interaction point along the length of the target cell.
hsxfp	HMS position at the focal plane in the dispersive direction (downward)
hsxpfp	= $\tan\phi_{particle}$. Slope of the projection of the trajectory in the x-z plane at the plane focal in the HMS.
SOS Quantities	
ssdelta	$\equiv \delta = \frac{\mathbf{p}-p_{SOS}}{p_{SOS}}$. The percentage a particle deviates from the central momentum setting in the SOS.
ssxptar	= $tan\phi_{particle}$. Slope of the projection of the trajectory in the x-z plane at the target in the SOS.
ssyptar	= $tan\theta_{particle}$. Slope of the projection of the trajectory in the y-z plane at the target in the SOS.
ssytar	The position of the interaction point along the length of the target cell.
ssxfp	SOS position at the focal plane in the dispersive direction (downward)
ssxpfp	= $\tan\phi_{particle}$. Slope of the projection of the trajectory in the x-z plane at the focal plane in the SOS.
Physics Quantities	
missing mass	momentum of undetected particle.
Q^2	Virtual photon four-momentum transfer squared.
W	Invariant mass of the virtual photon-target system.
$minust$	Square of the four-momentum transferred to the nucleon.
$theta_{pq}$	θ angle between the pion and virtual photon.
phi_{pq}	Azimuthal angle between the scattering and reaction planes.
$epsilon$	Virtual photon transverse linear polarization.
k_π	Momentum of the pion.

Table B.1: Definitions of Hall C variables used throughout this thesis.

BIBLIOGRAPHY

[1] E.D. Bloom et al., *Phys. Rev. Lett.*, **23** 930, 1969.

[2] J.I. Friedman and H.W. Kendall, *Ann. Rev. Nucl. Part. Sci.*, **22** 203, 1972.

[3] F.J. Yndurain, *Quantum Chromodynamics; an introduction to the theory of quarks and gluons.*, Springer, Heidelberg; 1983.

[4] G. Bertsch, L. Frankfurt, and M. Strikman, Science, **259** 773, 1993.

[5] B.L. Friman, V.R. Pandharipande, R.B. Wiringa, *Phys. Rev. Lett.* **51** 763, 1983.

[6] J.J. Aubert *et al.*, *Phys. Lett.* **123B** 275, 1983.

[7] M. Erickson, A.W. Thomas, *Phys. Lett.* **128B** 112, 1983.

[8] A. Bodek *et al.*, *Phys. Rev. Lett.* **50** 1431, 1983.

[9] R.G. Arnold *et al.*, *Phys. Rev. Lett.* **52** 727, 1984.

[10] J. Ashman *et al.*, *Z. Phys.*. **C57** 211, 1993.

[11] J. Ashman *et al.*, *Phys. Lett.* **202B** 603, 1988.

[12] T.A. Carey *et al.*, *Phys. Rev. Lett.* **53** 144, 1984.

[13] L.B. Rees *et al.*, *Phys. Rev.* **C34** 627, 1986.

[14] J.B. McClelland *et al.*, *Phys. Rev. Lett.* **69** 582, 1992.

[15] X.Y. Chen *et al.*, *Phys. Rev.* **C47** 2159, 1993.

[16] M. Moss, *Phys. Rev.* **C26** 727, 1982.

[17] E. Bleszynski *et al.*, *Phys. Rev.* **C26** 2063, 1982.

[18] J.B. McClelland *et al.*, *Phys. Rev. Lett.* **52** 98, 1984.

[19] D.M. Alde *et al.*, *Phys. Rev. Lett.* **64** 2479, 1990.

[20] P.B. Cushman. *Instrumentation in High Energy Physics.* World Scientific, 1993.

[21] C.A. Heusch. *Nucl. Inst. Meth..* **A248** 157, 1986.

[22] H. Mkrtchyan (unpublished).

[23] G. Heyes et al., *Proceedings of the TOOLS 8 Conference,* pages 171-183, July 1992.

[24] G. Heyes et al., *Proceedings of the CHEP COnference,* pages 122-126, April 1994.

[25] D. Abbott et al., *Proceedings of the IEEE COnference on Real Time Computer Applications in Nuclear, Particle, and Plasma Physics,* page 147, Michigan State University - NSCL, 1995.

[26] N.C.R. Makins, Ph.D thesis, Massachusetts Institute of Technology, 1994.

[27] T.G. O'Neill, Ph.D thesis, California Institute of Technology, 1994.

[28] D.M. Koltenuk, Ph.D thesis, University of Pennsylvania, 1999.

[29] J. Cha, Ph.D thesis, Hampton University, 2000.

[30] J. Volmer, Ph.D thesis, Vrije Universiteit, 2000.

[31] D.J. Gaskell, Ph.D thesis, Oregon State University, 2001.

[32] W. Hinton, Ph.D thesis, Hampton University, 2001.

[33] M. Berz, *Technical Report USUCL-977.* Michigan State University(unpublished), 1995.

[34] C. Caso *et. al.,* Euro. Phys. J. **C3**, 1 (1998).

[35] J. Schwinger, Phys. Rev. **76**, 790 (1949).

[36] L.W. Mo and Y.S. Tsai, Rev. Mod. Phys., **41**, 205 (1969).

[37] Y.S. Tsai, Phys. Rev. **122**, 122 (1961).

[38] D. Drechsel, O. Hanstein, S.S Kamalov and L. Tiator, *"A Unitary isobar model for pion photoproduction and electroproduction on the proton up to 1-GeV",* Nucl. Phys. **A645**, 145 (1999).

[39] Chew, *et. al.,* Phys. Rev. **106**, 1345 (1957).

[40] Walker, *et. al.,* Phys. Rev. **182**, 1729 (1969).

[41] Bartl, *et. al.,* Nuc. Phys. **B62**, 267 (1973).

[42] *Introduction to Q.* LAMPF technical Report (unpublished)(1994).

[43] D.F. Geesaman, S. Wood *Hall C Analysis Software Vade Mecum,* Jlab Hall C Internal Report (unpublished)(1994).

[44] D. Abbott et al., *The CODA System and its Performance.* Proceedings of the 1995 IEEE Conference on Real-Time Computing Applications in Nuclear, Particle, and Plasma Physics, pp. 147-151 (1995).

[45] K. Brown, *A First and Second order Matrix Theory for the Design of Beam Transport Systems and Charged Particle Spectrometers,* SLAC Report-75(1982).

[46] K.Makino and M.Berz, Nucl. Instr. Meth. **A427**, 338 (1999).

[47] C.S. Armstrong, *Hall C Time-of-Flight Fitting Code,* Jlab Hall C Internal Report (unpublished)(1995).

[48] G. Niculescu, *Shower Counter and Čherenkov Efficiencies,* Jlab Hall C Internal Report (unpublished)(1997).

[49] D.J. Mack, Private Communication(1997).

[50] R. Mohring, Ph.D thesis, University of Maryland, 2000.

[51] R.M. Gibbons and D.I. Nathan, *Thermodynamic Data of Helium-3,* AFML-TR-67-175, 1967.

[52] W.J. Metzger, *Statistical Methods in Data Analysis,* Experimental High Energy Physics Group, NIHKEF(1996).

[53] CERN Program Library Long Writeup Q121, CERN Software Group, *PAW - Physics Analysis Workstation* Reference Guide, (1995).

[54] L. Lyons, *Statistics for Nuclear and Particle Physicists,* Cambridge University Press, (1986).

[55] R.M. Barnett et al, *Physical Review,* **D54**, 72(1996).

[56] T.G. O'Neill, *Phys. Lett.,* **351**, 87 (1995).

[57] G.E. Brown et al, *Nucl.Phys.* **A593**, 295-314(1995).

[58] D.S. Koltun, *Physical Review,* **C57**, 1210(1998).

[59] D.M. Skopik et al., *Physical Review,* **C18**, 2219(1978).

[60] K. Assamagan et al., *Nucl.Inst. and Methods,* (accepted for publication)

[redacted]

Stephen Milton Avery [redacted] He graduated from Central High School (245) in Philadelphia and went to Millersville University to study physics. In May 1994 he received his B.S. degree in physics with a minor in Mathematics. In September of 1994, he began his graduated studies in Nuclear Physics at Hampton University. In May 1997 he received his M.S. in Nuclear Physics and in May 2002 he received his Ph.d in Nuclear Physics from Hampton University. On October 13, 1990 he married LaShon Bey. They have one daughter, Taylor Autumn, who was born on May 6, 1998. They presently reside in Newport News, Virginia.